Doctoral Dissertation

Hybrid quantum system based on a nitrogen vacancy center with phonon and magnon coupling

Dongkwon Lee

Department of Physics

Graduate School

Korea University

February 2026

Hybrid quantum system based on a nitrogen vacancy center with phonon and magnon coupling

by
Dongkwon Lee

---

under the supervision of Professor Donghun Lee

A dissertation submitted in partial fulfillment of
the requirements for the degree of
Doctor of Philosophy

Department of Physics

Graduate School
Korea University

October 2025

The dissertation of Dongkwon Lee has been approved by
the dissertation committee in partial fulfillment of the
requirements for the degree of
Doctor of Philosophy

December 2025

Committee Chair: Sang-Hoon Lee

Committee Member: Donghun Lee

Committee Member: Eun-mi Chae

Committee Member: Seok-Kyun Son

Committee Member: Nojoon Myoung

Hybrid quantum system based on a nitrogen vacancy center with phonon and magnon coupling

by Dongkwon Lee

Department of Physics

under the supervision of Professor Donghun Lee

Abstract

The advancement of quantum information theory has underscored the need to realize networks based on entanglement among many qubits. In solid state spin qubit systems, the appropriate coupling mechanism depends strongly on the separation between qubits. Interactions with nuclear spins can mediate coupling over extremely short distances on the order of a few nanometers, whereas photonic links enable connections over kilometer scale distances. However, connecting spin qubits at the on-chip scale calls for different information carriers.

Bridging the intermediate, on-chip regime motivates hybrid quantum systems, since no single qubit platform simultaneously provides long lived memory, fast control, and scalable interconnects. In this context, phonons and magnons are promising on-chip mediators that can interface spin qubits with other quantum systems and enable hybrid quantum architectures. This dissertation investigates phonon- and magnon-mediated interactions with NV centers in diamond as a route toward hybrid quantum platforms.

Using engineered mechanical resonators, surface acoustic waves, and patterned magnetic structures, we experimentally study strain mediated coupling between phonons and NV centers, spin wave driven control and imaging of NV spins, and phonon–magnon

coupling. We demonstrate tunable strain coupling achieved through interference between two mechanical modes, providing additional control over the strain field experienced by NV centers. We further show that spin waves can coherently manipulate NV center spin states and enable spatial imaging of wavefronts. In addition, we demonstrate acoustic generation of spin waves using surface acoustic waves and observe NV spin transitions induced by the resulting magnons, establishing a phonon-magnon-spin coupling pathway.

All experiments presented in this dissertation are performed in the classically driven regime, where the relevant strain and spin wave fields contain a large number of quanta. While this regime does not yet realize coherent coupling at the single quantum level, it elucidates the key physical mechanisms and coupling channels required for hybrid quantum interfaces. The results of this work establish an experimental foundation for NV center-based hybrid platforms in which phonons and magnons act as information carriers.

Keywords: NV center, magnon, phonon, strain, SAW

포논과 매그논 커플링을 이용한 질소 공공 중심 기반의 하이브리드 양자 시스템 구성

이 동 권

물 리 학 과

지 도 교 수: 이 동 헌

국문 초록

양자 정보 이론의 발전은 다수의 큐비트 사이에 얽힘을 기반으로 한 네트워크를 구현할 필요성을 부각시켰다. 고체 상태 스핀 큐비트 시스템에서 적절한 결합 메커니즘은 큐비트 간 거리의 크기에 의존한다. 핵스핀과의 상호작용은 수 나노미터 수준의 극히 짧은 거리에서 결합을 매개할 수 있는 반면, 광자 기반 링크는 킬로미터 규모의 장거리 연결을 가능하게 한다. 그러나 칩 상(on-chip) 규모에서 스핀 큐비트를 연결하기 위해서는 이와는 다른 정보 전달 매개체가 요구된다.

이러한 중간적인 온칩 영역의 연결은 하이브리드 양자 시스템에서 필요로 한다. 단일한 큐비트 플랫폼이 긴 수명의 메모리, 빠른 제어, 그리고 확장 가능한 상호연결성을 동시에 제공하지 못하기 때문이다. 이러한 맥락에서 포논과 마그논은 스핀 큐비트를 다른 양자 시스템과 인터페이스하고 하이브리드 양자 아키텍처를 가능하게 하는 유망한 온칩 매개체로 주목받고 있다. 본 학위논문은 하이브리드 양자 플랫폼으로 나아가는 경로로서, 다이아몬드 내 질소 빈자리 결함중심(nitrogen vacancy center)와의 포논(phonon) 및 마그논(magnon) 매개 상호작용을 연구한다.

본 연구에서는 기계적 공진기, 표면 음향파(surface acoustic wave), 그리고 패터닝된 자성 구조를 활용하여 포논에 의한 스트레인 결합, 스핀파에 의한 NV 중심 스핀 제어 및 이미징, 그리고 포논-마그논 변환 현상을 실험적으로 조사하였다. 두 개의 기

계적 모드 간 간섭을 이용하여 NV 중심에 작용하는 스트레인 결합을 조절할 수 있음을 보였으며, 이를 통해 스트레인 기반 제어의 자유도를 확장하였다. 또한 마그논 스핀파를 이용해 NV 중심의 스핀 상태를 결맞게 제어하고, 스핀파의 파면을 공간적으로 이미징할 수 있음을 실험적으로 입증하였다. 더 나아가 표면 음향파를 이용해 스핀파를 생성하고, 그 결과로 발생한 마그논이 NV 중심의 스핀 전이를 유도함을 관측함으로써 포논–마그논–스핀으로 이어지는 결합 경로를 확립하였다.

본 논문에서 제시된 모든 실험은 다수의 양자수를 포함하는 고전적 영역에서 수행되었다. 비록 단일 양자 수준의 결맞은 결합에는 아직 도달하지 못하였으나, 본 연구는 포논과 마그논을 매개로 하는 하이브리드 양자 인터페이스에 필요한 핵심 물리 메커니즘과 결합 경로를 명확히 규명한다. 이러한 결과는 포논과 마그논을 파동 기반 전달자로 활용하는 NV 중심 기반 하이브리드 양자 플랫폼의 실험적 기반을 제공하며, 향후 단일 양자 영역으로 확장하기 위해 요구되는 조건을 제시한다.

중심어 : 질소 빈자리 중심, 매그논, 포논, 변형률, 표면 탄성파

Preface

The strain-based experiments were carried out by constructing and operating the experimental setup together with Sunuk Choe, Wookyoung Choi, and Chanhu Park. The strain related work was published in [“Tuning strain coupling between diamond oscillators and NV centers via interference of two mechanical modes,” Dongkwon Lee, Seonho Lee, Jaebum Park, Sungjin Jang, Chanhu Park, Sunuk Choe, Preeti Ovartchaiyapong, Ania C. Bleszynski Jayich, and Donghun Lee, APL Quantum 2, 046107 (2025)]. I contributed to fabrication, measurements, and manuscript preparation.

The spin wave imaging experiments were performed using a scanning setup, with the technical support of Yuhan Lee, Seokmin Lee, Seongjin Jang, and Chanjong Ham. Some of the spin wave results were obtained using a wire patterned YIG film provided by the KAIST Ultrafast Spin Dynamics Lab (led by Kab-Jin Kim). The work on the spin wave reflector described in Chapter 6 was published in [“Characterization of magnetic Bragg reflectors on YIG thin film to control spin wave transmission,” Dongkwon Lee, Moojune Song, Kihwan Kim, Albert Min Gyu Park, Mujin You, Youngseon Soon, Kab-Jin Kim, and Donghun Lee, Journal of the Korean Physical Society (2025) 86:1066 -1071]. I was responsible for fabrication, measurements, and manuscript preparation. The content of Chapter 7 was presented at [“Toward Hybrid Quantum Systems Based on Solid-State Spin Qubits,” 2023 IBS Conference on Quantum Nanoscience].

Acknowledgment

2018년부터 2025년까지 긴 시간 동안 학업을 이어오며 힘든 순간도, 즐거운 순간도 많았습니다. 그 과정 속에서 제가 무사히 졸업에 이르기까지 많은 분들의 도움과 배려를 받을 수 있었기에, 이 자리를 빌려 진심으로 감사의 말씀을 전하고자 합니다.

먼저, 학위논문 심사에 참여해 주신 이상훈 교수님, 채은미 교수님, 손석균 교수님, 명노준 교수님께 깊이 감사드립니다. 교수님들의 소중한 조언과 지적 덕분에 논문의 부족한 점들을 보완하고 보다 완성도 높은 연구로 마무리할 수 있었습니다.

저의 지도교수님이신 이동헌 교수님께 진심으로 감사드립니다. 교수님께서는 제가 다양한 관점에서 생각할 수 있도록 끊임없이 아이디어를 제시해 주셨고, 실험을 수행하는 데 있어 아낌없는 지원을 해주셨습니다. 또한 실험뿐만 아니라 학회 등 외부 활동에도 적극적으로 참여할 수 있도록 배려해 주셔서, 대학원 생활 동안 연구 외적으로도 많은 경험을 쌓을 수 있었습니다. 교수님의 지도와 지원이 없었다면 이 학위를 마칠 수 없었을 것입니다.

대학원 생활 동안 가장 많은 시간을 함께한 사람들은 같은 연구실 구성원들이었습니다. 연구실에 처음 들어왔을 때 순욱이 형이 기본적인 연구와 실험에 대해 많은 것을 가르쳐 주었고, 우경이 누나와 찬후와는 함께 실험을 진행하며 많은 도움을 받았습니다. 함께 실험하며 큰 힘이 되어 주어 감사한 마음이 크며, 한편으로는 제가 알게 모르게 스트레스를 주지는 않았을까 하는 미안한 마음도 남아 있습니다. 이후 함께 연구를 진행했던 유한이, 석민이, 찬종이, 성진이에게도 제가 미처 알지 못했던 부분들에

대해 많은 도움을 받았고, 덕분에 소중한 실험 데이터를 얻을 수 있었습니다.

기환이와는 직접 실험을 함께한 시간은 많지 않았지만, 가장 많은 시간을 함께 보내며 실험에 대한 다양한 상상과 아이디어를 나누고 막히는 부분을 함께 고민해 주어 제 졸업 과정에 큰 도움이 되었습니다. 주경이에게도 연구실 생활 동안 실험 외적으로도 함께 시간을 보내며 많은 도움을 받았고, 이수와는 705호 같은 방에서 지내며 실험 과정에서의 어려움들을 논의하며 제게 필요한 배움을 쌓을 수 있었습니다. 현준이와도 학회나 회식 자리에서 함께하며 덕분에 대학원 생활을 보다 즐겁게 보낼 수 있었습니다. 재범이와 선호에게는 제가 공정 작업을 가르치는 과정에서 함께 시행착오를 겪으며 오히려 저 또한 많은 것을 배울 수 있어 감사하게 생각합니다. 새로 연구실에 합류한 선우를 포함해 연구실 모든 구성원들이 즐겁고 의미 있는 연구실 생활을 이어가길 바라며, 졸업 후에도 좋은 인연으로 계속 만날 수 있기를 바랍니다.

연구실 구성원들 외에도 대학원 생활 동안 가장 자주 만났던 분들은 KIST Micro Nano Fab Center의 선생님들이었습니다. 아무것도 모른 채 시행착오를 반복하던 시절부터 팹을 이용하며 수많은 실패를 겪었지만, 그때마다 선생님들께서 마치 자신의 일처럼 함께 고민해 주시고 조언과 개선 방향을 제시해 주신 덕분에 불필요한 시행착오를 줄일 수 있었습니다. 매번 따뜻하게 맞아 주셨던 곽승민 선생님, 남기훈 선생님, 정승운 선생님께 깊이 감사드리며, 앞으로도 항상 좋은 일들만 가득하시길 바랍니다.

또한 대학원 생활 동안 스핀파 관련 측정에서 많은 도움을 주신 김갑진 교수님과 KAIST USDL 연구실 구성원들께도 감사의 말씀을 전합니다. 송무준 박사님, 유무진 박사님, 박민규 박사님, 그리고 영선 씨와 함께 측정을 진행하며 문제점을 논의하고 앞으로의 방향을 이야기했던 대전 출장 기간은 새로운 상상을 할 수 있었던 소중한 시간이었습니다. 마지막 한 학기 동안 USDL 연구실에 머무르며 연구실 구성원 모두가 따뜻하게 맞아 주신 덕분에 매우 즐거운 시간을 보낼 수 있었고, 저널 클럽을 통해 평소 접하지 못했던 다양한 논문들을 접할 수 있어 뜻깊었습니다. 함께 지낼 시간이 조금 더 길었다면 더욱 가까워질 수 있었을 텐데 하는 아쉬움은 남지만, 앞으로도 계속 이어질

인연이 되기를 바랍니다.

박승 박사님과 기경이형은 자주 만나고 놀며 실없는 얘기도 많이 하지만 서로의 분야에 대해 얘기를 하며 친숙하지 않던 분야에 대해 알 수 있었습니다. 대학원 과정이라는 비슷한 상황을 겪어내며 공감할 수 있는 고민들이 많았고 그로 인해 제가 고민이 있을 때 가장 먼저 도움을 청할 수 있었던 사람들입니다.

학교 밖에서 만난 다양한 사람들은 대학원 생활동안의 짐을 잊고 즐겁게 생활할 수 있게 도움을 주었습니다. 훈련소에서 만나 이제는 연례행사로 일년에 한 번씩은 만나고 있는 윤호, 태웅, 규희, 태림, 재욱, 진호 모두 자주 만나지는 못하지만 앞으로도 계속 만날 인연들이 되어주어서 감사합니다. 또한 준석이, 수찬이, 현종이, 동균이는 학부 때부터 학교에 같이 야구하며 알고 지냈고 후에 사회인 야구팀도 같이 하며 완진이형, 대진이형, 연수, 민홍, 진솔과 같이 안 굴러가는 야구팀을 열심히 굴려가며 고생도 많았습니다. 한 팀의 일원으로서 너무 감사합니다.

대학원생활이 길었던 만큼 많은 사람들을 만났습니다. 같은 물리학과의 사람들에게 학문적인 도움도 받고, 학교 밖 사람들과 개인적으로 교류하며 인간적인 도움도 받았습니다. 저에게 도움주었던 많은 분들께 저 또한 그 분들께 도움되는 사람이 되기 위해 노력하고자 합니다.

Table of Contents

List of Tables

List of Figures

Nomenclature

Abbreviation	
CPW	Coplanar Waveguide
CWESR	Continuous Wave Electron Spin Resonance
DBR	Distributed Bragg Reflector
ESLAC	Excited state level anti-crossing
FMR	Ferromagnetic Resonance
GSLAC	Ground state level anti-crossing
IDT	Interdigital Transducer
MSSW	Magnetostatic Surface Spin Wave
NV center	Nitrogen Vacancy center
PCB	Printed Circuit Board
PL	Photoluminescence

SAW	Surface Acoustic Wave
TR-MOKE	Time-Resolved Magneto-Optic Kerr Effect
VNA	Vector Network Analyzer
XMCD	X-ray Magnetic Circular Dichroism
YIG	Yttrium Iron Garnet

Chapter 1. Introduction

Advances in quantum mechanics have given rise to quantum information science, in which quantum states serve as the fundamental units of information. A qubit operates on the basis of superposition and entanglement, phenomena that cannot be explained within classical mechanics and require a fully quantum mechanical description. Many theoretical and experimental studies have investigated the potential advantages of quantum computing over classical computing.

Beyond the question of computational supremacy, however, Feynman's well known remark: "Nature isn't classical, dammit, and if you want to make a simulation of nature, you'd better make it quantum mechanical, and by golly it's a wonderful problem, because it doesn't look so easy." [2] highlights that quantum mechanical computation may be essential for faithfully simulating physical phenomena in nature.

Growing interest in quantum information and its theoretical progress has naturally raised the question of whether quantum computers can be realized in practice. Recently, qubits have been realized on various physical platforms, including trapped ions [3], neutral atoms [4], electron/nuclear spins [5], superconducting transmon qubits [6], color centers [7], and photons [8]. A practical qubit requires a well defined two level system, long coherence times under realistic noise, and the ability to perform fast, high fidelity operations. Moreover, to perform large scale computations, an efficient method for coupling

multiple qubits is required. Some researchers search for new qubit platforms that satisfy these requirements [9], while others focus on building large scale qubit processors by interconnecting many qubits. For example, a 54 qubit superconducting transmon processor that demonstrated quantum advantage was reported [10].

Among the various qubit platforms, the nitrogen vacancy (NV) center in diamond, a type of color center, has attracted significant attention because it can operate even at room temperature. This feature makes NV centers promising as quantum sensors for measuring specific physical quantities in practical settings. In particular, for magnetic field sensing, their high sensitivity has enabled the detection of new physical phenomena in fundamental science [11, 12], and their room temperature operability has facilitated applications as compact magnetic sensors in everyday environments [13–15].

Beyond the advantages of individual NV centers, coupling them to surrounding qubits can further strengthen their potential for quantum computing. For instance, nuclear spins near an NV center experience weaker environmental interactions than the NV electronic spin, and thus exhibit much longer coherence times [16]. Entanglement between the NV center and nearby nuclear spins provides benefits unattainable with an NV center alone, and such schemes have been experimentally demonstrated [17].

However, because the interaction range between an NV center and nuclear spins is short, scaling up through NV and nuclear spin coupling is fundamentally limited. As an alternative, entanglement mediated by the optical properties of NV centers has been developed. Entanglement between two remote NV centers by measuring photons entangled with each NV center is demonstrated [18].

To achieve scalable interconnections in NV centers-based qubit networks, a quantum information carrier for communicating with NV centers is required. Such carriers must be controllable, and their coupling to NV centers must be sufficiently strong. One promising

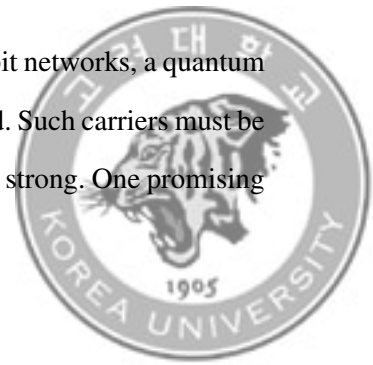

candidate is the phonon, the quantum of mechanical motion [19]. An experiment measured the coupling between NV centers and mechanical motion [20]. Another candidate is the magnon, the quantum of spin waves. Spin waves generate local magnetic fields, which can interact with NV centers. This coupling has enabled spin wave imaging using NV centers, and theoretical proposals have suggested magnon mediated entanglement between NV centers [21].

In this dissertation, the properties of the NV center as a qubit are investigated, and the interactions between NV centers and phonons, NV centers and magnons, as well as phonon-magnon coupling and their combined interaction with NV centers, are experimentally demonstrated. Based on these results, the feasibility of phonons and magnons as quantum information carriers for constructing NV center-based quantum networks is explored.

Chapter 2 examines the fundamental characteristics of NV centers as qubits through their electronic structure and optical properties, and presents experimental measurements that validate these characteristics. Chapter 3 describes the confocal microscope setup required for NV center measurements, along with the microwave electronics used for NV state control and for generating spin waves and surface acoustic waves (SAWs).

Chapter 4 focuses on NV-phonon interactions. A mechanical resonator is fabricated and actuated, and strain induced effects on NV centers are measured using a spin echo protocol. In addition, to test whether strain coupling can be tuned via interference between distinct strain coupling, a resonator supporting two vibrational modes is fabricated, and interference between the strain couplings of these modes is experimentally characterized.

Chapter 5 investigates NV-magnon interactions. The dispersion relation of spin waves is analyzed to identify wavelengths and frequencies capable of coherent coupling to NV

centers. Spin wave properties such as directionality and wavelength are then characterized using NV-based measurements. Chapter 6 studies the confinement of spin waves using a cavity structure. Simulations examine the possibility of spatial localization of spin waves, and selective transmission of spin waves through a stripe patterned structure is experimentally measured as a function of wavelength.

Chapter 7 explores phonon-magnon interactions probed with NV centers. The substrate and transducer used to generate SAWs are described, and the generated waves are confirmed via transmission measurements. A ferromagnetic film is deposited along the acoustic wave propagation path, and spin wave excitation through magnetoelastic coupling is demonstrated by magnetic field dependent changes in transmission. Finally, coherent control of NV centers by these acoustically generated spin waves is demonstrated, and a method for determining their wavelength using NV-based measurements is presented.

Chapter 2. NV center

The nitrogen vacancy (NV) center is a point defect in the diamond crystal lattice, formed when a substitutional nitrogen atom, a neighboring vacancy, and an extra electron combine within a diamond structure. The advantages of NV centers can be assessed in terms of the DiVincenzo criteria [22], which specify the requirements for a physical system to serve as a qubit platform for quantum computing. First, well defined qubits and scalability: the electronic structure of an NV center provides two levels that can encode a qubit, and the number of qubits can be scaled by exploiting interactions with nearby nuclear spins [23]. Second, initialization: the NV center can be initialized optically into a well defined state. Third, coherence: NV centers exhibit coherence times that are long compared to the timescales required for state manipulation [24]. Fourth, gate operations: microwave fields enable coherent control of the qubit states. Fifth, measurement: the qubit state can be read out optically through spin dependent fluorescence.

Among these strengths, the realization of entanglement between multiple NV centers is particularly important. If entangled NV-NV networks can be implemented to achieve scalability using NV centers alone, they would constitute an even more powerful qubit platform.

This chapter discusses these advantages of NV centers and introduces experimental demonstrations that show these properties. In this chapter, we provide an overview of the

NV center as a solid state spin qubit and introduce the key physical concepts required for the later chapters. We first describe the ground state spin Hamiltonian and its splitting under magnetic fields. Based on this framework, we explain coherent microwave control via Rabi oscillations, followed by the optical initialization and readout mechanisms arising from the NV photodynamics. We then discuss decoherence processes and coherence preserving pulse protocols, and finally present experimental demonstrations of continuous wave electron spin resonance (CWESR) and Rabi measurements used in this dissertation.

2.1 Hamiltonian of the NV center

Interactions between an NV center and external fields are described by its ground state spin Hamiltonian. The NV center has an $S = 1$ electronic ground state triplet with spin sublevels $m_s = 0, \pm 1$. In the absence of external fields, the Hamiltonian is

$$H/\hbar = DS_z^2 \tag{2.1}$$

where D is the zero field splitting (ZFS) parameter separating the $m_s = 0$ level from the $m_s = \pm 1$ levels. At room temperature, the ZFS is $D/2\pi \approx 2.87$ GHz [25]. The operator S_z denotes the spin-1 operator along the z axis. For an NV center, the coordinate system is defined such that the z axis lies along the nitrogen-vacancy symmetry axis. The x axis may be chosen along any of the three equivalent carbon axes perpendicular to z; owing to the threefold rotational symmetry of the defect, these choices are physically equivalent. The $m_s = 0$ state is separated from the $m_s = \pm 1$ states by D, while the $m_s = \pm 1$ states are degenerate in the absence of transverse strain or electric fields. In practice, transverse strain and electric fields introduce an additional term that lifts the degeneracy

of the $m_s = \pm 1$ manifold and can mix these states. Although this contribution is often small in bulk diamond, it becomes crucial when NV centers are coupled to mechanical excitations. The strain related terms in the Hamiltonian will be provided in Chapter 4. A common perturbation to the NV center is an applied magnetic field. Including the Zeeman interaction, the Hamiltonian becomes

$$H/\hbar = DS_z^2 + \gamma \vec{B} \cdot \vec{S} \tag{2.2}$$

where the magnetic field is $\vec{B} = (B_x, B_y, B_z)$, the spin operator is $\vec{S} = (S_x, S_y, S_z)$, and γ is the electron gyromagnetic ratio, $\gamma/2\pi \approx 2.8$ MHz/G. A magnetic field applied along the z direction lifts the degeneracy of the $m_s = \pm 1$ levels, giving eigenenergies $E_{m_s}/\hbar = Dm_s^2 + \gamma B_z m_s$, and hence a splitting between the $m_s = +1$ and $m_s = -1$ states of $2\gamma B_z$. In contrast, transverse magnetic field components (B_x or B_y) mix the $m_s = 0$ and $m_s = \pm 1$ states, so that the resulting eigenstates are superpositions of the zero field basis states. In most experiments, a bias magnetic field is applied to remove the $m_s = \pm 1$ degeneracy so that the two allowed electron spin resonance transitions, $m_s = 0 \leftrightarrow +1$ and $m_s = 0 \leftrightarrow -1$, can be independently resolved. Therefore, the field is aligned as closely as possible with the NV z axis while minimizing transverse components. Under this aligned field condition, the Hamiltonian reduces to

$$H/\hbar = DS_z^2 + \gamma B_z S_z \tag{2.3}$$

In this dissertation, a DC magnetic field is used to tune the NV electron spin transition frequencies to achieve frequency matching with the spin wave.

2.2 Rabi oscillation

Rabi oscillations serve two important purposes in this dissertation. First, they establish the basis for coherent qubit control and the calibration of π and $\pi/2$ microwave pulses. Second, the measured Rabi frequency provides a direct and quantitative probe of the driving field amplitude, which we later use to estimate the strength of microwave stray fields generated by spin waves. Transverse components of the field, B_x and B_y, drive transitions between $|0\rangle$ and $|\pm1\rangle$. This is conveniently described in the rotating frame. For an NV center aligned with a static magnetic field along the NV axis, the Hamiltonian is given by Equation 2.3. In the basis $|+1\rangle, |0\rangle, |-1\rangle$, it can be written as

$$H/\hbar = \begin{bmatrix} \omega_{+1} & 0 & 0 \\ 0 & 0 & 0 \\ 0 & 0 & \omega_{-1} \end{bmatrix} \tag{2.4}$$

where $\omega_{+1}(= D + \gamma B_z)$ and $\omega_{-1}(= D - \gamma B_z)$ are the transition angular frequencies between $|0\rangle$ and $|+1\rangle$, and between $|0\rangle$ and $|-1\rangle$, respectively. When an AC magnetic field is applied, the interaction term is $\gamma \vec{B}_{\mathrm{ac}}(t) \cdot \vec{S} = \gamma[B_x(t)S_x + B_y(t)S_y]$. For simplicity, we consider only an x polarized field $B_x(t) = B_x \cos \omega t$. Using the spin-1 operator $\langle \pm 1 | S_x | 0 \rangle = 1/\sqrt{2}$, the Hamiltonian becomes

$$H/\hbar = \begin{bmatrix} \omega_{+1} & \frac{\gamma B_x}{\sqrt{2}} \cos \omega t & 0 \\ \frac{\gamma B_x}{\sqrt{2}} \cos \omega t & 0 & \frac{\gamma B_x}{\sqrt{2}} \cos \omega t \\ 0 & \frac{\gamma B_x}{\sqrt{2}} \cos \omega t & \omega_{-1} \end{bmatrix} \tag{2.5}$$

To handle the time dependent terms, we move to a rotating frame using the unitary transformation

$$U = \begin{bmatrix} e^{i\omega t} & 0 & 0 \\ 0 & 1 & 0 \\ 0 & 0 & e^{i\omega t} \end{bmatrix} \tag{2.6}$$

A state $|\psi\rangle$ in the lab frame is related to the rotating frame state $|\tilde{\psi}\rangle$ by

$$|\tilde{\psi}\rangle = U|\psi\rangle, \qquad |\psi\rangle = U^{\dagger}|\tilde{\psi}\rangle \tag{2.7}$$

Starting from the Schrödinger equation,

$$\begin{aligned} i\frac{\partial}{\partial t}|\psi\rangle &= H|\psi\rangle \\ i\frac{\partial}{\partial t}\left(U^{\dagger}|\tilde{\psi}\rangle\right) &= H\left(U^{\dagger}|\tilde{\psi}\rangle\right) \\ iU\frac{\partial U^{\dagger}}{\partial t}|\tilde{\psi}\rangle + i\frac{\partial}{\partial t}|\tilde{\psi}\rangle &= UHU^{\dagger}|\tilde{\psi}\rangle \end{aligned}$$

we obtain the rotating frame Schrödinger equation $i\partial_t|\tilde{\psi}\rangle = \tilde{H}|\tilde{\psi}\rangle$ with

$$\tilde{H} = UHU^{\dagger} - iU\frac{\partial U^{\dagger}}{\partial t} \tag{2.8}$$

Explicitly,

$$\tilde{H}/\hbar = \begin{bmatrix} \omega_{+1} - \omega & \frac{\gamma B_x}{\sqrt{2}}e^{i\omega t}\cos\omega t & 0 \\ \frac{\gamma B_x}{\sqrt{2}}e^{-i\omega t}\cos\omega t & 0 & \frac{\gamma B_x}{\sqrt{2}}e^{-i\omega t}\cos\omega t \\ 0 & \frac{\gamma B_x}{\sqrt{2}}e^{i\omega t}\cos\omega t & \omega_{-1} - \omega \end{bmatrix} \tag{2.9}$$

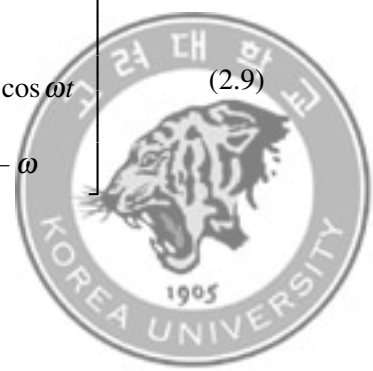

The terms $e^{\pm i\omega t}\cos\omega t$ contain rapidly oscillating contributions. Under the rotating wave approximation (RWA), the fast terms at 2ω are neglected:

$$e^{i\omega t}\cos\omega t = \frac{1}{2}e^{i\omega t}\left(e^{i\omega t}+e^{-i\omega t}\right) \approx \frac{1}{2} \tag{2.10}$$

Thus, the effective time independent Hamiltonian is

$$\tilde{H}/\hbar = \begin{bmatrix} \Delta_{+1} & \frac{\gamma B_x}{2\sqrt{2}} & 0 \\ \frac{\gamma B_x}{2\sqrt{2}} & 0 & \frac{\gamma B_x}{2\sqrt{2}} \\ 0 & \frac{\gamma B_x}{2\sqrt{2}} & \Delta_{-1} \end{bmatrix} \tag{2.11}$$

where $\Delta_{\pm 1} = \omega_{\pm 1} - \omega$ are the detunings between the spin transition frequencies and the rotating frame frequency. The off-diagonal terms induce transitions between the states, while large detuning suppresses these transitions. For example, when $\Delta_{+1} \gg \Delta_{-1}, \gamma B_x/(2\sqrt{2})$, the $|+1\rangle$ state is effectively decoupled and the system reduces to the two level subspace spanned by $|0\rangle, |-1\rangle$:

$$\tilde{H}/\hbar = \begin{bmatrix} 0 & \frac{\gamma B_x}{2\sqrt{2}} \\ \frac{\gamma B_x}{2\sqrt{2}} & \Delta_{-1} \end{bmatrix} \tag{2.12}$$

To determine the time evolution, we write $|\tilde{\psi}\rangle = \alpha|\tilde{0}\rangle + \beta|\tilde{-1}\rangle$. This evolution can be expressed:

$$\dot{\alpha} = -i\frac{\gamma B_x}{2\sqrt{2}}\beta$$
$$\dot{\beta} = -i\left(\frac{\gamma B_x}{2\sqrt{2}}\alpha + \Delta_{-1}\beta\right)$$

Combining these gives

$$\ddot{\alpha} + i\Delta_{-1}\dot{\alpha} + \left(\frac{\gamma B_x}{2\sqrt{2}}\right)^2 \alpha = 0 \tag{2.13}$$

The solutions are

$$\alpha(t) = e^{-i\frac{\Delta_{-1}}{2}t}\left[A\cos\left(\frac{\Omega t}{2}\right) + B\sin\left(\frac{\Omega t}{2}\right)\right]$$
$$\beta(t) = e^{-i\frac{\Delta_{-1}}{2}t}\frac{\sqrt{2}}{\gamma B_x}\left[(\Delta_{-1}A + i\Omega B)\cos\left(\frac{\Omega t}{2}\right) + (\Delta_{-1}B - i\Omega A)\sin\left(\frac{\Omega t}{2}\right)\right]$$

where A and B are determined by the initial conditions and

$$\Omega = \sqrt{\Delta_{-1}^2 + \left(\frac{\gamma B_x}{\sqrt{2}}\right)^2} \tag{2.14}$$

is the generalized Rabi frequency. For the initial state $|\tilde{0}\rangle$ ($P_0 = |\alpha(0)|^2 = 1$, $P_{-1} = |\beta(0)|^2 = 0$), the populations oscillate at frequency $\Omega/2$ with amplitude

$$\frac{\left(\gamma B_x/\sqrt{2}\right)^2}{\Delta_{-1}^2 + \left(\gamma B_x/\sqrt{2}\right)^2} \tag{2.15}$$

showing that larger detuning reduces the transition probability. Figure 2.1 presents Rabi oscillations for different detunings, where increased detuning leads to less efficient transitions. A larger AC field amplitude yields a higher Rabi frequency. By measuring Ω, the AC magnetic field amplitude can be quantified. In this dissertation, we use Rabi oscillations to determine the amplitude of the stray field generated by spin waves. Beyond serving as a probe, Rabi oscillations enable coherent control of the qubit state: an ideal π pulse occurs at $\tau = \pi/\Omega$, while a $\pi/2$ pulse preparing the superposition $|\psi\rangle = \frac{1}{\sqrt{2}}(|0\rangle + |-1\rangle)$ occurs at $\tau = \pi/(2\Omega)$. In practice, perfectly coherent Rabi oscillations are an idealization;

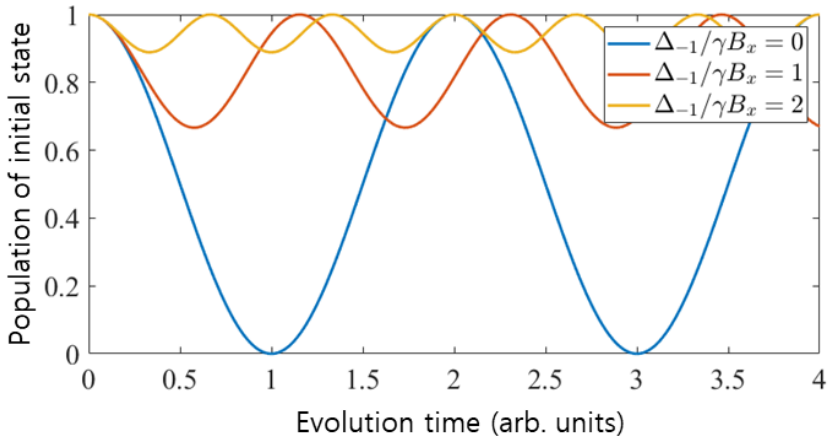

Figure 2.1: Rabi oscillations depend on the detuning condition. The behavior of Rabi oscillations is governed by the detuning. As the detuning becomes large relative to the amplitude of the driving AC magnetic field, the population oscillations exhibit a reduced amplitude. In addition, the Rabi frequency is modified by the detuning, leading to a corresponding change in the oscillation frequency.

detuning, imperfect pulse control, and finite pulse duration errors distort the oscillations and produce state errors. To mitigate these effects, more sophisticated pulse sequences are employed for qubit manipulation [26–34].

2.3 Photodynamics of the NV center

One of the prominent properties of the NV center is that its spin state can be optically read out and initialized. This section introduces the photodynamics of the NV center, following the model of J.-P. Tetienne et al. (2012), where further details can be found [35]. To describe photodynamics of the NV center, we consider eight effective relevant states: triplet ground states ($m_s = +1, 0, -1$), triplet excited states ($m_s = +1, 0, -1$), and

two intermediate singlet states (Figure 2.2 (a)). Optical excitation drives transitions from the ground state manifold to the excited state manifold. During radiative decay back to the ground state manifold, photons are emitted, and the decay pathways depend on the spin projection m_s. In particular, the $m_s = \pm 1$ in excited states have an additional non-radiative decay channel through the singlet states. This spin dependent fluorescence enables optical readout of the ground state spin. Moreover, the singlet mediated pathway is spin nonconserving: population in the $m_s = \pm 1$ excited states preferentially relaxes to the $m_s = 0$ ground state. As a result, after sufficient optical pumping, the NV center is polarized into the $m_s = 0$ ground state.

Because the NV center energy levels are split according to m_s, an external magnetic field modifies the level structure. A transverse magnetic field mixes the ground and excited state spin manifolds, which reduces the number of photons emitted under optical excitation. Figure 2.2 (b) shows the calculated photoluminescence (PL) of an NV center under an external magnetic field, illustrating how the field modifies the NV optical cycle. As the magnitude of the magnetic field component transverse to the NV symmetry axis increases, the PL decreases. This reduction is attributed to transverse field induced spin state mixing, which diminishes the efficiency of optical spin polarization and enhances intersystem crossing into non-radiative pathways, thereby lowering the observed PL. Beyond this transverse field dependence, the PL is also modulated by the magnetic field component along the NV axis. In particular, characteristic features appear near ~ 50 mT and ~ 100 mT, corresponding to the excited state level anti-crossing (ESLAC) and the ground state level anti-crossing (GSLAC), respectively. Near these axial field resonances, the relevant triplet spin sublevels become strongly mixed, altering the optical pumping dynamics and consequently the PL. Overall, these results highlight that NV PL is sensitive to both the magnitude and the direction of the applied magnetic field. For PL-based

NV measurements, it is therefore essential to align the magnetic field with the NV axis so as to minimize transverse components and maintain high PL, while also accounting for PL variations that can occur in the vicinity of the ESLAC and GSLAC fields. At these fields, the $m_s = 0$ and $m_s = -1$ levels approach a level anticrossing, which enhances state mixing and results in a sharp reduction in PL. Therefore, when accurate NV center measurements are required, PL reductions due to magnetic field induced mixing must be taken into account. Unless a specific experiment requires otherwise, the magnetic field should be aligned with the NV axis to maintain strong optical contrast.

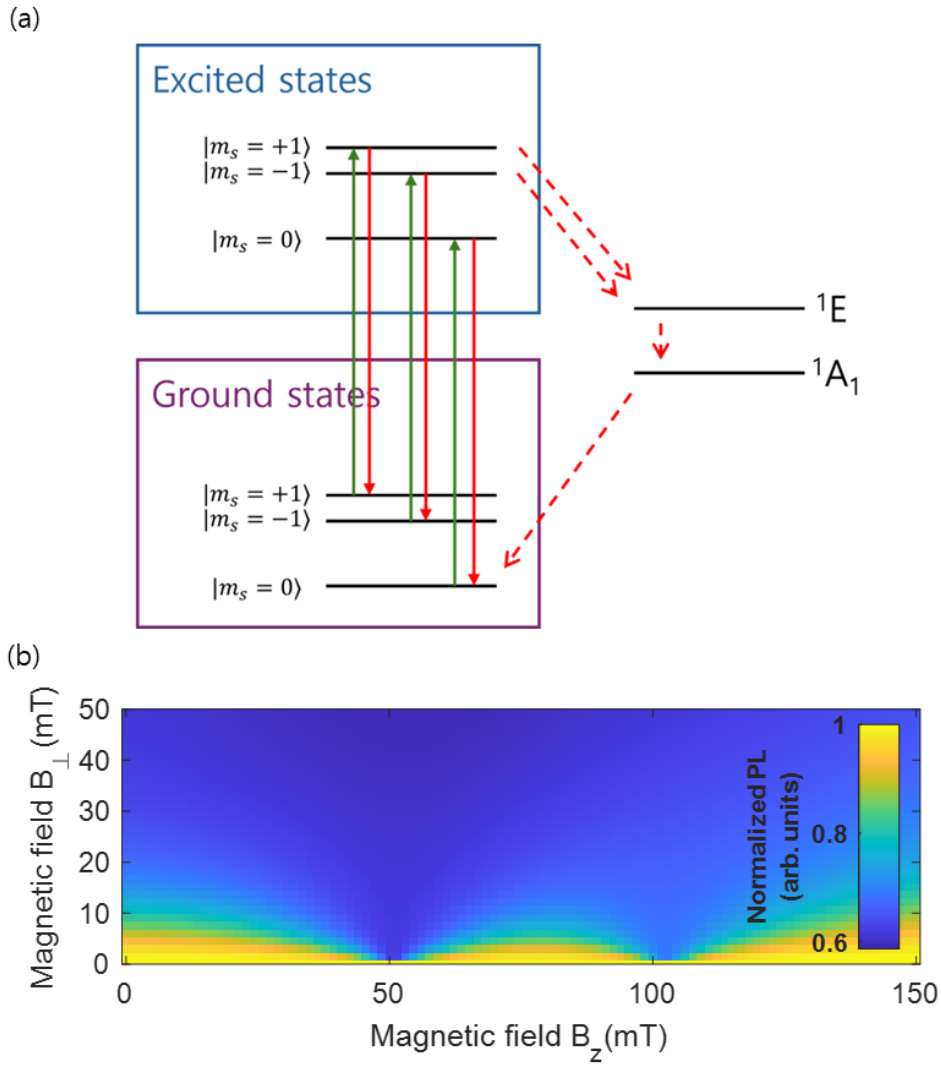

Figure 2.2: Photodynamics of NV centers. (a) Optical transitions between ground states and excited states. Ground state population is optically excited by a green laser and subsequently decays radiatively to the ground state, emitting photons. The $m_s = \pm 1$ excited states have an additional non-radiative decay pathway (red dashed lines). (b) Calculated NV PL as a function of magnetic field. B_z denotes the field component along the NV axis, and $B_\perp$ denotes the transverse component.

2.4 Decoherence

Quantum states are inevitably coupled to their environment. Because the environment interacts with a quantum system, the system gradually loses the information encoded in its state, leading to decoherence [36]. This process is unavoidable and ultimately limits practical applications of quantum coherence. Decoherence is typically characterized by the timescale over which a quantum state preserves its coherence. Since multiple mechanisms can contribute, coherence loss can manifest in different ways. Two characteristic times are commonly used to quantify these processes: T_1 and T_2 [37]. The T_1 relaxation time (energy relaxation time) quantifies energy exchange between the system and its environment, the timescale over which the system approaches thermal equilibrium. For example, an NV center can exchange energy with the surrounding lattice, causing its spin population to relax toward the thermal state. The T_2 dephasing time (phase relaxation time) quantifies the loss of phase coherence, the timescale over which the relative phase of a superposition state becomes randomized. In NV centers, dephasing often arises from interactions with nearby nuclear spins. These spins generate a local magnetic field at the NV center and fluctuations of this field cause the NV spin phase to wander, resulting in decoherence. A convenient way to visualize a qubit state is the Bloch sphere representation. In this picture, a qubit state corresponds to a vector on (or inside) a unit sphere. For a pure qubit state $|\psi\rangle = a|0\rangle + b|1\rangle$, the density matrix is

$$\rho = |\psi\rangle\langle\psi| = \begin{bmatrix} \rho_{00} & \rho_{01} \\ \rho_{10} & \rho_{11} \end{bmatrix} = \begin{bmatrix} |a|^2 & ab^* \\ a^*b & |b|^2 \end{bmatrix} \tag{2.16}$$

The corresponding Bloch vector coordinates (x, y, z) are given by

$$\begin{aligned} x &= 2\,\mathrm{Re}[\rho_{01}] = 2\,\mathrm{Re}[ab^*] \\ y &= 2\,\mathrm{Im}[\rho_{01}] = 2\,\mathrm{Im}[a^*b] \\ z &= \rho_{00} - \rho_{11} = |a|^2 - |b|^2 \end{aligned} \tag{2.17}$$

For example, the states $|\pm\rangle = \frac{1}{\sqrt{2}}(|0\rangle \pm |1\rangle)$ correspond to Bloch vectors $(x, y, z) = (\pm 1, 0, 0)$; thus, $|\pm\rangle$ lie along the x axis. In the Bloch sphere picture, T_1 relaxation causes longitudi-

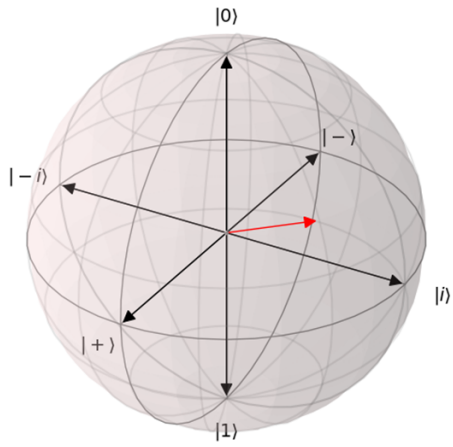

Figure 2.3: Bloch sphere. A qubit state can be represented as a vector. The north pole corresponds to $|0\rangle$, whereas the south pole corresponds to $|1\rangle$. When a qubit is in a superposition of $|0\rangle$ and $|1\rangle$, the vector lies away from the poles, pointing to a position on the surface of the sphere.

nal decay, a change in the z component of the Bloch vector toward its thermal value. In contrast, T_2 processes induce decay of transverse coherence in the xy plane, shortening the Bloch vector length. Quantum information can be encoded either in the populations

(longitudinal component) or in the relative phase (transverse component). Therefore, a qubit loses different types of information on different timescales. The coherence times are key properties of a qubit: longer coherence times imply slower information loss and are essential for high fidelity quantum control. To mitigate decoherence, it is important first to engineer qubits with intrinsically long coherence times. For NV centers, deep defects located far from the surface typically exhibit longer coherence times than shallow ones, because surface related noise sources accelerate decoherence [38]. Beyond defect depth, several experimental conditions can be optimized to suppress dominant noise channels [39]. Nevertheless, since the environment is always present, decoherence cannot be completely eliminated even in an idealized device. As an alternative, various control protocols have been developed to extend the effective coherence time [31, 40].

2.5 Spin echo

Spin echo sequences are fundamentally designed to refocus dephasing and extend spin coherence times. However, by selectively suppressing quasi-static noise while remaining sensitive to time dependent interactions, they also serve as powerful tools for probing time varying interactions. In this dissertation, the spin echo pulse sequence is used to probe strain interactions with the NV center. A Bloch sphere representation of the sequence is shown in Figure 2.4. To probe the interaction, the spin state is first rotated to the equator. In the equatorial plane, the state acquires a phase during the free evolution time ($T = 2\tau$) due to the strain interaction. A π pulse is applied halfway through this evolution period so that the phase contribution from the AC strain is refocused and adds constructively, rather than canceling. Finally, the state is rotated again to project the accumulated phase onto the z axis for readout. The accumulated phase from the time

evolution operator appears in the measured spin state population as

$$P(T) = \frac{1}{2}\left(1 + \cos\theta(T)\right) \tag{2.18}$$

In the spin echo sequence, the spin state is flipped at the midpoint of the total evolution time T in order to accumulate the phase arising from an AC varying interaction. We drive two mechanical modes simultaneously, where ω_1 and ω_2 are the angular frequencies of the first and second modes, respectively, and ϕ_1 and ϕ_2 are their corresponding driving phases. For simplicity, we consider only the parallel strain coupling $G_{\parallel}$. Here, G_1 and G_2 denote the parallel coupling strengths associated with the first and second mechanical modes, respectively. $G_i/2\pi$ is the frequency shift in Hz. The accumulated phase is then

$$\begin{aligned}\theta(T = 2\tau) = 2\pi\Bigg[&\int_0^{\tau} \left(G_1\cos(\omega_1 t + \phi_1) + G_2\cos(\omega_2 t + \phi_2)\right) dt \\ &- \int_{\tau}^{2\tau} \left(G_1\cos(\omega_1 t + \phi_1) + G_2\cos(\omega_2 t + \phi_2)\right) dt\Bigg]\end{aligned} \tag{2.19}$$

During the evolution, the spin coherence decays exponentially. Including this decoherence, the echo signal becomes

$$P_{\text{echo}}(T = 2\tau) = \frac{1}{2}\left[1 + e^{-T/T_2}\cos\left(\sum_{i=1,2}\frac{4G_i}{f_i}\sin^2\left(\frac{\pi f_i T}{2}\right)\sin\left(\pi f_i T + \phi_i\right)\right)\right] \tag{2.20}$$

where $f_i = \omega_i/2\pi$ are the mechanical mode frequencies in Hz. In chapter 4, we measured strain couplings using spin echo sequence and observed selective tuning in the strain coupling through this measurement.

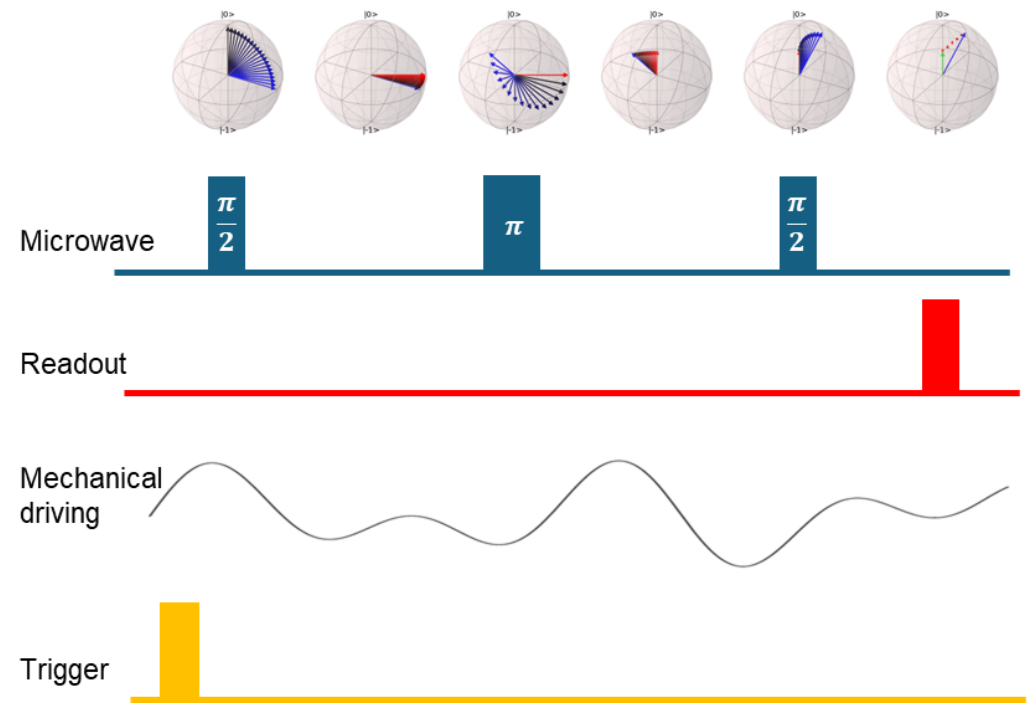

Figure 2.4: Spin echo sequence. Starting from an initial state prepared in $|0\rangle$, a microwave $\pi/2$ pulse creates a superposition state. During free evolution, the qubit acquires a phase due to external interactions. A subsequent π pulse inverts the state so that an additional phase is accumulated with opposite sign, refocusing static contributions while enhancing AC components. Finally, a second $\pi/2$ pulse converts the accumulated phase into a measurable population difference, enabling readout of the phase and extraction of the external interaction. This protocol is therefore sensitive to AC strain generated by mechanical driving. By synchronizing the microwave pulses and the external drive to a common trigger, the phase of the drive can be controlled.

2.6 Experimental demonstration

To determine the ground state transition frequencies of an NV center, we use CWESR. Continuous microwave driving induces population transitions between the qubit states. By sweeping the microwave frequency, resonant and off-resonant conditions can be distinguished through the resulting change in population. For NV centers, these population changes are read out optically via fluorescence photon counts. Because the spin resonances shift under an external magnetic field, the transition frequencies can be tuned accordingly. Owing to this field dependence, the NV center can also serve as a magnetic field sensor.

After determining the electron spin resonance frequency using CWESR, microwave pulses are employed to manipulate the qubit state. A resonant microwave field drives coherent transitions between the spin levels, and the pulse duration determines the final qubit state. Figure 2.5 shows an example of Rabi oscillations. From these data, we extract the π pulse time, the duration required to invert the population between two states. Rabi measurements are therefore fundamental for coherent qubit control. In addition, the Rabi oscillation frequency is proportional to the applied microwave field amplitude, enabling estimation of the microwave field strength. In this sense, the NV center can also function as a microwave power sensor [41, 42]. In our experiments on yttrium iron garnet (YIG) films, we likewise use the NV center as a sensor for the local microwave magnetic field [43].

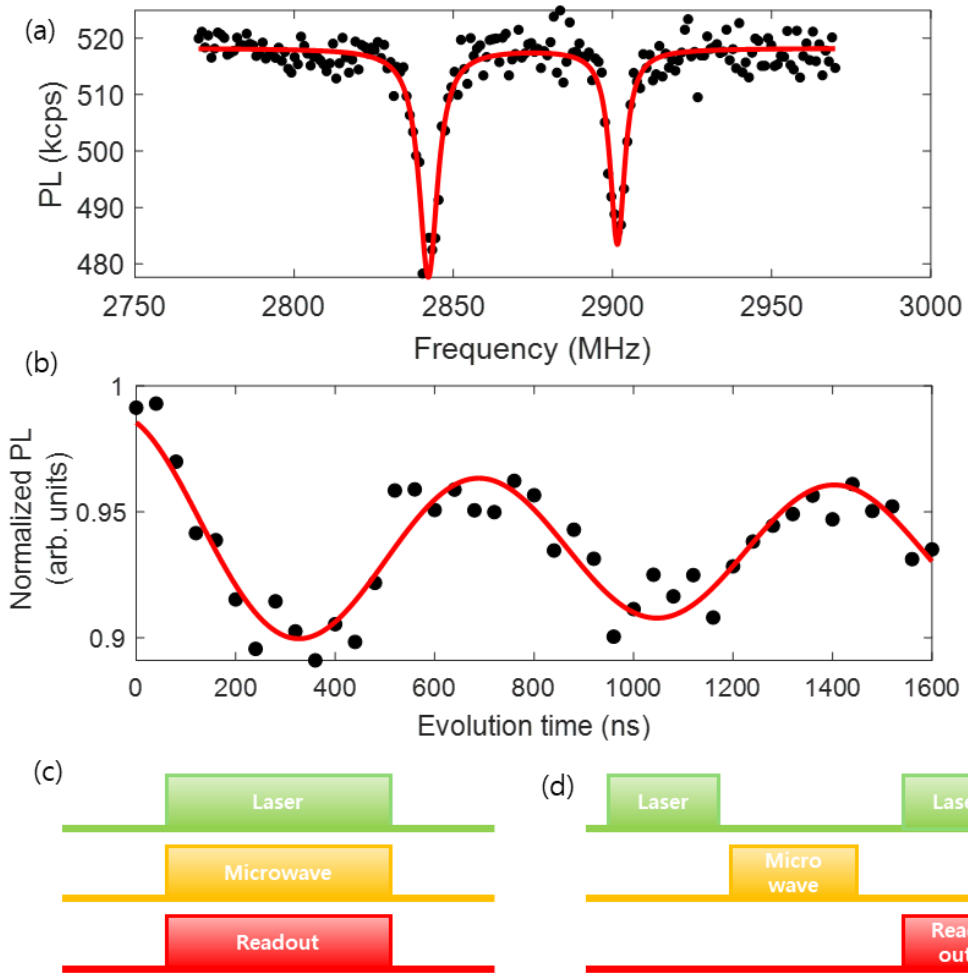

Figure 2.5: Measurement of the NV center. (a) CWESR spectra are used to determine the NV center's electronic resonance frequencies. The splitting between the two resonances can be tuned by an external magnetic field. (b) Measurement of the Rabi oscillation. The vertical axis corresponds to the population in $|0\rangle$. The oscillations indicate that the population coherently oscillates between $|0\rangle$ and $|-1\rangle$. (c) CWESR measurement sequence. Optical pumping, microwave driving, and photon counting are performed simultaneously while the microwave frequency is swept. (d) Rabi measurement sequence. The first laser pulse initializes the spin, and the second laser pulse is used for readout. The duration of the microwave pulse between the two laser pulses is swept. Photon counting is performed after the microwave pulse.

Chapter 3. Experimental setup

In this chapter, we introduce the experimental setup designed to verify the properties of NV centers discussed in the previous chapters. A confocal microscopy setup was built to leverage the optical properties of the NV centers. In addition, a microwave system was implemented to perform measurements such as CWESR and Rabi oscillations for coherent spin manipulation. Furthermore, a vacuum chamber setup was developed to investigate interactions between the NV centers and strain.

3.1 Optical system

The optical system is used for NV center readout. We built a confocal microscopy setup. Figure 3.1 (a) shows the overall layout of optics. A 532 nm laser (MLL-III-532, CNI Laser) is used to excite the NV center. A filter wheel is placed in front of the laser to adjust its power; the wheel contains several neutral density (ND) filters with different transmissions. The green beam is then sent to an acousto-optic modulator (AOM, ATM-200C1, IntraAction). Owing to the acousto-optic effect, the direction of the diffracted beam is deflected, and with a fast RF driver the AOM serves as a high speed optical switch. The light is delivered through an optical fiber and directed to a dichroic beam splitter. This dichroic element separates the 532 nm excitation laser from the NV fluo-

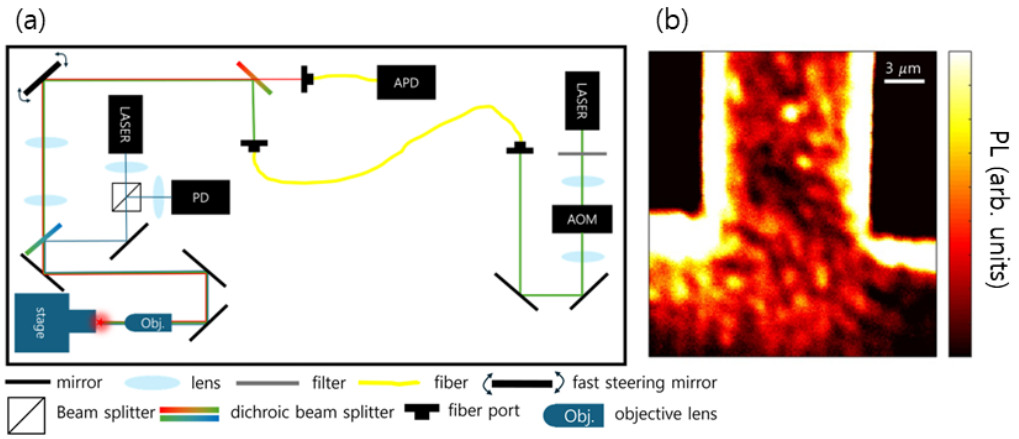

Figure 3.1: Optical system for NV center measurement. (a) Schematic of optical system. (b) Image acquired using the confocal microscopy setup. This image was taken near the base of the diamond cantilever sample.

rescence. Because the NV center has a zero phonon line at 637 nm and emits a phonon sideband from 637 to 850 nm, the resulting fluorescence passes through the dichroic beam splitter and is directed to a fiber port coupled to an avalanche photodiode (APD, SPCM-AQRH-10-FC, Excelitas). In contrast, the excitation beam is reflected by the dichroic beam splitter and sent to a fast steering mirror (FSM, FSM-300-02, Newport). The FSM tilts the reflected beam, thereby changing the incident angle into a pair of telescope lenses. The telescope consists of two convex lenses with focal lengths f_1 and f_2. The first lens is placed at a distance f_1 from the FSM, and the second lens is positioned $f_1 + f_2$ from the first lens. When the incident beam from the FSM has an angle θ_{in}, the focal position after the second lens shifts laterally. Thus, the angular deflection of the FSM is converted into a lateral displacement of the focus, enabling confocal scanning by sweeping the FSM angle. The excitation beam is focused onto the NV center, which emits red fluorescence photons. These photons retrace the same optical path back to the dichroic beam split-

ter, where they are transmitted to the APD. With this optical setup, photon counts are collected at each lateral position to form a PL image map. From this map, the NV center position can be identified; by focusing on that position, fluorescence signals from a single NV center are obtained for subsequent measurements. Figure 3.1 (b) shows a fluorescence image acquired by confocal microscopy. Bright, localized spots correspond to NV centers or surface contaminants. When a diamond sample is loaded for the first time, the confocal image is often cloudy rather than showing well localized points. To remove bright contaminants, we illuminate the affected area with a focused laser. After several hours of illumination, the PL in that region decreases, resulting in a clearer image with distinct pointlike emitters. In addition, a 450 nm laser is included in the setup. When the sample mounted on the stage is a mechanical oscillator, this laser is directed onto the oscillating structure, and an optical interferometer is used to characterize its mechanical motion.

3.2 Electronics

Microwave fields are used to manipulate the quantum state of the NV center. To this end, we control the microwave frequency, power, and pulse timing. Figure 3.2 illustrates the electronic system used in this work. A signal generator (SG384, Stanford Research Systems) produces microwaves with the desired frequency and power. The output is gated by a microwave switch (ZASWA-2-50DR+, Mini-Circuits), which transmits the signal only when a TTL control input is high. This TTL signal is provided by a PulseBlaster (PBESR-PRO-500-PCI, SpinCore). After the switch, the microwave is amplified through an amplifier (ZHL-16W-43+, Mini-Circuits) and delivered to a printed circuit board (PCB) mounted near the sample. To protect the electronics from damage due to re-

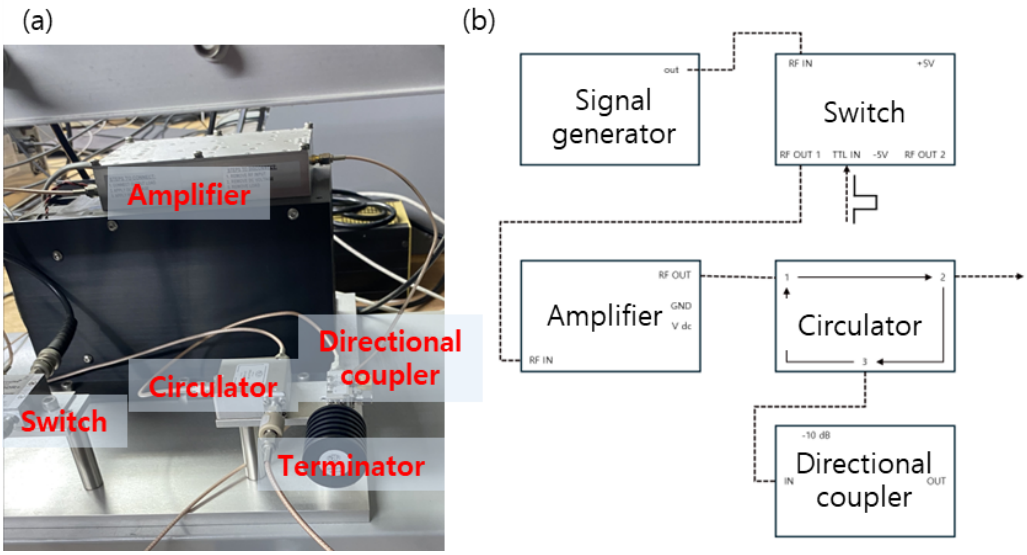

Figure 3.2: Electronic system. (a) Photograph of electronics system. (b) The signal generator produces the microwave signal and sends it to a switch, which controls the output so that microwaves are delivered with the desired timing. The signal is then amplified to the required power and transmitted to a PCB that contains the microwave circuitry needed for the experiment. To protect the circuit, a circulator is inserted in the line so that any microwaves reflected from the PCB are routed to a termination through a separate path.

flected power, a circulator routes any reflected signal into a separate path that terminates at a matched load. We used two different PCB designs, as shown in Figure 3.3. In designing the PCBs, the coplanar waveguide (CPW) parameters were chosen to set the signal line width and the gap between the signal and ground lines, based on the substrate thickness and dielectric constant, so as to achieve a 50 Ω characteristic impedance. To connect the PCB to the sample, we use wire bonding. Thin gold wires are bonded between the metal pads on the sample and the gold pads on the PCB. We tested several types of metal pads for reliable bonding. For easy and mechanically robust connections, the pads should be sufficiently large, thicker than 100 nm, and made of gold. For mechanical driving, we

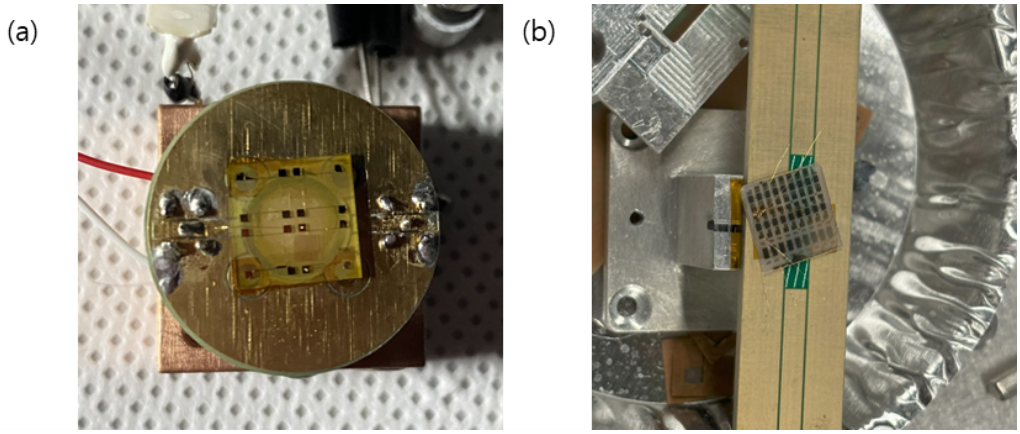

Figure 3.3: Various PCB designs. (a) A circular PCB. The signal pad is located at the center, and ground pads are placed on both sides. The sample is mounted on top of the PCB, and wire bonding is used to connect the signal and ground pads to the sample, respectively. (b) A PCB with one elongated side was fabricated to fit the scanning setup.

use a vacuum chamber to achieve low pressure. A window is installed on the top of the chamber to allow the laser beam to enter. Figure 3.4 shows the chamber and the sample holder. The sample holder has a supporting arm that positions the sample close to the window. Beneath the sample, a piezoelectric actuator is mounted for mechanical driving, and it is secured by a bolt inserted from below.

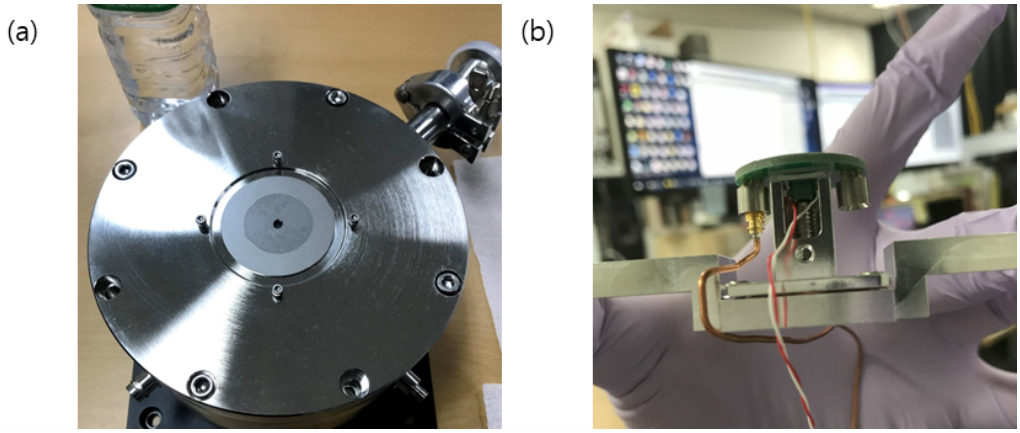

Figure 3.4: Setup used for strain measurements. (a) A vacuum chamber designed for experiments under low pressure conditions. Optical signals from the NV centers inside the chamber can be collected through the viewport at the center of the top flange. (b) A sample holder installed inside the vacuum chamber. A piezoelectric actuator is placed beneath the sample mount to drive mechanical oscillations.

Chapter 4. Strain interaction

Mechanical waves are a form of wave motion that transport energy through the collective motion of particles. They manifest across a wide range of length scales, from geophysical phenomena such as earthquakes to practical applications such as acoustic waves in mobile devices. In solid-state platforms, mechanical excitations are often realized as confined mechanical modes in resonators, enabling controlled and coherent interactions with localized qubits. Recently, there has been growing interest in using such mechanical excitations as a medium for quantum communication between spatially separated qubits. To employ mechanical excitations as an information carrier, it is essential to develop a detailed understanding of their interaction mechanisms with solid-state quantum systems.

The interaction between NV centers and mechanical waves can be realized in two primary ways. First, mechanical waves can generate strain fields in the diamond host crystal containing NV centers [44–47]. Such strain modifies the interatomic distances of the lattice and consequently perturbs the NV center's electronic structure, leading to shifts and mixing in the electron spin resonance transitions. Second, a mechanical resonator can produce an oscillating magnetic field gradient, such that the motion of the resonator modulates the local magnetic field experienced by a nearby NV center and thereby affects its spin dynamics through magnetic coupling [48, 49].

Strain mediated coupling is particularly attractive because it can drive transitions

between the $m_s = +1$ and $m_s = -1$ sublevels within the ground state spin triplet, enabling control pathways that are difficult to access using conventional magnetic field based techniques. In this dissertation, we investigate the interaction between NV centers and mechanical waves via strain field.

We first present a theoretical description of how strain influences the NV center ground state triplet levels, and we describe the fabrication process of diamond mechanical resonators designed to generate AC strain. We then report measurements of strain–NV interactions using spin echo measurements. Next, we demonstrate, via spin echo measurements, that the strain couplings produced by two simultaneously driven mechanical modes add. Finally, through simulations of a membrane hosting nearly degenerate mechanical modes, we show that by controlling the relative amplitudes and phases of the modes and combining their contributions, the effective strain coupling can be tailored for a desired operation.

4.1 Theoretical description

To quantify the strain coupling strength $G_{\parallel}$ and $G_{\perp}$, we first express the mechanical deformation as a strain tensor and relate its components to the NV spin Hamiltonian. Strain quantifies the deformation of a material under applied stress.

$$\varepsilon_{ij} = \frac{1}{2}\left(\frac{\partial u_i}{\partial j} + \frac{\partial u_j}{\partial i}\right), \qquad (i = x, y, z) \tag{4.1}$$

Here, u_i is the displacement of a particle along i direction. It is represented by a 3×3 tensor whose components describe deformation along different directions.

$$\varepsilon = \begin{bmatrix} \varepsilon_{xx} & \varepsilon_{xy} & \varepsilon_{xz} \\ \varepsilon_{yx} & \varepsilon_{yy} & \varepsilon_{yz} \\ \varepsilon_{zx} & \varepsilon_{zy} & \varepsilon_{zz} \end{bmatrix} \tag{4.2}$$

The strain tensor is symmetric, $\varepsilon_{ij} = \varepsilon_{ji}$ and therefore has six independent components $(\varepsilon_{xx}, \varepsilon_{xy}, \varepsilon_{xz}, \varepsilon_{yy}, \varepsilon_{yz}, \varepsilon_{zz})$. All components enter the strain affected Hamiltonian [50].

$$\begin{aligned} H_{strain} = & [d_{A_1}\varepsilon_{zz} + d_{A_1'}(\varepsilon_{xx} + \varepsilon_{yy})]S_z^2 \\ & - [d_E(\varepsilon_{xx} - \varepsilon_{yy}) + d_{E'}(\varepsilon_{xz} + \varepsilon_{zx})](S_x^2 - S_y^2) \\ & + [d_E(\varepsilon_{xy} + \varepsilon_{yx}) + d_{E'}(\varepsilon_{yz} + \varepsilon_{zy})](S_x S_y + S_y S_x) \end{aligned} \tag{4.3}$$

These coefficients $(d_{A_1}, d_{A_1'}, d_E, d_{E'})$ are strain coupling constants, the labels (A or E) indicate the symmetry of the corresponding strain components. Strain with A symmetry affects the ZFS, whereas strain with E symmetry mixes the $|\pm 1\rangle$ states. In the following, we compute these effective couplings from the strain profile of the cantilever. In this Hamiltonian, the xyz coordinate system is defined with respect to the diamond crystal axes. The diamond lattice has four equivalent $\langle 111 \rangle$ directions. An NV center has a symmetry axis along the nitrogen-vacancy direction, which we define as the z axis. The x axis is chosen to be perpendicular to z within the plane spanned by z and one of the three remaining crystal directions. The y axis is then defined to complete a right-handed coordinate system with x and z. Because the NV center has rotational symmetry about the nitrogen-vacancy axis, the specific crystal direction used to define the x axis is not

important. As mentioned above, strain has directional components, so the strain profile obtained in the cantilever frame must be converted into the NV center frame. Only the strain components expressed in the NV frame enter Equation (4.3), allowing us to extract $G_{\|}$ and $G_{\perp}$ for a given NV orientation. The cantilever coordinate system $(x'y'z')$ is defined by $x' \parallel [1\bar{1}0]$, $y' \parallel [001]$, and $z' \parallel [110]$. The four possible nitrogen-vacancy axes are

$$\begin{aligned} v_1 &= [\bar{1}\bar{1}1] \\ v_2 &= [\bar{1}1\bar{1}] \\ v_3 &= [1\bar{1}\bar{1}] \\ v_4 &= [111] \end{aligned} \tag{4.4}$$

All these directions are represented in cantilever $(x'y'z')$ frame

$$\begin{aligned} v_1 &= \frac{1}{\sqrt{3}}(0,1,-\sqrt{2}) \\ v_2 &= \frac{1}{\sqrt{3}}(-\sqrt{2},-1,0) \\ v_3 &= \frac{1}{\sqrt{3}}(\sqrt{2},-1,0) \\ v_4 &= \frac{1}{\sqrt{3}}(0,1,\sqrt{2}) \end{aligned} \tag{4.5}$$

To construct NV center frame (x,y,z), we take the z axis to lie along the nitrogen-vacancy, one of the vectors ,v_i (for example, v_2). x axis perpendicular to z axis and lies in plane made by two vectors, v_i and v_j (for example, v_3). The y axis is defined by the cross

product z and x.

$$\begin{aligned} z' &= v_2 = \frac{1}{\sqrt{3}}(-\sqrt{2}, -1, 0) \\ x' &= \frac{v_3 - (v_2 \cdot v_3)v_2}{|v_3 - (v_2 \cdot v_3)v_2|} = \frac{1}{\sqrt{3}}(1, \sqrt{2}, 0) \\ y' &= z' \times x' = (0, 0, 1) \end{aligned} \tag{4.6}$$

Using these vectors, the transform matrix from (xyz) to $(x'y'z')$ is

$$Q_{23} = \begin{bmatrix} x' \\ y' \\ z' \end{bmatrix} = \frac{1}{\sqrt{3}} \begin{bmatrix} 1 & -\sqrt{2} & 0 \\ 0 & 0 & \sqrt{3} \\ -\sqrt{2} & -1 & 0 \end{bmatrix} \tag{4.7}$$

Finally, strain defined in $x'y'z'$ frame is $\varepsilon_{xyz} = Q_{23}\varepsilon_{x'y'z'}Q_{23}^T$.

$$\varepsilon_{xyz} = Q_{23}\varepsilon_{x'y'z'}Q_{23}^T = \frac{1}{3} \begin{bmatrix} 1 & -\sqrt{2} & 0 \\ 0 & 0 & \sqrt{3} \\ -\sqrt{2} & -1 & 0 \end{bmatrix} \varepsilon_{x'y'z'} \begin{bmatrix} 1 & 0 & -\sqrt{2} \\ -\sqrt{2} & 0 & -1 \\ 0 & \sqrt{3} & 0 \end{bmatrix} \tag{4.8}$$

Similarly, other choices of v_i and v_j define a corresponding matrix Q_{ij} for each nitrogen-vacancy orientation. We obtain the strain profile analytically or numerically, transform it into NV center frame, and then compute the resulting couplings using Equation (4.3).

$$H_{strain} = G_{\parallel}S_z^2 + G_{\perp,x}(S_x^2 - S_y^2) + G_{\perp,y}(S_xS_y + S_yS_x)$$

$$G_{\parallel} = [d_{A_1}\varepsilon_{zz} + d_{A_1'}(\varepsilon_{xx} + \varepsilon_{yy})] \tag{4.9}$$

$$G_{\perp,x} = -[d_E(\varepsilon_{xx} - \varepsilon_{yy}) + d_{E'}(\varepsilon_{xz} + \varepsilon_{zx})] \tag{4.10}$$

$$G_{\perp,y} = [d_E(\varepsilon_{xy} + \varepsilon_{yx}) + d_{E'}(\varepsilon_{yz} + \varepsilon_{zy})] \tag{4.11}$$

$\varepsilon_{xx}, \varepsilon_{xy}, \varepsilon_{xz}, \varepsilon_{yy}, \varepsilon_{yz}, \varepsilon_{zz}$ is converted from strain in cantilever frame $(x'y'z')$. All coupling coefficients are referred to [50] ($d_{A_1} = -3$ GHz, $d_{A_1'} = 11.2$ GHz, $d_E = 2$ GHz, $d_{E'} = 6.6$ GHz). Using the transformed strain components, we can compute the longitudinal and transverse strain coupling strengths $G_{\parallel}$ and $G_{\perp}$, which are then probed via phase locked spin echo measurements.

4.2 Resonator fabrication

Unlike the cantilever geometry used in previous experiments [51], we aim to fabricate resonators with a significant shear strain component and with two mechanical modes whose frequencies are close to each other within the kHz range. To this end, we explored T-shaped and U-shaped cantilevers. COMSOL simulations were employed to predict the vibrational mode shapes and resonance frequencies. The T- and U-shaped structures have a wide transverse geometry, which supports two characteristic modes: an in-phase vibration of the two arms, referred to as the flexural mode, and an out-of-phase vibration, referred to as the torsional mode. In general, the flexural mode frequency is primarily determined by the longitudinal length of the resonator, whereas the torsional mode frequency is mainly governed by its transverse length. Using simulations, we estimate the strain coupling strengths from the strain profiles after transforming them into the NV center frame. Because the largest strain occurs near the base of these resonators, we select an NV center located close to the base to maximize the coupling. To realize the designed

diamond resonators, we fabricate them from a diamond plate into the target geometry. We start with a 2 mm $\times$ 2 mm $\times$ 500 μm diamond plate. Through a commercial service, the plate is sliced and polished into three pieces, each with a thickness of approximately 20μm. The fabrication process consists of three main steps: bonding, etching, and patterning.

	Flexural mode	Torsional mode
U-shaped	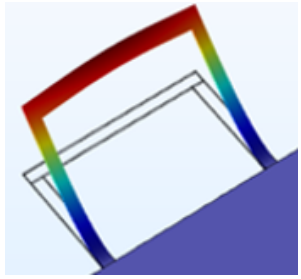	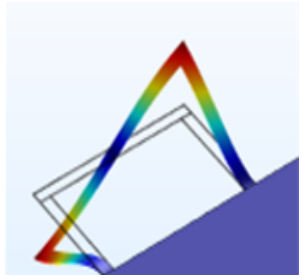
T-shaped	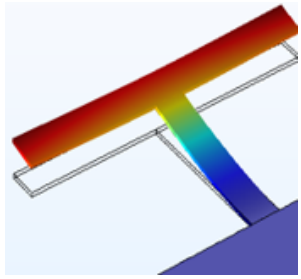	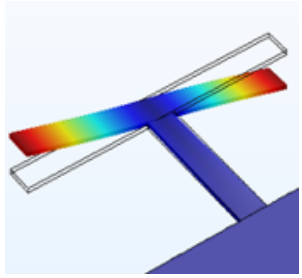

Table 4.1: Mode shapes for U-shaped and T-shaped resonator. These resonators have two distinct modes, which are divided by flexural mode and torsional mode.

- Bonding

Bonding is for easy handling during fabrication process. Since the diamond plate is small (2 mm $\times$ 2 mm), handling it without bonding to a substrate can easily lead to damage, resulting in breakage or contamination. We use silicon oxide layer as bonding layer between diamond plate and silicon substrate. Silicon oxide layer is formed by FOX (flowable oxide). FOX is spun on silicon substrate. Cleaned diamond plate is put on coated

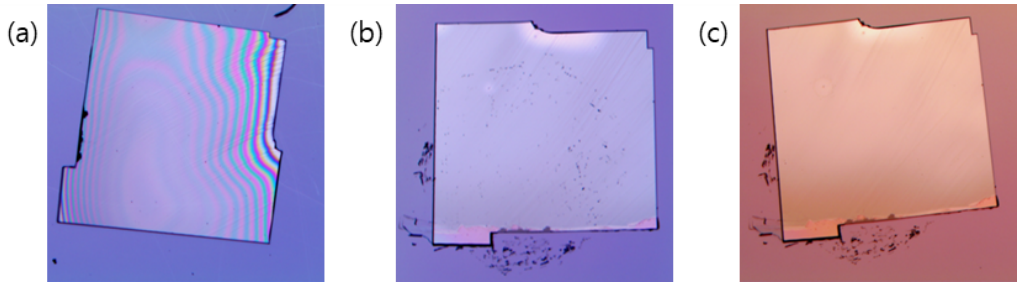

Figure 4.1: Bonding preparation step before loading in the bonder. (a) Diamond plate cleaning. Interference patterns are visible on the diamond surface due to a gap between the diamond and the substrate. The rough, uneven edges result from the diamond polishing and slicing processes. (b) Diamond plate bonded with FOX. Before being placed on a hot plate, small contamination was introduced by the cotton swab and the weight used during pressing. Under the diamond plate, FOX spreads and bonds between the diamond and the substrate. The disappearance of the interference pattern indicates that the gap is filled with FOX. (c) After heating on a hot plate, contamination on the diamond surface was removed.

substrate (Figure 4.1 (a)). We press the stack with a weight for 1 - 2 min and use a cotton swab to ensure a uniform bonding layer (Figure 4.1 (b)).The sample is then baked on a hot plate at 160 °C (Figure 4.1 (c)). After hot plate, this stack is on the wafer bonder. Wafer bonder is fabrication equipment for bonding a wafer stack. The wafer bonder offers several adjustable parameters including temperature, temperature rising time, pressing force or vacuum pressure. We tested these parameters under various conditions; in some runs the diamond cracked or the bonding layer was nonuniform. These parameter have to be checked in several tests.

The parameters used were 420 °C, with 1 hour to take from room temperature to 420 °C, vacuum and 1.2 kg/cm^2 pressing force. Although the process was carried out with the same parameters each time, the outcomes varied from run to run. We attribute this variability to differences in the quality and completeness of the bonding preparation

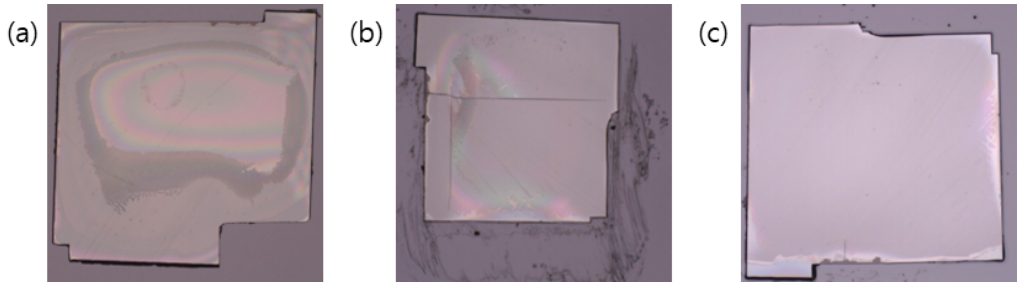

Figure 4.2: Results of the bonding process. (a) Unsuccessful case showing interference patterns on the diamond plate, suggesting a nonuniform bonding layer. (b) Unsuccessful case in which the diamond plate cracked during wafer bonding. (c) Successful case that was used for the subsequent process.

steps before loading the sample into the bonder.

- Etching

The diamond plate is 20 μm thick. To thin it down to our designed thickness, 1 μm, we etch diamond plate. Etching process is done in ICP-RIE. Before the main process, we test etching rate by step etching and profiler. As shown in Figure 4.3, etching diamond covering half of the surface shows a step depth. During several tries, we estimated etching rate as 1.7 μm/h (Figure 4.3 (c)). From etching rate, Etching time is about 9 hours. The etching time was divided into several cycles, between each cycle, monitoring thickness using scanning electron microscopy (SEM), cleaning surface using IPA and acetone. We use two different recipes, Ar/Cl_2 and O_2 etching, the former guarantees smooth surface but slow etching rate, the latter provides a fast etch rate but results in poor surface quality. To reach 1 μm thick, for smooth surface, Ar/Cl_2 etching is used. After patterning, defining resonator shape, O_2 etching is used for fast process.

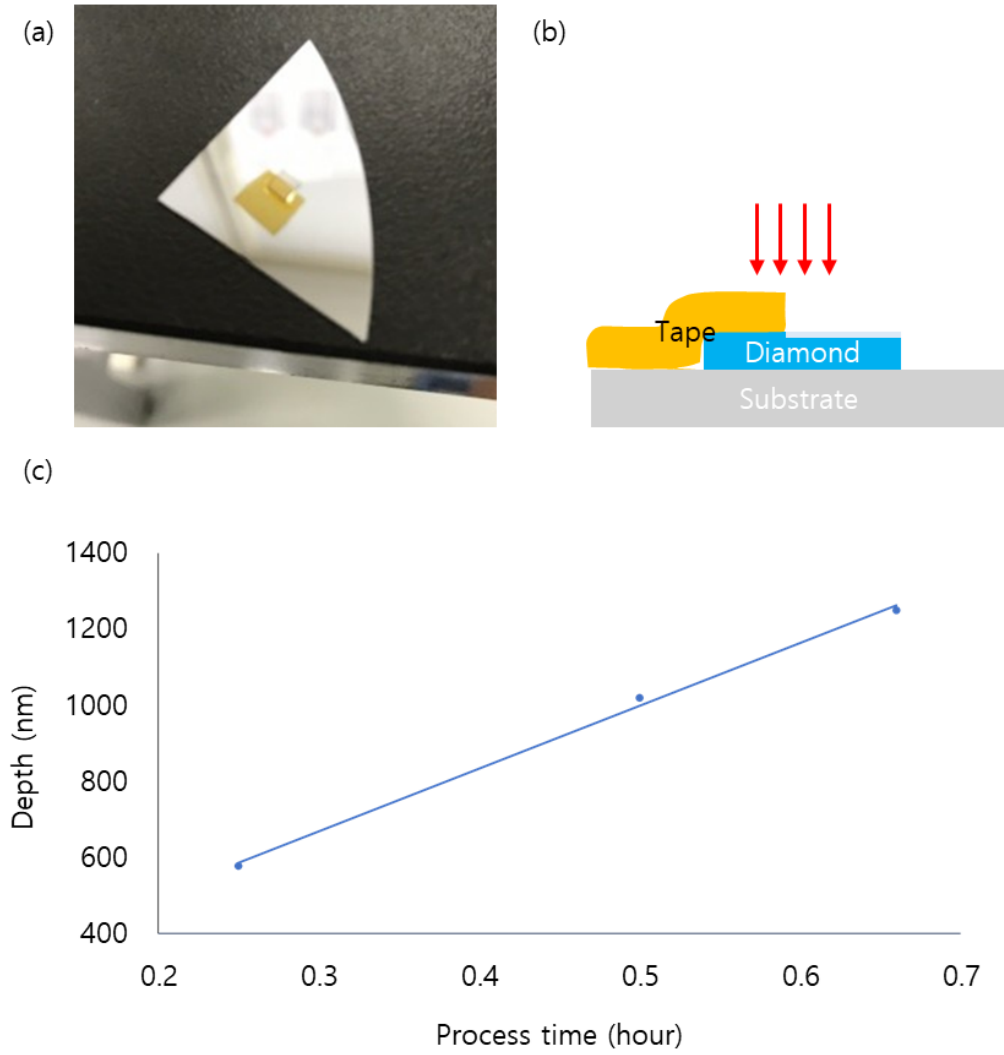

Figure 4.3: Step etching to characterize the etch rate. (a) A Teflon tape mask covers half of the diamond. (b) Schematic of the step etching procedure: the tape covered region remains intact while the exposed region is etched; after the tape is removed, a surface step is formed at the boundary. (c) Step height measurement using an optical profiler. The estimated etch rate for the Ar/Cl_2 recipe is 1.7 μm/h.

- Patterning

The patterning process follows a standard photolithography procedure. An aluminum layer is used as the etch mask (Figure 4.4(b)). After the etching step, the aluminum layer is removed using the developer MIF 300. At this point, the diamond resonators remain attached to the substrate through the underlying oxide layer. To release the resonators, we etch the silicon oxide beneath them by wet etching with buffered oxide etchant (BOE). This BOE step removes the oxide layer and breaks the bonding between the diamond and the substrate (Figure 4.4(c)). After wet etching, the diamond resonators are fully released and no longer bonded to the substrate. Excessive wet etching can produce an overly large undercut region, which degrades the quality of the mechanical motion. As shown in Figure 4.4(c), the surface color provides a visual indication of any remaining bonding layer. Therefore, the BOE etching should be performed in multiple short steps, with essential optical microscope inspection between steps. Figures 4.4(d) and (e) show tilted view SEM images confirming that the diamond structures are suspended above the substrate.

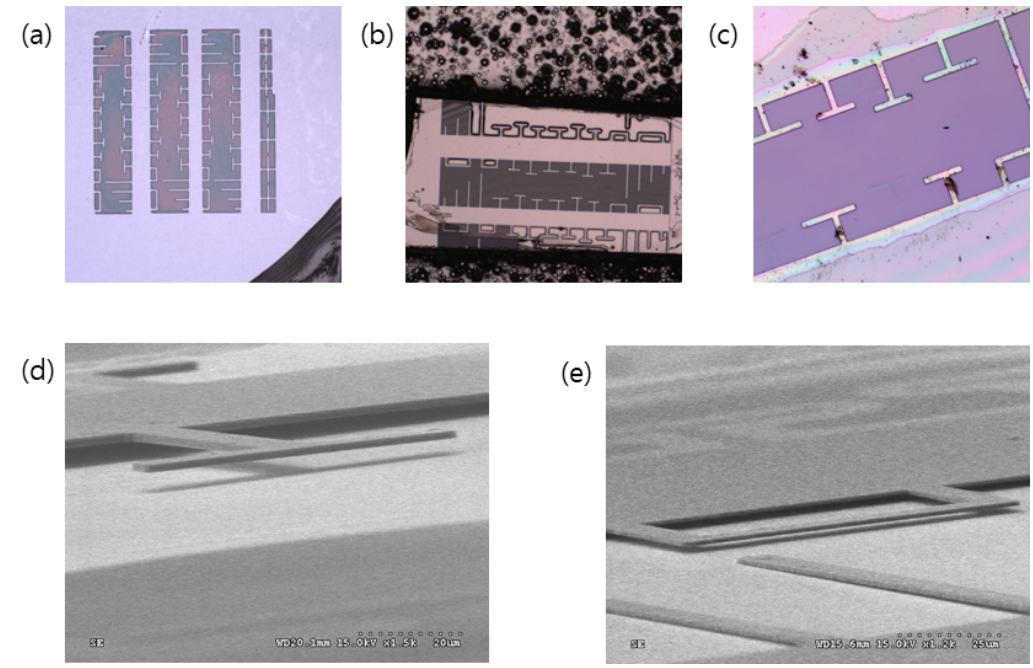

Figure 4.4: Patterning process. (a) A patterned photoresist layer on the diamond plate. (b) A metal mask on the plate. (c) Optical image of the final cantilever array. (d) SEM image of a T-shaped cantilever. (e) SEM image of a U-shaped cantilever.

4.3 Spin echo experiments

Before measuring strain coupling to the NV center, the mechanical motion of the diamond structure is characterized using an optical interferometer. As shown in Figure 4.5 (a), the laser is focused at the point where the mechanical amplitude is maximized. By sweeping the drive frequency, we record the photodetector signal to obtain the mechanical response spectrum. As Figure 4.5 (b) and (c), signal of each mode shows resonance frequency and width of mechanical mode. We assign 582 kHz as flexural mode and 876 kHz as torsional mode. To study the interaction between the NV center and the AC strain field, Spin echo measurement is used. Figure 4.6 (a) and (b) show spin echo measurement for two mechanical driving. These results demonstrate coupling bewteen the strain field and the NV center for each mechanical driving mode. To verify our phase control capability, we perform phase locked spin echo measurements. Figure 4.6 (c) and (d) show spin echo data acquired at a fixed drive phase. When the phase of the mechanical drive is changed by 45°, the phase of the spin echo signal shifts by the same amount. These results confirm that the spin echo sequence is synchronized with the mechanical drive and that spin echo signals at a well defined phase can be reliably acquired.

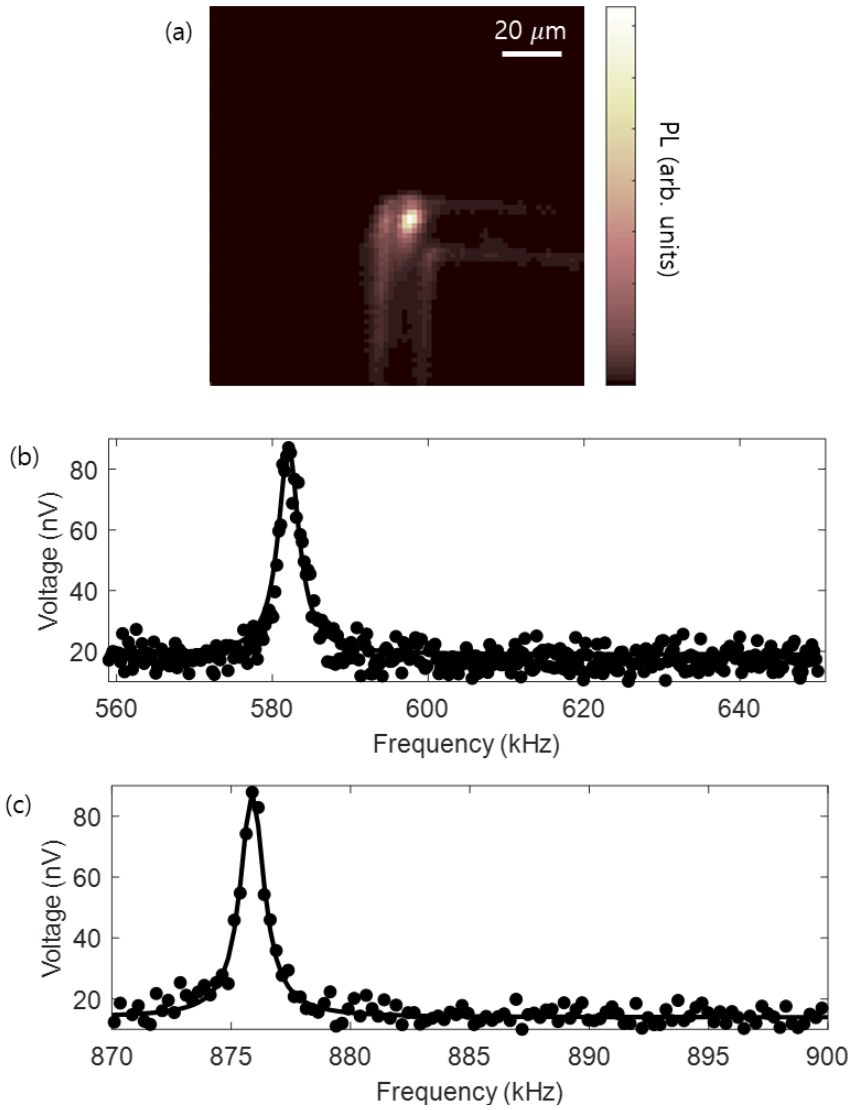

Figure 4.5: Optical interferometry. (a) Image when a laser is focused on a cantilever tip. The vibration modes can be identified by using an interferometer to measure the distance between the cantilever tip and the substrate below. (b) Frequency sweep for flexural mode. Its resonance frequency is 582 kHz. (c) Frequency sweep for torsional mode. Its resonance frequency is 876 kHz.

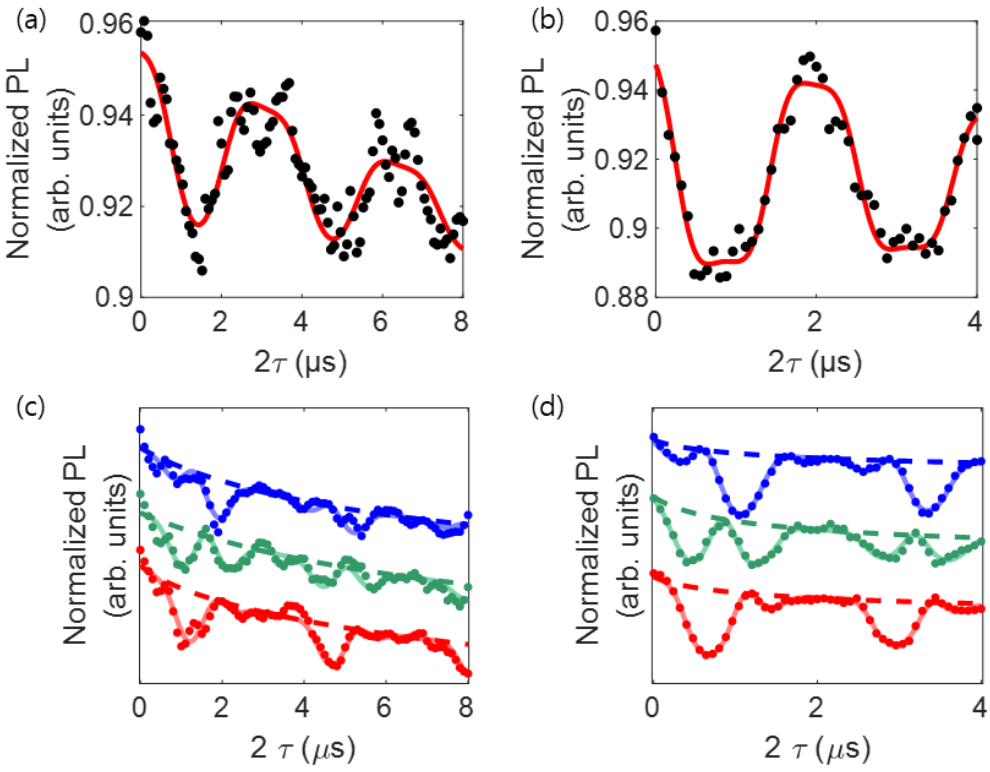

Figure 4.6: Spin echo measurements for (a) 582 kHz driving and (b) 876 kHz driving. Phase lock spin echo measurements for (c) 582 kHz driving and (d) 876 kHz driving. The measurement was repeated with three successive 45° phase shifts, and the results show a corresponding continuous 45° shift.

Beyond single mode frequency, we study spin echo measurement with two different frequencies simultaneously. Figure 4.7 shows phase dependent spin echo data. We vary the phase of the 876 kHz drive in 45° steps while keeping the 582 kHz drive phase fixed. Fitted phase values from spin echo measurement are agreed with controlled input phase of mechanical drivings. Another spin echo measurement is variation in amplitude of mechanical driving. Figure 4.8 shows amplitude variation spin echo measurements. α is ratio of coupling strength $G_{582\text{kHz}}/G_{876\text{kHz}}$. Figure 4.7 and Figure 4.8 show that, like single frequency spin echo, two frequencies spin echo measurements change by phase and amplitude. 4 parameters, strain coupling strength and phase, G_1, G_2, ϕ_1 and ϕ_2 can be controlled by one's purpose, engineering strain coupling.

Strain coupling engineering has a flaw that two mechanical modes have different frequency so that combination of G_1, G_2, ϕ_1 and ϕ_2 cannot yield perfect cancellation of strain coupling. We design a membrane that has nearly degenerate mode frequencies. Membrane is slightly asymmetric, 100.5 μm × 99.5 μm which breaks degeneracy of mode frequencies.Two mode frequencies are 5.81 MHz and 5.88 MHz expected from COMSOL simulation. By combining the two modes with appropriate amplitudes and phases, we achieve advanced engineering strain coupling. At a certain position of membrane, $G_{\parallel}$ and $G_{\perp}$ are derived from strain profile. We choose two combinations of driving amplitude, in-phase 1:1 and out-of-phase 0.5:1. Equal amplitude driving with in phase makes large $G_{\parallel}$ and small $G_{\perp}$ and 0.5:1 driving amplitude with out of phase makes large $G_{\perp}$ and small $G_{\parallel}$. Figure 4.9 (b) shows $G_{\parallel}$ coupling by spin echo signal. Blue data shows large $G_{\parallel}$ coupling. To demonstrate perpendicular coupling, $G_{\perp}$, Rabi oscillation between $|+1\rangle$ and $|-1\rangle$ induced by $G_{\perp}$. Figure 4.9 (c) shows $G_{\perp}$ coupling by strain Rabi oscillation between $|+1\rangle$ and $|-1\rangle$. Simulation data in Figure 4.9 (b) and (c) are acquired by Qutip simulation tool.

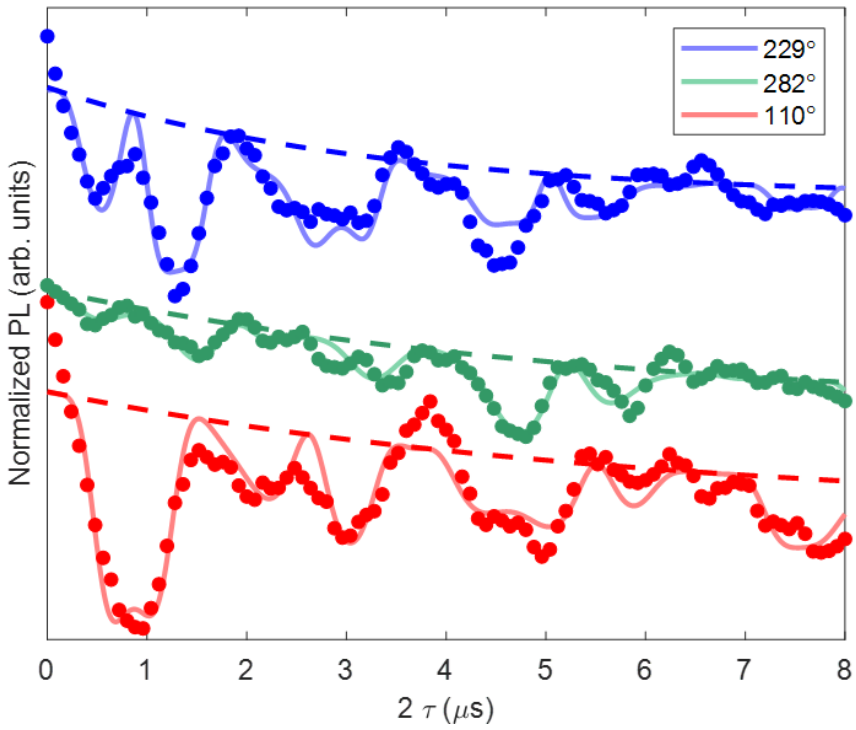

Figure 4.7: Phase variation of echo measurements. Phase lock spin echo measurements for two modes driving with difference phase input. The measurement was repeated with three successive 90° phase shifts, and the fitted results show a corresponding continuous 90° shift.

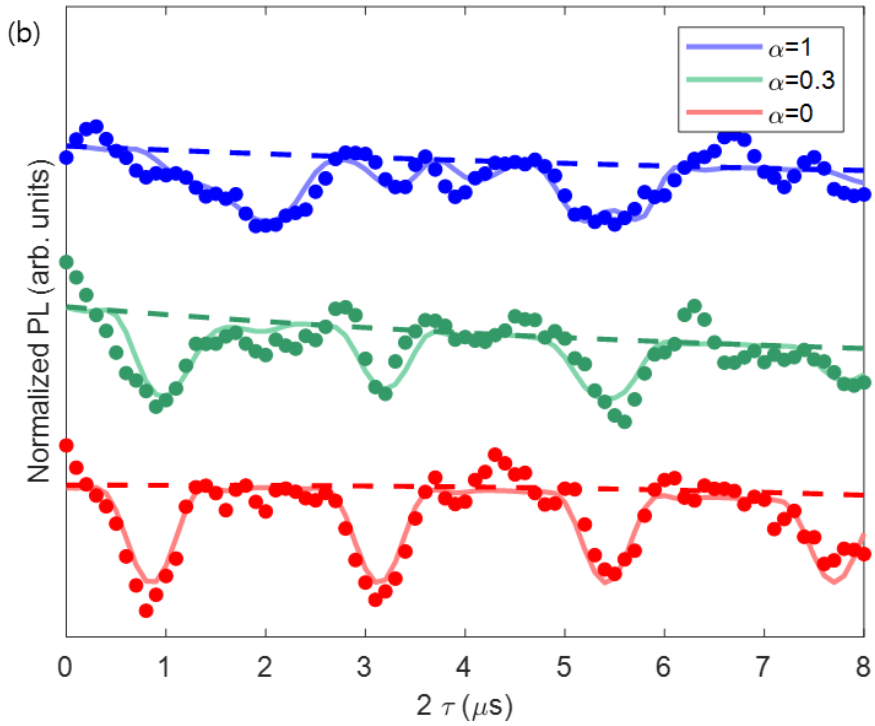

Figure 4.8: Amplitude variation of echo measurements. Phase lock spin echo measurements for two modes driving with amplitude variation. The red data is acquired by driving only 876 kHz mode. α corresponds to relative amplitude of two modes.

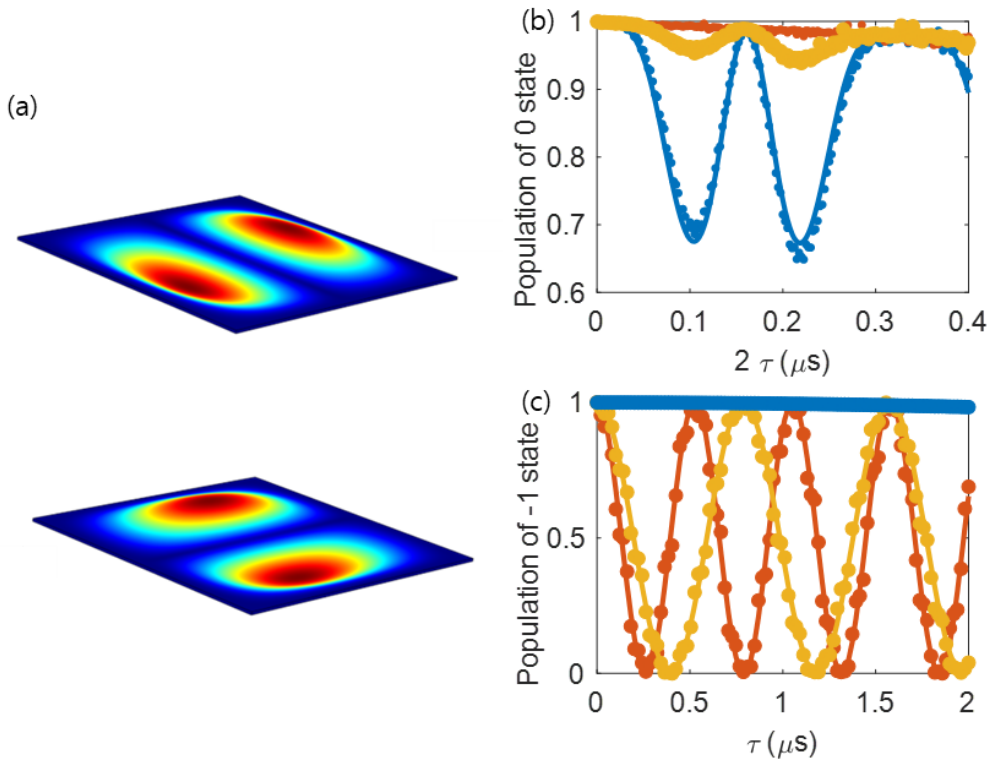

Figure 4.9: (a) Mode shapes of membrane. The asymmetric square membrane has two nearly degenerate modes of which frequencies are 5.81 MHz and 5.88 MHz (b) Spin echo simulation showing $G_{\parallel}$ be controlled larger or smaller than single mode driving. The yellow plot is for single mechanical mode. The blue plot is multimode driving for larger parallel coupling. The red plot is multimode driving for smaller parallel coupling. (c) Rabi oscillation showing $G_{\perp}$ larger or smaller than single mode driving. The yellow plot is for single mechanical mode. The blue plot is multimode driving for smaller perpendicular coupling. The red plot is multimode driving for larger perpendicular coupling.

4.4 Conclusions

In this chapter, we investigated the interaction between NV centers in diamond and mechanically generated strain fields. To produce mechanical waves, we fabricated diamond vibrating resonators designed to support two vibrational modes, and characterized their mode spectra and profiles using optical interferometric readout. We then quantified the strain coupling to NV center by employing phase locked spin echo measurements. These experiments allowed us to extract the effective coupling strengths and to directly observe how the echo response depends on the amplitude and phase of the mechanical drive. We demonstrated that simultaneous driving of two mechanical modes enables partial control of the effective strain coupling through interference. Furthermore, numerical simulations showed that in membranes hosting nearly degenerate vibrational modes, the strain coupling can be tuned with nearly complete selectivity, offering a route toward engineered strain environments for NV spin control. For practical manipulation of NV centers via strain, achieving a sufficiently large coupling strength is essential. In this context, the mechanical quality factor of the diamond resonator plays a central role, as it determines how efficiently mechanical energy is stored and thus how large a strain amplitude can be generated for a given drive power. Enhancing the quality factor therefore directly improves the strain coupling strength. Two complementary strategies can be pursued. First, resonator fabrication can be further optimized to minimize intrinsic dissipation. Second, extrinsic losses can be mitigated by operating under improved environmental conditions such as low pressure and low temperature. Together, these advances would extend coherence of the mechanical modes and enable stronger, more controllable strain driving, thereby making strain based NV control a more powerful tool for hybrid quantum systems and related sensing technologies.

Chapter 5. Spin wave interaction

A magnon is the quantum of a spin wave, and a spin wave is a collective oscillation of electron spins in a magnetic material. Unlike charge currents, spin waves do not produce Joule heating, making magnons promising candidates for low power integrated chip devices. Accordingly, extensive research has explored magnon based signal processing and computing [52–54]. Experimentally, a simple way to excite coherent spin waves is to place a current carrying wire near the magnetic material. When a microwave current flows through a wire adjacent to a magnetic film, it generates an oscillating magnetic field that induces spin precession in the film.

Spin waves can be detected in two main ways. One approach is transport detection using inductive antennas [55]. In this configuration, two antennas are positioned near the magnetic film: one for excitation and the other for detection. By measuring the transmission parameters (S_{12} or S_{21}) with a vector network analyzer (VNA), the power carried by spin waves from the excitation antenna to the detection antenna can be quantified. This method is straightforward, however, because the spin wave propagation region is not directly probed by an antenna, it is difficult to determine what occurs within the magnetic film during transmission.

The other approach is direct imaging of spin waves. Because spin wave propagation involves spatially and temporally oscillating magnetization, measuring these oscillations

enables visualization of the wave dynamics. Such measurements can be performed using several techniques. Time resolved magneto-optic Kerr effect (TR-MOKE) imaging exploits the magneto-optic Kerr effect, in which the polarization of light reflected from a magnetized surface changes [56]. X-ray magnetic circular dichroism (XMCD) measures the difference in absorption between left- and right-circularly polarized X-rays. Direct imaging techniques are particularly useful for investigating wave properties such as wavelength and group velocity. This chapter discusses the dispersion of spin waves, presents transmission measurements obtained using a VNA, and validates NV center state manipulation mediated by spin waves.

5.1 Theoretical description of spin waves

Spin wave dynamics are governed by the Landau-Lifshitz-Gilbert (LLG) equation:

$$\frac{d\boldsymbol{M}}{dt} = \gamma\mu_0 \boldsymbol{M} \times \boldsymbol{H} + \frac{\alpha}{M_s}(\boldsymbol{M} \times \frac{d\boldsymbol{M}}{dt}) \tag{5.1}$$

Here, $\boldsymbol{M}$ is magnetization, $\boldsymbol{H}$ is magnetic field, μ_0 is the vacuum magnetic permeability, α is damping parameter and M_s is saturation magnetization. The first term on the right hand side describes the precession of the magnetization about the effective magnetic field; the precession frequency is proportional to the gyromagnetic ratio γ. The second term is the Gilbert damping term, which accounts for relaxation of the magnetization toward equilibrium. In general, $\boldsymbol{H}$ represents the effective magnetic field including the applied, anisotropy, and exchange contributions. For simplicity, and to isolate the influence of the applied bias field, we take $\boldsymbol{H}$ to include only the external field in this section. We decompose the magnetization and magnetic field into static and dynamic components,

$\boldsymbol{M} = \boldsymbol{M}_0 + \boldsymbol{m}$ and $\boldsymbol{H} = \boldsymbol{H}_0 + \boldsymbol{h}$ where the dynamic parts are small, $\boldsymbol{h} \ll \boldsymbol{H}_0$ and $\boldsymbol{m} \ll \boldsymbol{M}_0$. The time dependence of the dynamic components is assumed to be harmonic, $\boldsymbol{m}, \boldsymbol{h} \propto e^{i\omega t}$. For simplicity, we first neglect the damping term and consider a static bias field along the z axis, so that $\boldsymbol{H}_0 \parallel \hat{\boldsymbol{z}}$ and $\boldsymbol{M}_0 \parallel \hat{\boldsymbol{z}}$. Linearizing the LLG equation then yields

$$\begin{aligned} i\omega\boldsymbol{m} &= \gamma\mu_0 \left(H_0\,\boldsymbol{m} \times \hat{\boldsymbol{z}} + M_0\,\hat{\boldsymbol{z}} \times \boldsymbol{h}\right) \\ &= \left(\omega_0 \boldsymbol{m} - \omega_M \boldsymbol{h}\right) \times \hat{\boldsymbol{z}} \end{aligned} \tag{5.2}$$

where $\omega_0 = -\gamma\mu_0 H_0$ and $\omega_M = -\gamma\mu_0 M_s$. We use the convention $\gamma < 0$ for electron spins, so that $\omega_0 = -\gamma\mu_0 H_0 > 0$. Solving for the relation between $\boldsymbol{m}$ and $\boldsymbol{h}$ gives

$$\begin{bmatrix} \boldsymbol{h}_x \\ \\ \boldsymbol{h}_y \end{bmatrix} = \frac{1}{\omega_M} \begin{bmatrix} \omega_0 & i\omega \\ \\ -i\omega & \omega_0 \end{bmatrix} \begin{bmatrix} \boldsymbol{m}_x \\ \\ \boldsymbol{m}_y \end{bmatrix} = \overline{\chi}^{-1} \cdot \boldsymbol{m} \tag{5.3}$$

The tensor $\overline{\chi}$ is the Polder susceptibility, relating the dynamic magnetization to the dynamic magnetic field via $\boldsymbol{m} = \overline{\chi} \cdot \boldsymbol{h}$:

$$\overline{\chi} = \frac{\omega_M}{\omega_0^2 - \omega^2} \begin{bmatrix} \omega_0 & -i\omega \\ \\ i\omega & \omega_0 \end{bmatrix} \tag{5.4}$$

Spin waves are collective magnetization excitations accompanied by dipolar fields that satisfy Maxwell's equations. Assuming plane wave solutions of the form $\exp[i(\boldsymbol{k} \cdot \boldsymbol{r} - \omega t)]$, Maxwell's equations for small AC fields ($\boldsymbol{d}$ is electric displacement field, $\boldsymbol{b}$ is mag-

netic field, $\boldsymbol{e}$ is electric field) become

$$\nabla \cdot \boldsymbol{d} = i\boldsymbol{k} \cdot \boldsymbol{d} = 0 \tag{5.5}$$

$$\nabla \cdot \boldsymbol{b} = i\boldsymbol{k} \cdot \boldsymbol{b} = 0 \tag{5.6}$$

$$\nabla \times \boldsymbol{e} = i\boldsymbol{k} \times \boldsymbol{e} = i\omega\boldsymbol{b} = i\omega\mu_0(\boldsymbol{h}+\boldsymbol{m}) \tag{5.7}$$

$$\nabla \times \boldsymbol{h} = i\boldsymbol{k} \times \boldsymbol{h} = -i\omega\boldsymbol{d} = -i\omega\varepsilon\boldsymbol{e} \tag{5.8}$$

Using the vector identity $\boldsymbol{k} \times (\boldsymbol{k} \times \boldsymbol{e}) = \boldsymbol{k}(\boldsymbol{k} \cdot \boldsymbol{e}) - \boldsymbol{e}k^2$ and combining the above equations, we obtain

$$\begin{aligned}\boldsymbol{k} \times (\boldsymbol{k} \times \boldsymbol{e}) &= \omega\boldsymbol{k} \times \boldsymbol{b} = \omega\mu_0\boldsymbol{k} \times (\boldsymbol{h}+\boldsymbol{m}) \\ &= \omega\mu_0\,(-\omega\boldsymbol{d} + \boldsymbol{k} \times \boldsymbol{m}) = -\omega^2\mu_0\varepsilon\boldsymbol{e} + \omega\mu_0\boldsymbol{k} \times \boldsymbol{m}\end{aligned}$$

Therefore, the AC electric and magnetic fields are

$$\boldsymbol{e} = \frac{\omega\mu_0(\boldsymbol{k} \times \boldsymbol{m})}{k_0^2 - k^2} \tag{5.9}$$

$$\boldsymbol{h} = \frac{k_0^2\boldsymbol{m} - \boldsymbol{k}(\boldsymbol{k} \cdot \boldsymbol{m})}{k^2 - k_0^2} \tag{5.10}$$

where k_0 is the electromagnetic wavenumber. In the regime relevant to magnetostatic spin waves, the spin wave wavenumber satisfies $k \gg k_0$. In this limit, $\boldsymbol{e}$ becomes negligible because the denominator grows as k^2. In contrast, $\boldsymbol{h}$ remains finite since both its numerator

and denominator scale quadratically with $\boldsymbol{k}$. Then, Equation (5.5) - (5.8) become

$$\nabla \cdot \boldsymbol{e} = 0 \tag{5.11}$$

$$\nabla \cdot \boldsymbol{b} = 0 \tag{5.12}$$

$$\nabla \times \boldsymbol{e} = i\omega \boldsymbol{b} \tag{5.13}$$

$$\nabla \times \boldsymbol{h} = 0 \tag{5.14}$$

This is known as the magnetostatic approximation. Since $\nabla \times \boldsymbol{h} = 0$, we introduce a magnetic scalar potential ψ such that $\boldsymbol{h} = -\nabla\psi$. Using $\boldsymbol{b} = \mu_0(\boldsymbol{h} + \boldsymbol{m}) = \mu_0(\bar{I} + \bar{\chi}) \cdot \boldsymbol{h}$, the condition $\nabla \cdot \boldsymbol{b} = 0$ gives

$$\nabla \cdot \mu_0(\bar{I} + \bar{\chi}) \cdot \nabla\psi = 0 \tag{5.15}$$

Finally, the differential equation for the scalar potential becomes

$$\left(1 + \frac{\omega_M \omega_0}{\omega_0^2 - \omega^2}\right)\left(\frac{\partial^2\psi}{\partial x^2} + \frac{\partial^2\psi}{\partial y^2}\right) + \frac{\partial^2\psi}{\partial z^2} = 0 \tag{5.16}$$

This equation is known as Walker's equation and describes magnetostatic spin wave modes. Because $\boldsymbol{M_0}$ and $\boldsymbol{H_0}$ are aligned along $\hat{z}$, the Polder susceptibility in equation (5.4) has axial symmetry ($\chi_{xx} = \chi_{yy}, \chi_{xy} = -\chi_{yx}$). This symmetry allows Walker's equation to separate into components transverse to the bias direction (x, y) and parallel to it (z), leading to equation (5.16). Magnetostatic waves are classified by the relative orientations of the bias field $\boldsymbol{H}$ and the wavevector $\boldsymbol{k}$ as shown in Table 5.1. If $\boldsymbol{H}$ is normal to the film plane, the mode is a forward volume wave. If $\boldsymbol{H}$ lies in the film plane and $\boldsymbol{k} \parallel \boldsymbol{H}$, the mode is a backward volume wave [57]. If $\boldsymbol{H}$ lies in the film plane and $\boldsymbol{k} \perp \boldsymbol{H}$,

the mode is a magnetostatic surface spin wave (MSSW). In this dissertation, we focus

Forward volume wave	Backward volume wave	Surface wave
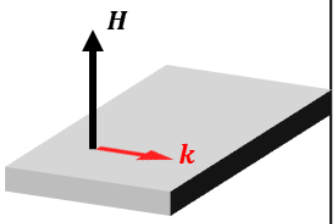	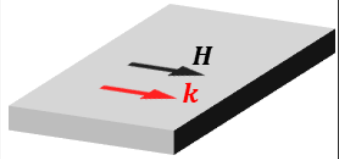	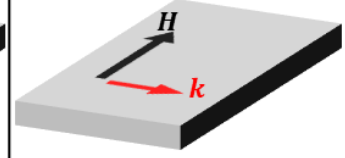
$\boldsymbol{H} \perp \boldsymbol{k}$ (perpendicular magnetized)	$\boldsymbol{H} \parallel \boldsymbol{k}$ (inplane magnetized)	$\boldsymbol{H} \perp \boldsymbol{k}$ (inplane magnetized)

Table 5.1: Spin wave types for different geometries of the magnetic field $\boldsymbol{H}$ and wavevector $\boldsymbol{k}$.

on MSSWs. Applying the boundary conditions at the surfaces of a magnetic thin film, Walker's equation yields the MSSW dispersion relation:

$$\omega_k(H,k) = -\gamma\mu_0 M_s \sqrt{\left[\frac{H}{M_s} + \alpha_{ex}k^2 + \frac{1}{kd}\left(1-e^{-kd}\right)\right]\left[\frac{H}{M_s} + \alpha_{ex}k^2 + 1 - \frac{1}{kd}\left(1-e^{-kd}\right)\right]} \tag{5.17}$$

Here d is the thickness of the magnetic film, and α_{ex} is the exchange interaction coefficient. The parameters α_{ex}, d, and M_s depend on the magnetic film properties. As the external field H changes, the dispersion relation shifts, leading to changes in the spin wave frequency and wavelength. Figure 5.1 shows the dispersion of MSSWs. The exchange interaction affects the dispersion only at short length scales; for spin waves with wavelengths above 1 μm, its contribution can be neglected. In this dissertation, we neglect exchange in the following analysis unless otherwise stated.

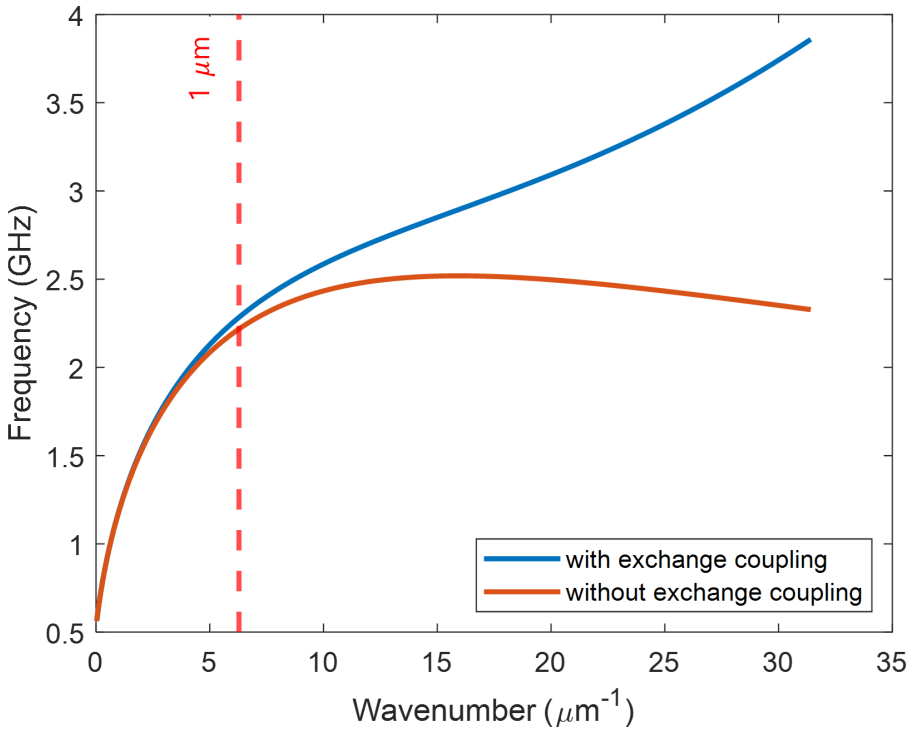

Figure 5.1: Calculated dispersion relation of magnetostatic surface spin waves. The external magnetic field of 20 G. Other parameters are $M_s = 140\ kA/m$, $\alpha_{ex} = 3 \times 10^{-16}\ m^2$, and $d = 100$ nm. Exchange interaction dominates at shorter wavelengths. For wavelengths longer than 1 μm, the exchange contribution is negligible.

5.2 Transport of spin waves

Before investigating the interaction between the NV center and spin waves, we first characterize spin wave generation and propagation via transmission measurements using a vector network analyzer (VNA). The range of wavevectors that can be efficiently excited and detected is set by the spatial current distribution of the antenna, which is dictated by the antenna geometry [58]. We therefore evaluated two antenna designs. Table 5.2 compares their layouts and corresponding excitation spectra. The left panel shows a simple stripline antenna with enlarged pads for electrical contact. In real space, the stripline current profile is well approximated by a rectangular function, yielding a sinc-shaped excitation spectrum in k-space. Consequently, this antenna predominantly excites spin waves with wavevectors k below the inverse stripline width; reducing the stripline width broadens the accessible wavevector range. The right panel shows a three line antenna, whose distributed signal and ground lines produce a nonuniform, multi-lobed current profile and a correspondingly structured k-space spectrum, enabling more selective excitation at finite wavevectors. In this dissertation, we employ the stripline design because it provides a broad spin wave spectrum suitable for the subsequent NV based measurements and spin wave reflector. The antennas were fabricated on the surface of a YIG thin film (Matesy GmbH, 1 cm $\times$ 1 cm $\times$ 100 nm). We first compared striplines of two different widths. In Figure 5.2 (a) and (c), both antennas show transmission peaks that shift to higher frequency with increasing magnetic field, corresponding to ferromagnetic resonance (FMR). Notably, the 2 μm stripline exhibits a broader transmission envelope than the 6 μm stripline. This difference becomes clearer when comparing spectra taken at the same magnetic field. Figure 5.2 (b) shows line cuts taken at the same magnetic field. The frequencies at which the transmission envelope narrows correspond to the wavevectors

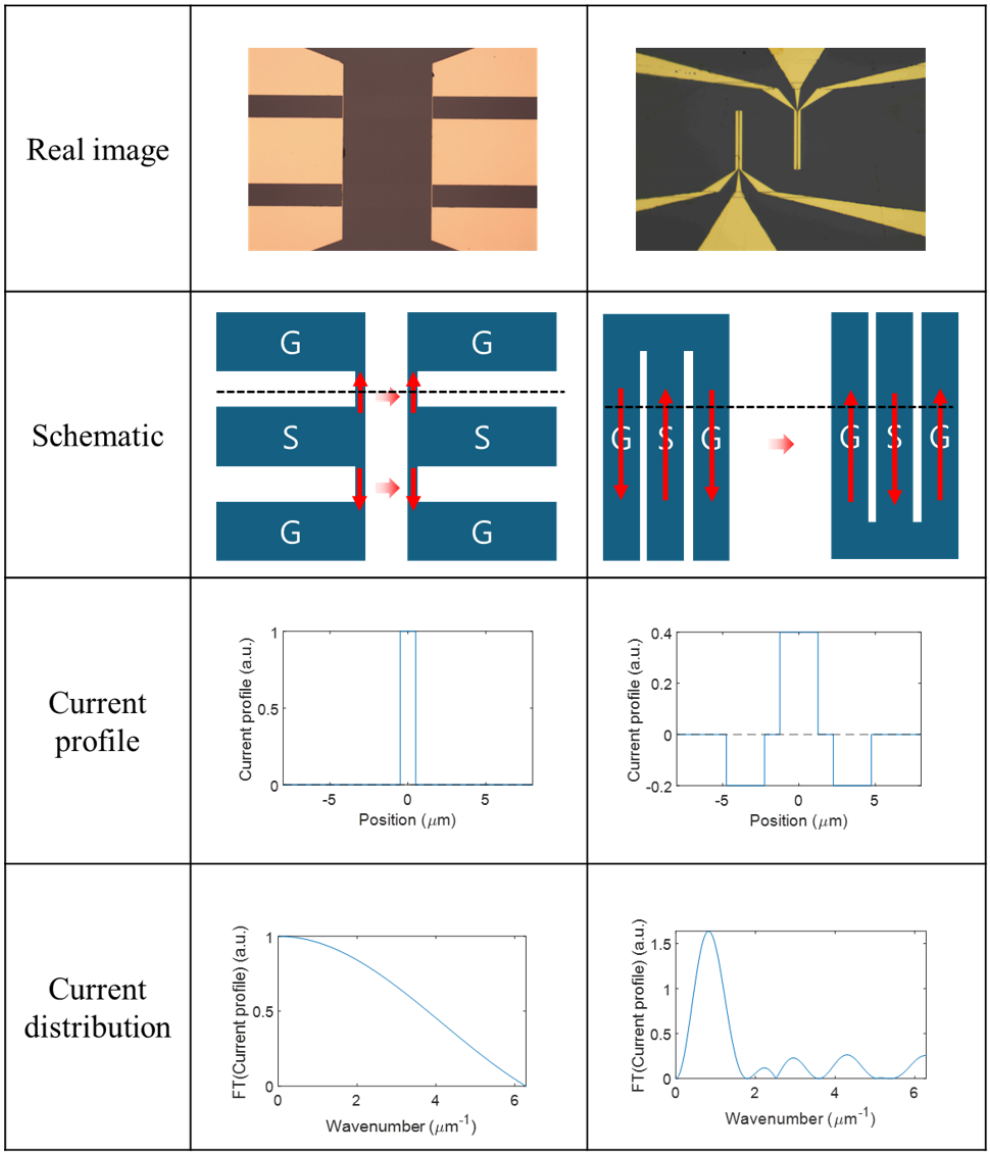

Table 5.2: Antenna structures. Real image: optical micrographs of the fabricated antennas. Schematic: layouts of the antenna geometries; the current (red arrows) flows from the signal (S) to the ground pads (G). Current profile: current density along the cutline indicated by the black dashed line in the schematics (left: conductor width 1 μm; right: signal/ground line widths 2.5 μm with a 1 μm gap). Current distribution: Fourier transforms of the current profiles. The stripline antenna exhibits a broad spectrum near $k = 0$, whereas the coplanar antenna enables excitation at a designed, finite wavenumber.

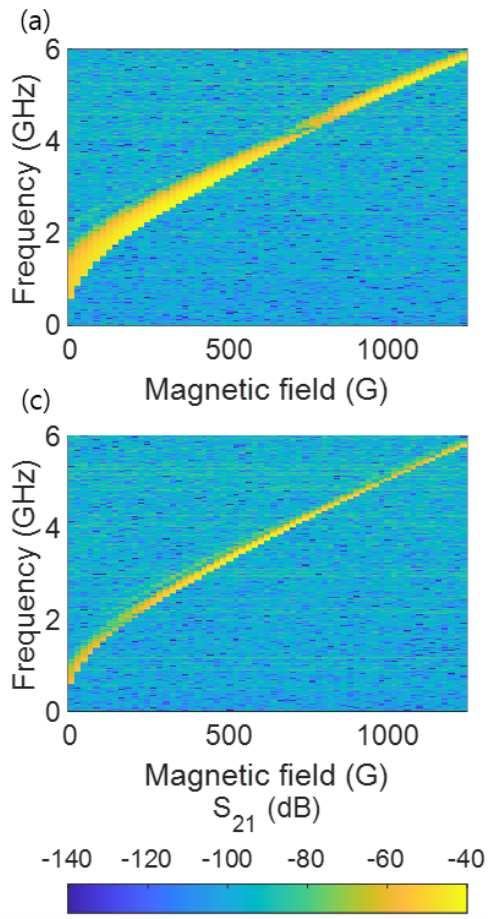

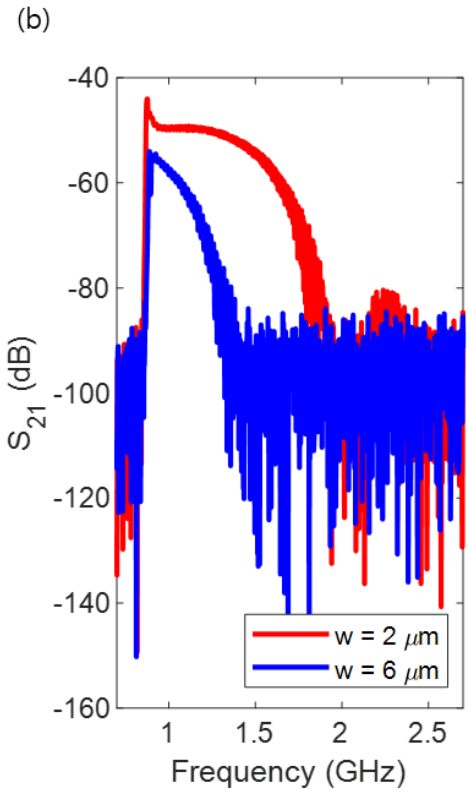

Figure 5.2: Spin wave transmission measured using (a) a 2 μm wide stripline and (c) a 6 μm wide stripline. The background measured at high magnetic field ($\mu_0 H = 1.2$ kG) has been subtracted. (b) Spin wave transmission at $\mu_0 H = 20$ G. The narrower stripline excites spin waves over a broader frequency range.

where the stripline width intersects the spin wave dispersion relation.

Figure 5.3 shows the spin wave transmission generated by a stripline with a width of 2 μm together with the corresponding dispersion relation. From the dispersion relation, it can be confirmed that the upper frequency limit of the broad spin wave spectrum corresponds to a wave vector of $k = 2\pi/(2\ \mu\text{m})$. In addition, in the frequency range above 2 GHz, a weaker transmission envelope is observed rather than a broad spectral response. This feature originates from the side lobes of the sinc-shaped k-space excitation spectrum associated with the stripline current distribution. From these observations, we confirm that spin waves are excited by the stripline antenna, propagate through the YIG film, and are detected by the same stripline geometry.

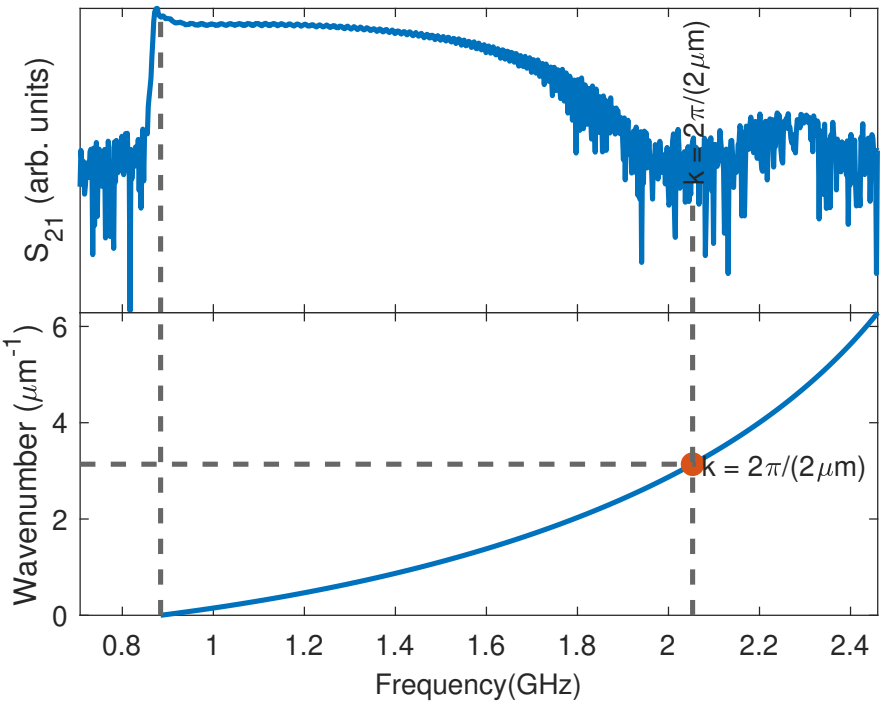

Figure 5.3: Spin wave transmission at $\mu_0 H = 20$ G. In lower panel, Dispersion relation of spin wave with magnetic field $\mu_0 H = 20$ G. Although the VNA measures the transmission as a function of frequency, the corresponding wavevector can be extracted by comparing the data with the spin wave dispersion relation. The left dashed line indicates FMR, the lowest frequency of spin wave resonance.

5.3 NV centers and spin waves

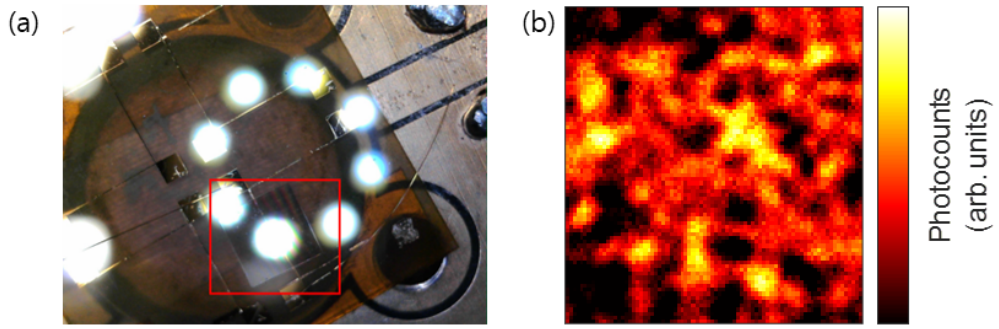

Figure 5.4: NV centers positioned in close proximity to the YIG film. (a) Photograph of the experimental assembly, where a diamond containing NV centers is placed on top of the YIG film. Microwave currents in the patterned striplines on the YIG film excite spin waves, and the stray magnetic fields generated by these spin waves interact with the NV centers. The red box indicates a diamond plate placed on top of the YIG. (b) Confocal fluorescence image of the NV centers obtained with the YIG film placed beneath the diamond.

In a qubit platform for information processing, entanglement among multiple qubits is essential. Entanglement between spatially separated NV centers mediated by photons has already been demonstrated [59, 60]. Entanglement between an NV center and a nearby nuclear spin has also been realized and applied to quantum information processing [61]. However, nuclear spin-NV interactions are practical only when the nuclei are located very close to the NV center.

To build a multi qubit quantum computer based on NV centers, a flying quantum excitation capable of interacting with spatially separated NV centers is therefore required. Magnons provide one possible solution [21, 62–64]. Spin waves can propagate with decay lengths of several micrometers or more, and thus NV centers separated by a few

micrometers could, in principle, be entangled via magnons [65, 66]. Achieving this goal requires a detailed understanding of NV-magnon interactions. Spin waves correspond to collective precession of magnetic moments and generate an oscillating stray magnetic field. NV centers couple to magnons through this stray field [67–71].

To enable NV-magnon interactions, the NV center must be positioned close to a magnetic film. This can be achieved in three main ways: (i) placing a diamond plate on the magnetic film with the NV layer facing the film [72], (ii) using a scanning probe with an NV center at its tip [73], or (iii) depositing a nanodiamond solution onto the film [74]. In this dissertation, we place a diamond plate directly on the surface of a YIG film.

We first drive microwaves through the stripline to perform CWESR measurements (Figure 5.5). By sweeping the magnetic field, we identify the ground state transitions $|0\rangle \leftrightarrow |-1\rangle$ and $|0\rangle \leftrightarrow |+1\rangle$. Small peaks appearing between these two main resonances originate from NV centers whose axes are not aligned with the applied magnetic field. At lower frequencies, additional broad features are observed, which we attribute to a mixture of NV excited state resonances and the FMR of the YIG film. Because these signals are close in frequency and strongly broadened, we do not analyze them further. To confirm that the observed signal originates from spin waves, we exploit a characteristic property of MSSWs. Figure 5.6 (c) shows mode profile of an MSSW. MSSWs are surface localized modes that propagate along the film surface, and their localization depends on the propagation direction. For example, a spin wave propagating to the right may be localized near the upper surface, whereas a wave propagating to the left is localized near the lower surface. Consequently, on a given side of the film, the stray magnetic field produced by an MSSW depends on its propagation direction. This nonreciprocal behavior is referred to as directionality. To quantify the spin wave intensity, we measure Rabi oscillations between $|-1\rangle$ and $|0\rangle$. Spin waves whose frequency matches the energy

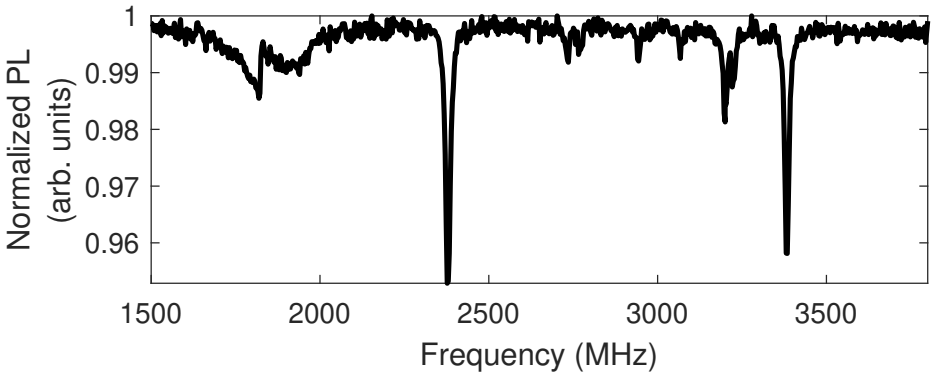

Figure 5.5: CWESR with YIG film. CWESR spectrum measured on the diamond on YIG sample at an external magnetic field of approximately 180 G. The two dips with the largest PL contrast correspond to the electron spin resonances of NV centers whose axes are aligned with the external magnetic field. The peaks with smaller PL contrast arise from electron spin resonances of NV centers that are misaligned with the external field, resulting in reduced contrast. Around 2000 MHz, the dips appear to originate from overlapping contributions of the NV center excited state resonance and the magnetic resonance, making them difficult to distinguish.

splitting between $|-1\rangle$ and $|0\rangle$ can drive population transitions, and a stronger stray field leads to a higher Rabi frequency. Figure 5.6 (a) was taken on the left side, about 50 μm away from the stripline, whereas Figure 5.6 (b) was taken on the right side at the same distance. The faster oscillations on (a) confirm the directional propagation of MSSWs.

To coherently couple NV centers to spin waves, both the spin wave dispersion and the NV transition frequencies must be considered. For a given magnetic field, only spin waves with wavevectors that satisfy the dispersion relation and simultaneously match an NV transition frequency can interact coherently with the NV center.

To identify the wavelength of the resonant spin waves, we measure Rabi oscillations at various positions along the propagation direction. Along the propagation direction, the spin wave can be approximated as a plane wave $\exp[i(kx-\omega t)]$. Although the phase of

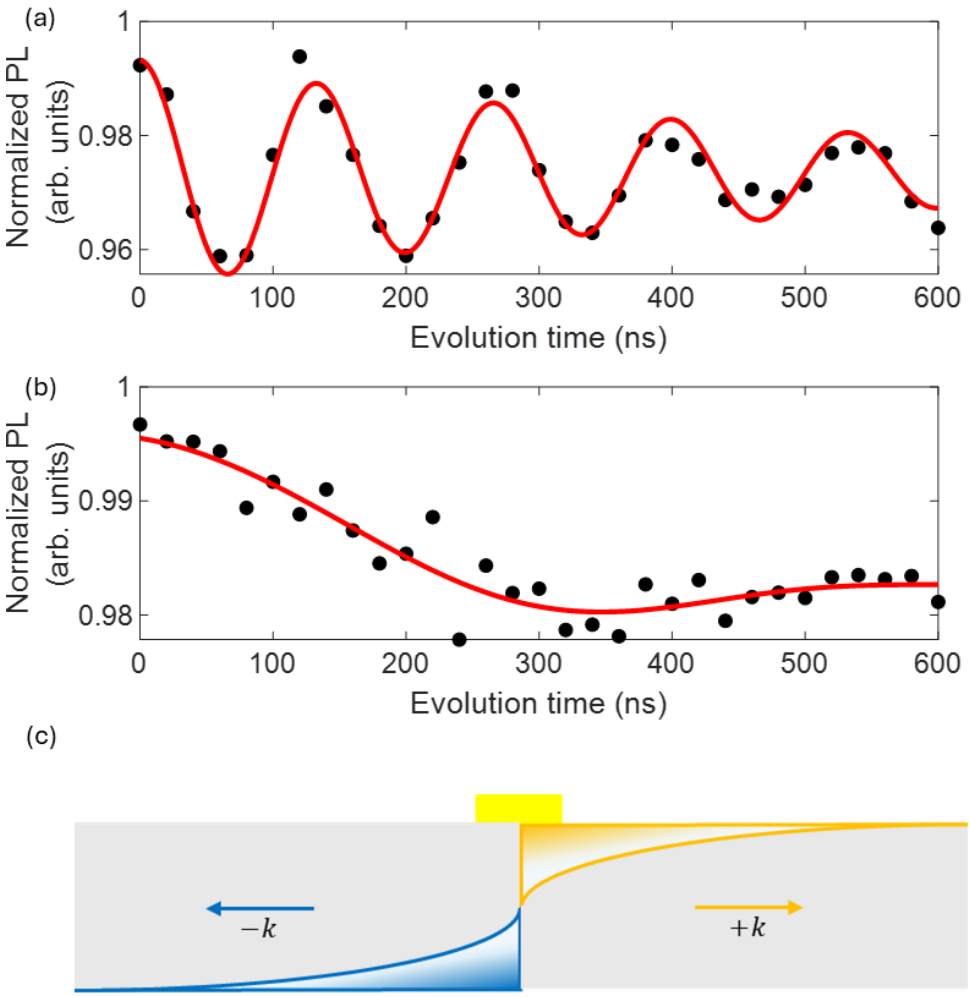

Figure 5.6: Rabi oscillations measured on opposite sides of the stripline. (a) Rabi oscillation acquired on the excited side. (b) Rabi oscillation acquired on the unexcited side. (c) Th schematic of an MSSW. an MSSW is a mode that propagates along the surface of a magnetic film, and its propagation direction determines which side of the film it travels on. When it propagates along the top versus the bottom surface, the magnitude of the stray field delivered to the NV centers becomes different.

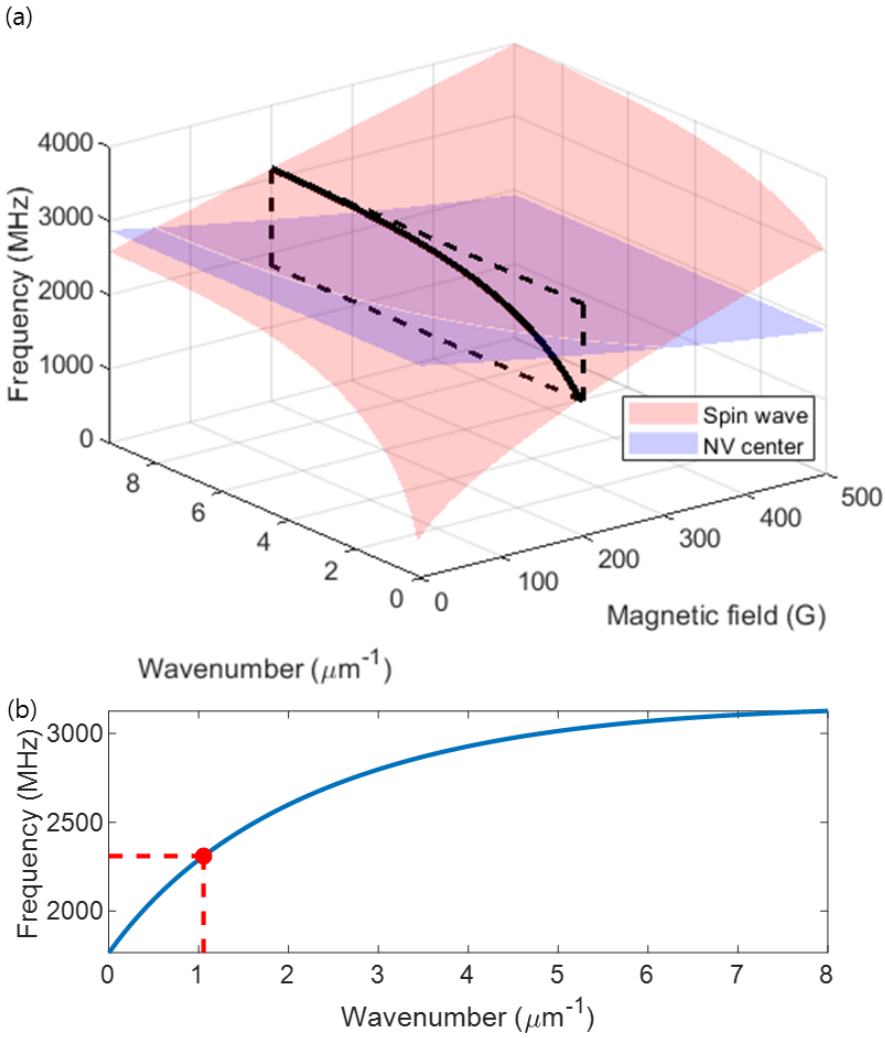

Figure 5.7: NV ground state levels and MSSW dispersion relation. (a) The external magnetic field modifies both the spin waves dispersion and the NV transition frequencies, thereby determining the resonance condition. (b) The dispersion of spin wave when magnetic field is 200 G. The magnetic field determines the electron spin resonance frequency of the NV centers, which in turn sets the wavelength of the spin waves that can interact coherently with them.

the spin wave cannot be obtained directly from its intensity, the stripline excites not only spin waves but also a propagating microwave background. The microwave background has a much longer wavelength than the spin wave, yet both generate oscillating magnetic fields at the same frequency. Their interference converts the spin wave phase into a measurable modulation of the AC magnetic field intensity. Figure 5.8 (a) shows the Rabi frequency as a function of distance from the stripline. The Rabi frequency, which reflects the local AC magnetic field amplitude, oscillates along the propagation direction. Figure 5.8 (b) shows the Fourier spectrum of the Rabi frequency data. From this analysis, we extract a spin wave wavelength of 17.4 μm, in good agreement with the value expected from the dispersion relation. To probe spin waves with shorter wavelengths, a more precise positioning system is required. We therefore use a scanning probe with an NV center attached at its apex. Figure 5.9 shows the scanning probe setup together with a YIG stripline antenna. This configuration allows the NV center to be positioned within a few micrometers of the stripline with high spatial precision. In addition, the NV and YIG separation can be actively controlled, which is not possible when simply placing a diamond plate on the film [75]. In this setup, interference is still present. We quantify the local field intensity using Rabi oscillations as well as the linewidth (or contrast) of the CWESR signal. Figure 5.10 shows three colormaps of the CWESR linewidth with different frequency. Figure 5.11 (a) shows an example map of the Rabi oscillation frequency. The observed wavelength patterns agree with those expected from the spin wave dispersion relation. As the magnetic field is varied, the dispersion relation changes, and consequently the wavelength resonant with the NV transition also changes. We imaged the spin-wave wavefront at four drive frequencies; the extracted wavelengths agree well with the theoretical dispersion (Figure 5.11 (b)).

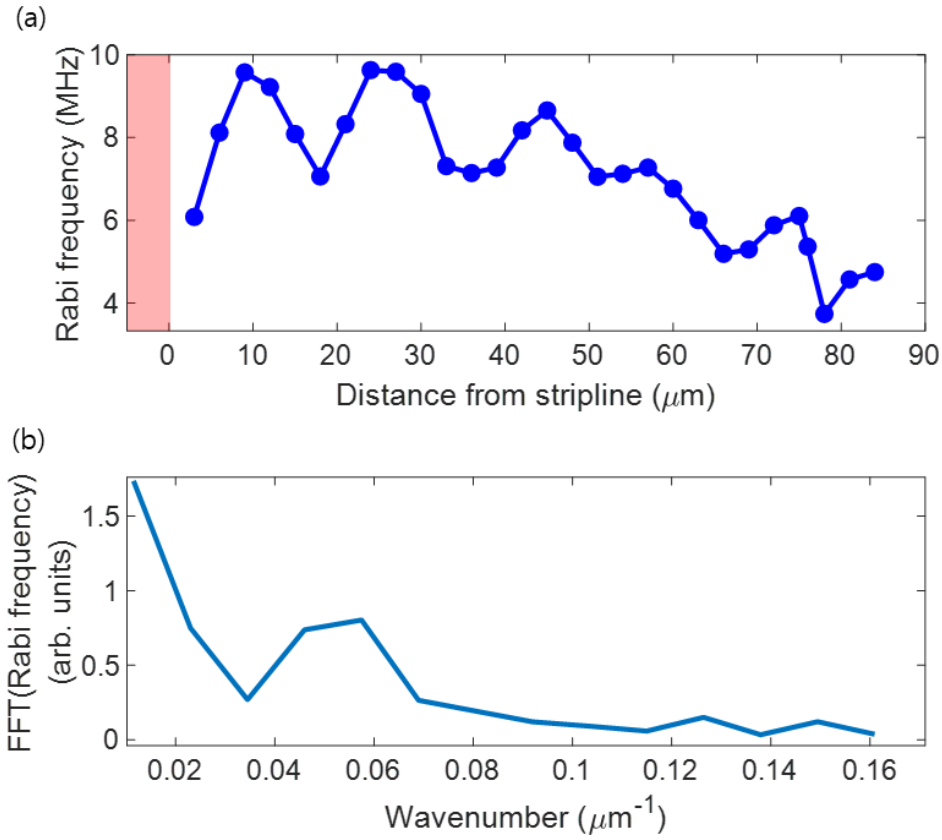

Figure 5.8: Spatial variation of Rabi frequency. (a) Rabi frequency versus distance from the stripline. Interference between the spin wave and the near field microwave background visualizes the wavefronts. The red shaded area represents stripline region. (b) The wavelength is extracted from the Fourier transform of the spatial Rabi frequency data.

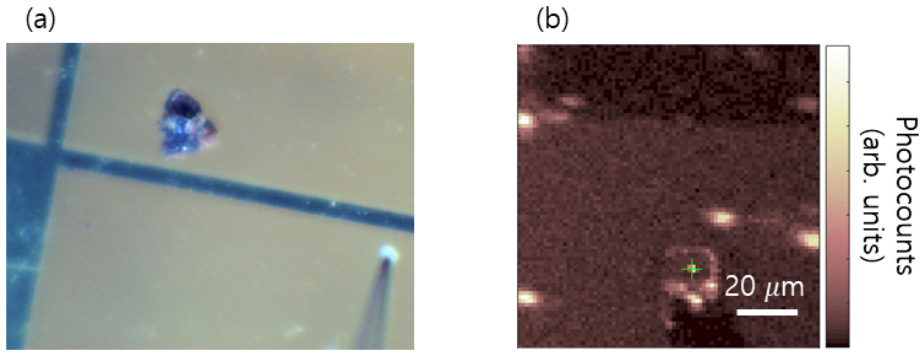

Figure 5.9: Scanning probe setup. (a) Optical microscope image of stripline and a probe with an NV center attached. (b) Confocal image.

5.4 Conclusions

In this chapter, we investigated the dispersion relation of MSSW and experimentally observed that the spin wave spectrum depends on the linewidth of the antenna used to generate the waves. We also showed that spin wave characteristics such as propagation direction and wavelength can be extracted using NV centers. This NV-spin wave hybrid platform therefore provides a foundation not only for employing NV centers as imaging sensors, but also for using spin waves as a medium to transmit information encoded in NV centers. For future applications where spin waves serve as information carriers, it is necessary to go beyond the regime in which externally injected spin waves simply perturb the NV centers, instead, coherent interactions between NV centers and spin waves confined within a structure are required. To this end, we propose creating spin wave reflectors to trap spin waves in a defined region. In the next chapter, we present simulations for designing such spin wave reflectors, along with examples of fabricated devices.

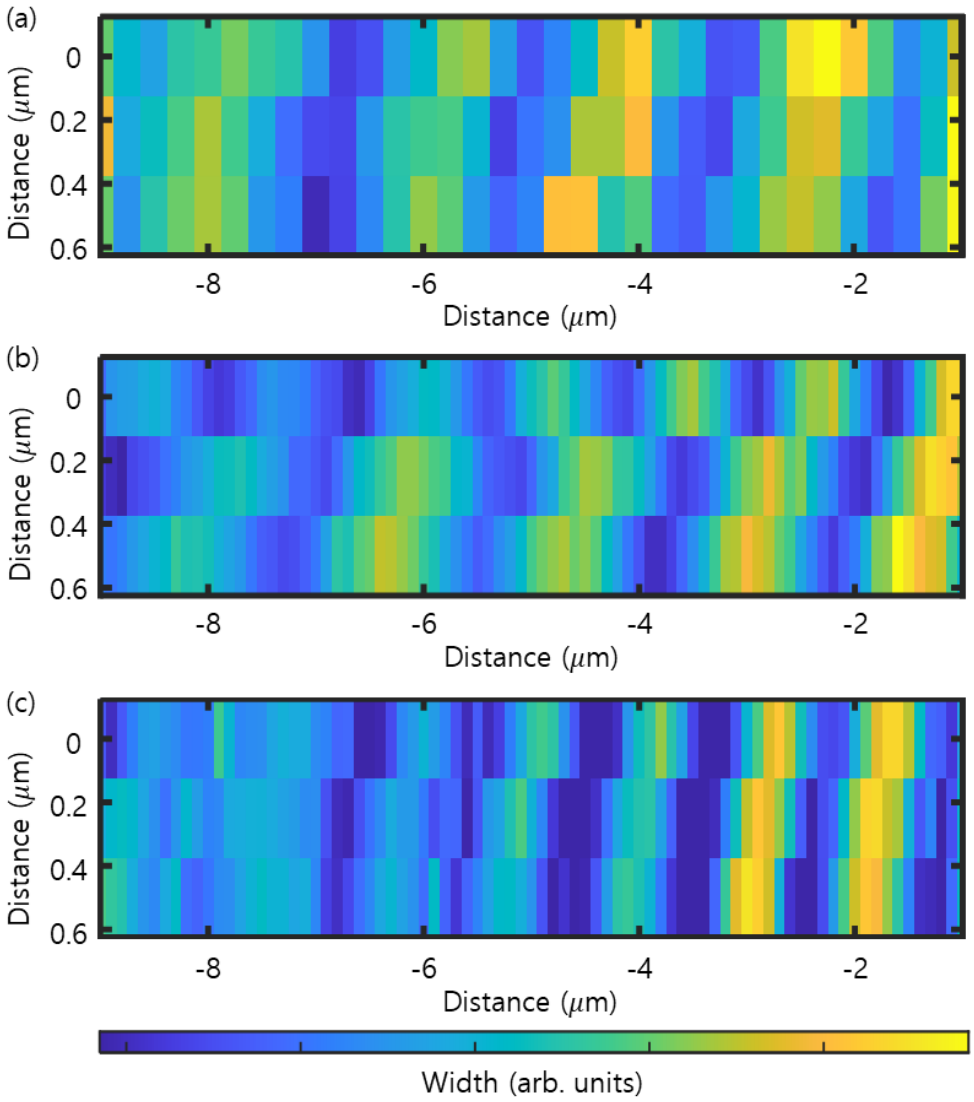

Figure 5.10: Scanning NV magnetometry images. These images are acquired from the CWESR linewidth. The frequency of the CWESR was controlled by the external magnetic field. The CWESR frequencies for each case are (a) 2556 MHz, (b) 2601 MHz, and (c) 2650 MHz.

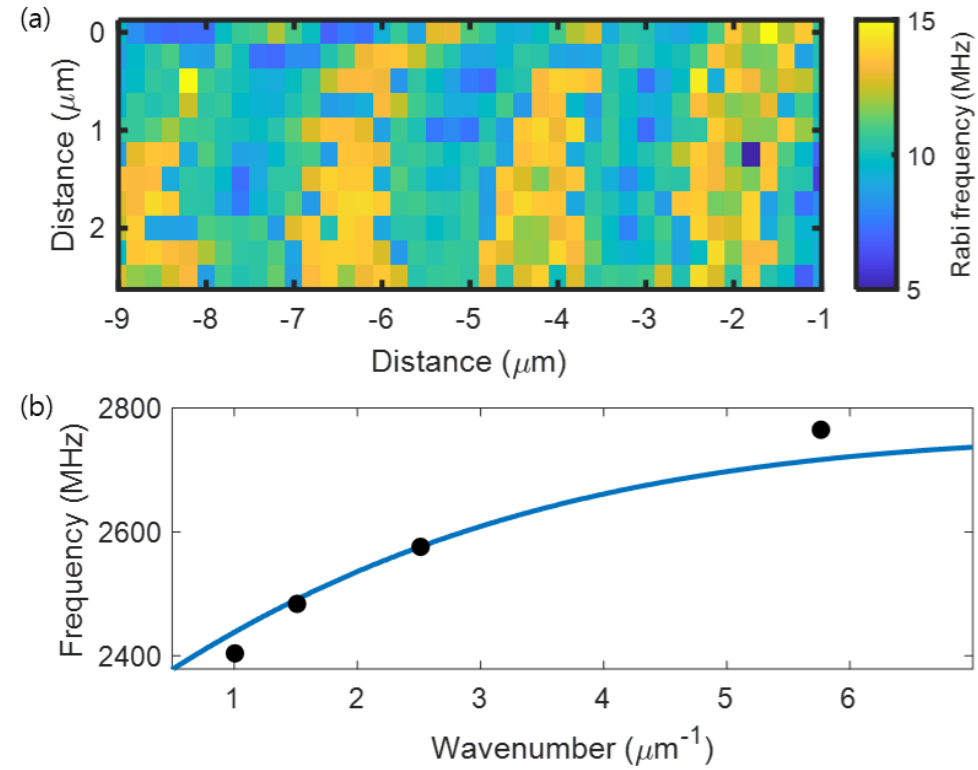

Figure 5.11: Spin wave wavelengths extracted from scanning NV magnetometry. The data agree well with wavelengths calculated from the MSSW dispersion relation.

Chapter 6. Distributed Bragg Reflector

To realize information processing via magnons, strong coupling between a qubit and a magnon is essential. One way to enhance the coupling is to confine the magnon mode to a small volume, which increases the field amplitude at the qubit location. In optics, the periodic modulation of refractive index produces a stop band via Bragg interference, which is called distributed Bragg reflector (DBR). In magnonic DBRs, an analogous stop band arises from a periodic modulation of the spin wave dispersion via thickness or material contrast, leading to strong reflection at Bragg wavevectors. A spin wave DBR cavity can produce a spatially localized spin wave mode; if a qubit is placed inside such a cavity, a much larger coupling strength can be expected. In this chapter, we first review optical DBR cavities and their basic structure. We then simulate a spin wave DBR reflector with an analogous geometry. Finally, we introduce spin wave reflectors based on an array of nickel stripe patterns forming a periodic structure.

6.1 Basics of DBR Cavities in Photonics

Before studying spin wave DBRs, it is useful to review optical DBRs, whose behavior can be treated more straightforwardly. An optical DBR consists of alternating layers of two materials with different refractive indices [76]. A standard approach for calculat-

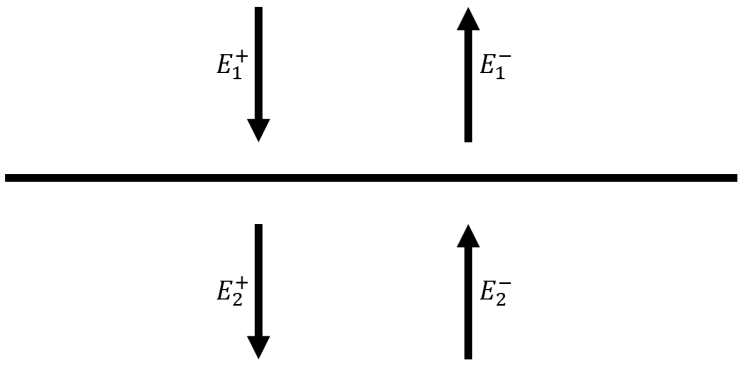

Figure 6.1: Electric fields at the interface. The reflection and transmission of optical waves propagating in two media with different propagation directions at an interface are calculated.

ing the response of a DBR is the transfer matrix method (TMM). At each interface, an optical wave is partially reflected and partially transmitted; in the TMM formalism, these processes are represented by matrices that relate the forward and backward propagating field amplitudes across the boundary. Figure 6.1 illustrates the optical fields at an interface, where two counter propagating waves exist on each side. The fields on the two sides of the interface are related by

$$\begin{bmatrix} E_2^+ \\ E_2^- \end{bmatrix} = \begin{bmatrix} M_{11} & M_{12} \\ M_{21} & M_{22} \end{bmatrix} \begin{bmatrix} E_1^+ \\ E_1^- \end{bmatrix} \tag{6.1}$$

where E_i^+ (E_i^-) denotes the forward (backward) propagating field in region i. The reflection coefficient for incidence from region 1 to region 2 is obtained by imposing the outgoing wave boundary condition $E_2^- = 0$:

$$r_{12} = \left.\frac{E_1^-}{E_1^+}\right|_{E_2^-=0} = -\frac{M_{21}}{M_{22}} \tag{6.2}$$

Similarly, the transmission coefficient is

$$t_{12} = \left.\frac{E_2^+}{E_1^+}\right|_{E_2^-=0} = M_{11} - \frac{M_{21}M_{12}}{M_{22}} \tag{6.3}$$

As an example, for normal incidence at an interface between two media with refractive indices n_1 and n_2, the interface matrix is

$$M_I(n_1,n_2) = \frac{1}{2}\begin{bmatrix} 1+\frac{n_1}{n_2} & 1-\frac{n_1}{n_2} \\ 1-\frac{n_1}{n_2} & 1+\frac{n_1}{n_2} \end{bmatrix} \tag{6.4}$$

Propagation through a layer of refractive index n and thickness t is described by

$$M_P(n) = \begin{bmatrix} \exp\left(2\pi i\frac{nt}{\lambda}\right) & 0 \\ 0 & \exp\left(-2\pi i\frac{nt}{\lambda}\right) \end{bmatrix} \tag{6.5}$$

where λ is the vacuum wavelength. A DBR is formed by repeating two layers with refractive indices n_a and n_b, as shown in Figure 6.2. The total transfer matrix of the DBR

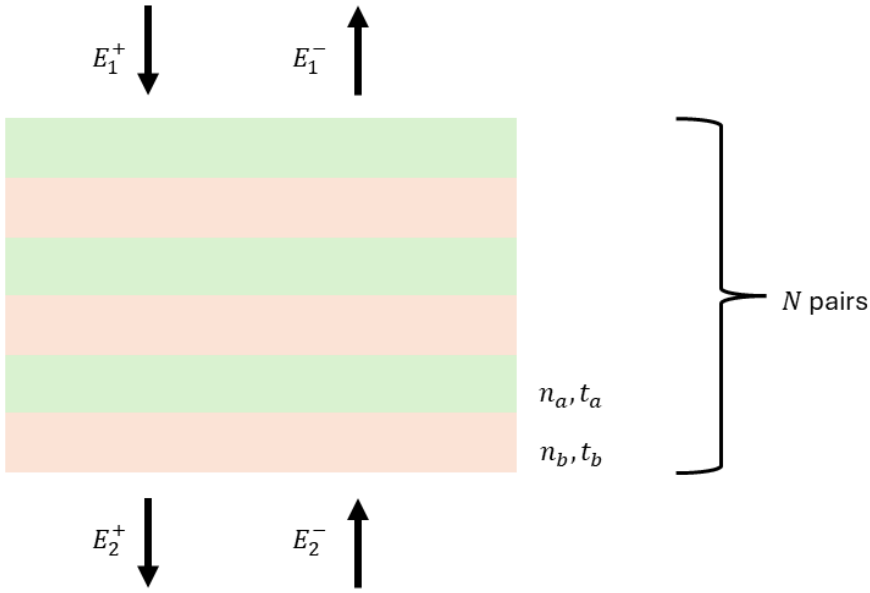

Figure 6.2: Schematic of a DBR composed of alternating layers with refractive indices n_a and n_b.

is the ordered product of the interface and propagation matrices for all layers:

$$\begin{bmatrix} E_2^+ \\ E_2^- \end{bmatrix} = M_{\text{DBR}} \begin{bmatrix} E_1^+ \\ E_1^- \end{bmatrix}$$

$$= M_I(n_b,1)\,M_P(n_b)\,M_I(n_a,n_b)\,M_P(n_a)\cdots M_P(n_a)\,M_I(1,n_a) \begin{bmatrix} E_1^+ \\ E_1^- \end{bmatrix} \tag{6.6}$$

From M_{DBR}, the reflectance $R = |r|^2$ and transmittance $T = |t|^2$ can be obtained. Figure 6.3 (a) shows representative results for $n_a = 1.4$, $n_b = 1.1$, $t_a = 80$ nm, $t_b = 100$ nm and

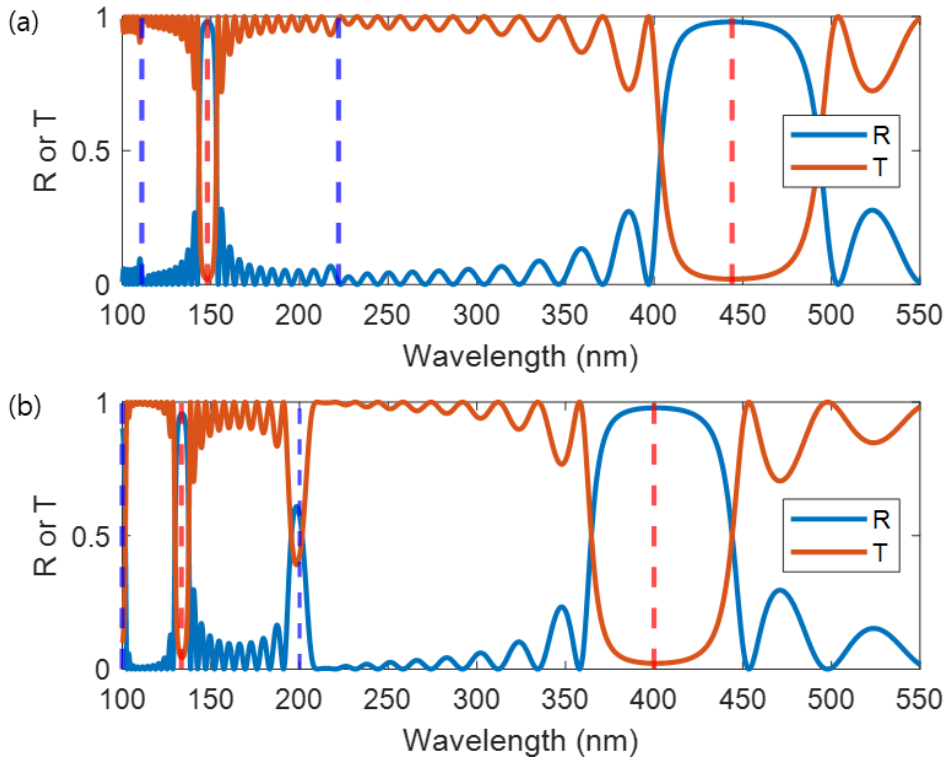

Figure 6.3: Reflectance R and transmittance T of a single DBR. For (a), $n_a = 1.4$, $n_b = 1.1$, $t_a = 80$ nm, $t_b = 100$ nm and $N = 10$. For (a), $n_a = 1.4$, $n_b = 1.1$, $t_a = 80$ nm, $t_b = 80$ nm and $N = 10$. The vertical dashed lines indicate wavelength $\lambda = \frac{2(n_a t_a + n_b t_b)}{n}$ (red: odd n, blue: even n).

$N = 10$ periods. The periodic structure produces a pronounced stop band in which R is strongly enhanced and T is suppressed. The vertical dashed line indicates the wavelength satisfying $\frac{2\pi}{\lambda}(n_a t_a + n_b t_b) = n\pi$. Under this Bragg condition, reflections from successive periods interfere constructively, driving $R \to 1$ and $T \to 0$. More generally, reflective bands occur whenever

$$\frac{2\pi}{\lambda}(n_a t_a + n_b t_b) = n\pi \tag{6.7}$$

with integer order n. Mathematically, Bragg reflection should occur at all wavelengths that satisfy the above condition. However, in Figure 6.3 (a), the reflectance increases for odd n (red dashed lines), whereas no such enhancement is observed for even n (blue dashed lines). In contrast, Figure 6.3 (b) shows an increase in reflectance regardless of whether n is odd or even. The only difference between the two cases is t_b. In (a), the phase accumulated in regions a and b are similar $\left(\frac{n_a t_a}{n_b t_b} \approx 1\right)$, while in (b) the phases acquired in the two regions are different. These results indicate that Bragg reflection is robust for odd n independent of the specific parameters, but for even n the parameters that define the Bragg structure strongly affect the reflectance and transmittance. A similar behavior will also be observed in the simulations of the spin wave reflector in the next section. Therefore, to use the DBR structure effectively, we will focus on the fundamental mode with $n = 1$. Our goal is to localize the wave in space. To this end, as shown in Figure 6.4, two DBRs are placed facing each other and separated by a distance d, forming a cavity. We again use the TMM to analyze the resulting spectral response. The DBRs

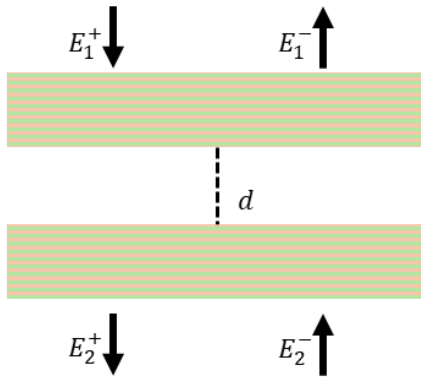

Figure 6.4: Optical cavity formed by two opposing DBRs separated by distance d. The optical fields will be confined in the space between the two reflectors, forming an optical cavity.

act as mirrors, confining the field within the cavity. The wave undergoes repeated round trips; for certain wavelengths, the accumulated round trip phase leads to constructive interference, producing resonant modes. The resonance condition is

$$\phi_{\mathrm{RT}} = 2\pi \frac{2d_{\mathrm{eff}}}{\lambda} = 2\pi m \quad (m = 1, 2, 3, \ldots) \tag{6.8}$$

where d_{eff} is the effective cavity length. Because the field penetrates into each DBR over a finite depth, d_{eff} is slightly larger than the physical separation d. Figure 6.5 shows the reflectance and transmittance of the DBR cavity for $d = 6\ \mu$m, with all other parameters identical to those used for the single DBR. Within the DBR stop band, several narrow transmission peaks appear, corresponding to cavity resonances. The spacing between adjacent resonances is the free spectral range (FSR), which follows directly from the cavity condition:

$$\phi_{\mathrm{RT}} = 2\pi \frac{d_{\mathrm{eff}}}{\lambda} = 2\pi \frac{d_{\mathrm{eff}} f}{c} = 2m\pi \tag{6.9}$$

Thus,

$$\Delta\lambda = \frac{\lambda^2}{2d_{\mathrm{eff}}} \tag{6.10}$$

$$\Delta f = \frac{c}{2d_{\mathrm{eff}}} \tag{6.11}$$

Equation (6.10) and (6.11) define the FSR in wavelength and frequency units, respectively. Because $\Delta\lambda$ depends on λ, it is often more convenient to use the constant frequency domain FSR. From Figure 6.5, the measured FSR is 21.6 THz, corresponding to an effective cavity length of $d_{\mathrm{eff}} = 6.9\ \mu$m, consistent with the resonance condition.

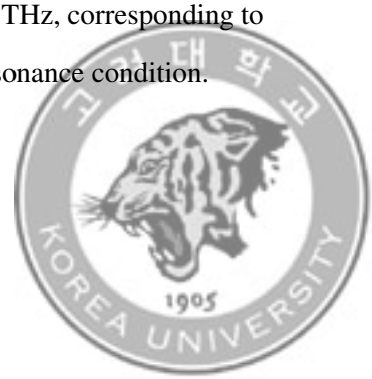

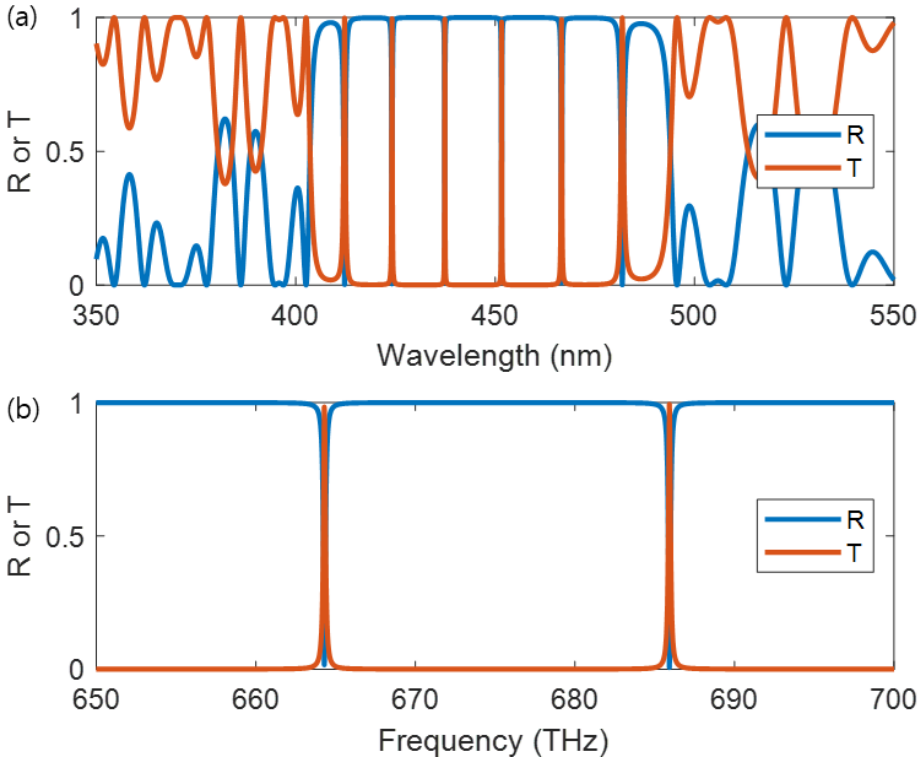

Figure 6.5: Reflectance and transmittance of a DBR cavity. The parameters used to construct the DBR are the same as those in Figure 6.3 (a). The separation between the two DBRs is $d = 6\ \mu$m. (a) Reflectance and transmittance calculated as a function of wavelength. (b) Reflectance and transmittance calculated as a function of frequency.

6.2 Spin wave simulation

Optical waves are governed by Maxwell's equations, and therefore their wave properties including reflectance, transmittance, and dispersion can often be obtained analytically. In contrast, for spin waves, analytical treatments exist in simplified geometries, but complex patterned structures are most reliably captured by micromagnetic simulations [77,78]. To study spin wave DBRs, we therefore employ MuMax3, a micromagnetic simulation package [79]. To obtain the spin wave dispersion in a YIG film, we simulate

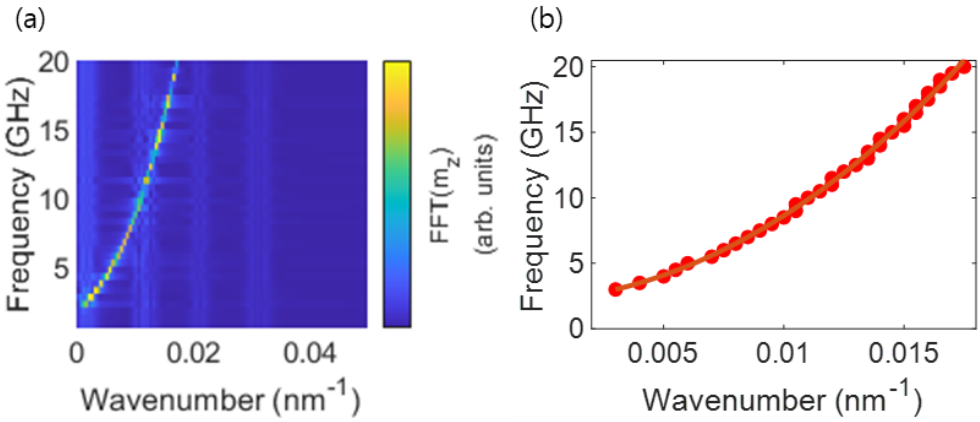

Figure 6.6: The spin wave spectrum. (a) Spin wave frequency versus wavenumber. (b) Dispersion relation extracted from (a).

spin waves driven over a range of frequencies. Figure 6.6 shows the resulting dispersion relation, which we fit using

$$f = \sqrt{\left[f_0 + \alpha_{ex} f_m k^2 + \frac{f_m}{kd}\left(1 - e^{-kd}\right)\right]\left[f_0 + \alpha_{ex} f_m k^2 + \frac{f_m}{kd}\left(kd - 1 + e^{-kd}\right)\right]} \quad (6.12)$$

In our simulation, k ranges from 0 to 0.02 nm^{-1} and the film thickness is $d = 10$ nm, so that $kd \ll 1$. In this limit, the dispersion simplifies to

$$f = \sqrt{[f_0 + f_m + \alpha_{ex} f_m k^2]\,[f_0 + \alpha_{ex} f_m k^2]} \tag{6.13}$$

From the fit, we obtain $f_0 = 0.649$ GHz, $f_m = 6.05$ GHz, and $\alpha_{ex} = 9.19 \times 10^3$ nm^2.

A spin wave DBR can be realized by introducing periodic modulation to parameters that affect the spin wave dispersion, analogous to how an optical DBR is formed by modulating the refractive index [80–87] Our simulated DBR structure has a period of 100 nm, consisting of alternating segments of 100 nm and 50 nm thickness, as illustrated in Figure 6.7. The periodic thickness modulation directly changes the local MSSW dispersion providing the required contrast for Bragg reflection. Analogous to optical DBRs, spin wave DBRs satisfy a Bragg condition, $2a = n\lambda_n$ (or equivalently $2ka = 2\pi n$), where a is the period and λ_n is the wavelength of the nth order Bragg reflection. Figure 6.8 compares the spectra with and without the DBR. Clear dips appear near $k = 0.005$ nm^{-1} and $k = 0.015$ nm^{-1}, corresponding to the $n = 1$ and $n = 3$ Bragg conditions, respectively. These dips correspond to Bragg stop bands (magnonic bandgaps) where counter propagating waves interfere constructively, suppressing transmission. As shown in Figure 6.8 (b), Bragg reflection occurs only at wavenumbers corresponding to odd n. This behavior is consistent with the result observed for the optical DBR in the previous chapter. We attribute the absence of even order Bragg reflection to the fact that the thickness modulation forming the Bragg structure is even symmetric, which suppresses Bragg scattering at even order wavenumbers. To visualize the DBR effect, we plot a colormap of the spin wave amplitude as a function of position and time. The vertical axis denotes the distance from the excitation region, while the horizontal axis represents simulation time. The gray

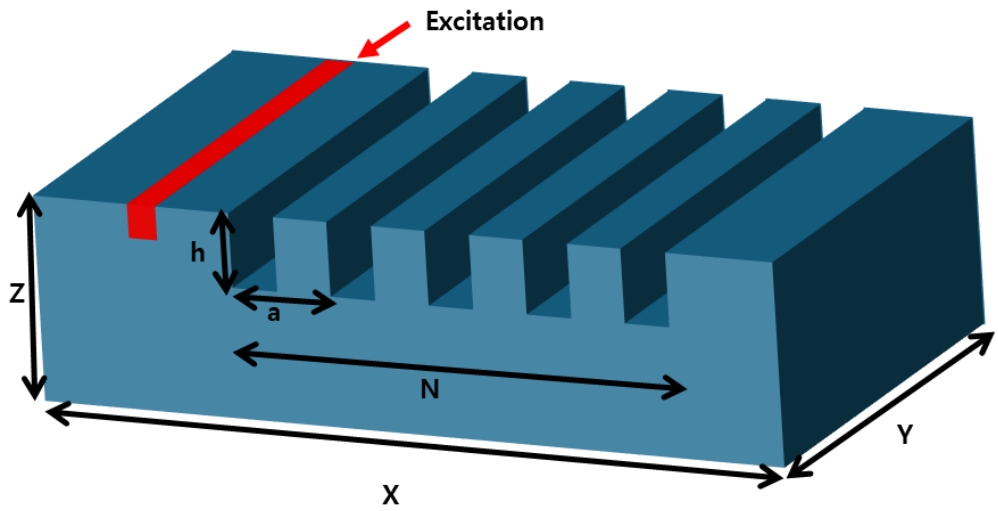

Figure 6.7: Schematic of the spin wave DBR model used in the MuMax3 simulations. The overall simulation domain was defined with dimensions of X = 8000 nm, Y = 500 nm, and Z = 10 nm. The DBR structure was implemented as a periodically repeated groove pattern with thickness modulation, where the groove depth and period were set to h = 5 nm and a = 100 nm, respectively. Each groove had a width of 50 nm and a depth of 5 nm, and the number of repetitions was set to N = 5. Spin waves were excited in the excitation region and propagated along the ±X direction. The DBR characteristics were evaluated by analyzing the spin waves transmitted after passing through the DBR structure.

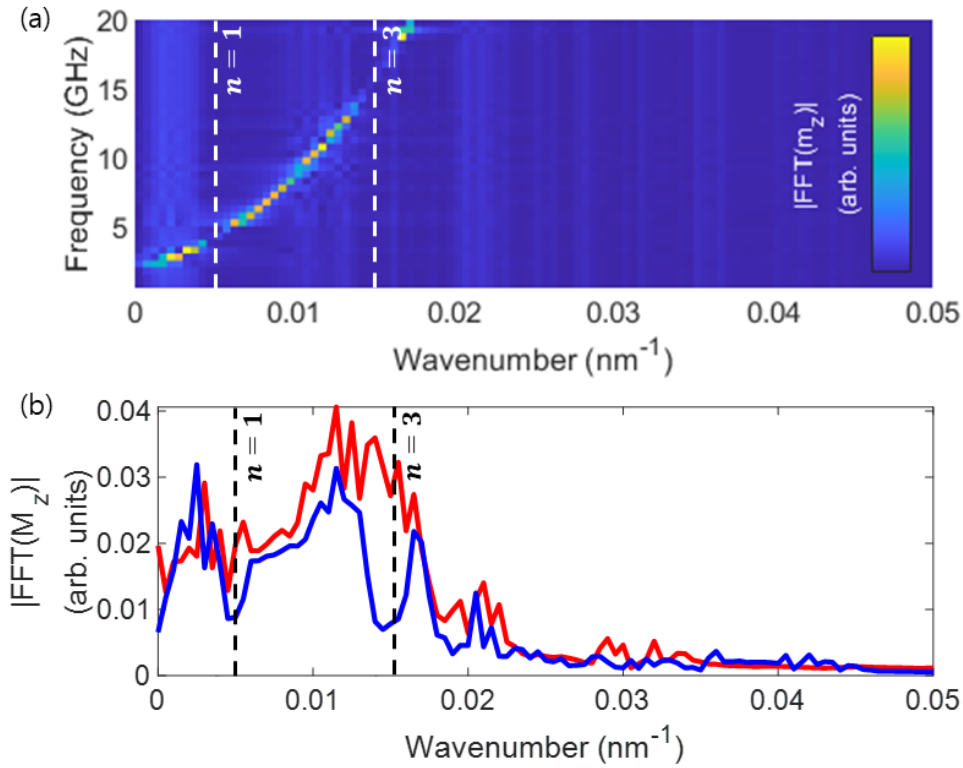

Figure 6.8: Spin wave DBR performance. (a) Spin wave spectrum after propagation through the DBR. (b) Wavenumber resolved spectral intensity obtained by integrating the spectra over frequency, $|\mathrm{FFT}(m_z)|$ is summed along the frequency axis to yield the total intensity as a function of wavenumber only. The red line corresponds to the case without a DBR (Figure 6.6(a)), while the blue line represents the spectrum after passing through the DBR (Figure 6.8(a)). Dashed lines represent wavenumber satisfying DBR condition.

region indicates the DBR segment. Figure 6.9 shows two representative cases. Figure 6.9 (a) corresponds to a frequency of 4.5 GHz ($k = 0.005\ \mathrm{nm}^{-1}$), where the Bragg condition is satisfied; the spin wave is strongly reflected and cannot propagate through the DBR. Figure 6.9 (b) corresponds to 6.5 GHz, which does not satisfy the Bragg condition, and the spin wave propagates through the DBR with minimal reflection.

As in the preceding optical analysis, we construct a DBR cavity by placing two DBRs at a fixed separation. The DBR is identical to that used previously, except that the number of periods is reduced to $N = 3$. Figure 6.10 (a) shows the transmission spectrum near the first stop band of this DBR. Around $f \approx 4$ GHz, spin wave transmission is strongly suppressed, indicating that waves in this frequency range are predominantly reflected by the DBR.

When a second DBR is added to form a cavity, cavity resonances are expected to appear as narrow transmission peaks inside the stop band. To estimate the resonance condition, we follow the standard cavity argument, as in an optical cavity. The round trip phase condition is given by

$$\phi_{\mathrm{RT}} = 2kd = 2\pi n, \tag{6.14}$$

where k is the spin wave wavenumber, d is the cavity length, and n is an integer. The spacing between adjacent resonant wavenumbers is therefore

$$\Delta k = \frac{\pi}{d}. \tag{6.15}$$

Converting this wavenumber spacing into the frequency domain yields the FSR,

$$\Delta f = \left.\frac{\partial f}{\partial k}\right|_{k_0} \Delta k, \tag{6.16}$$

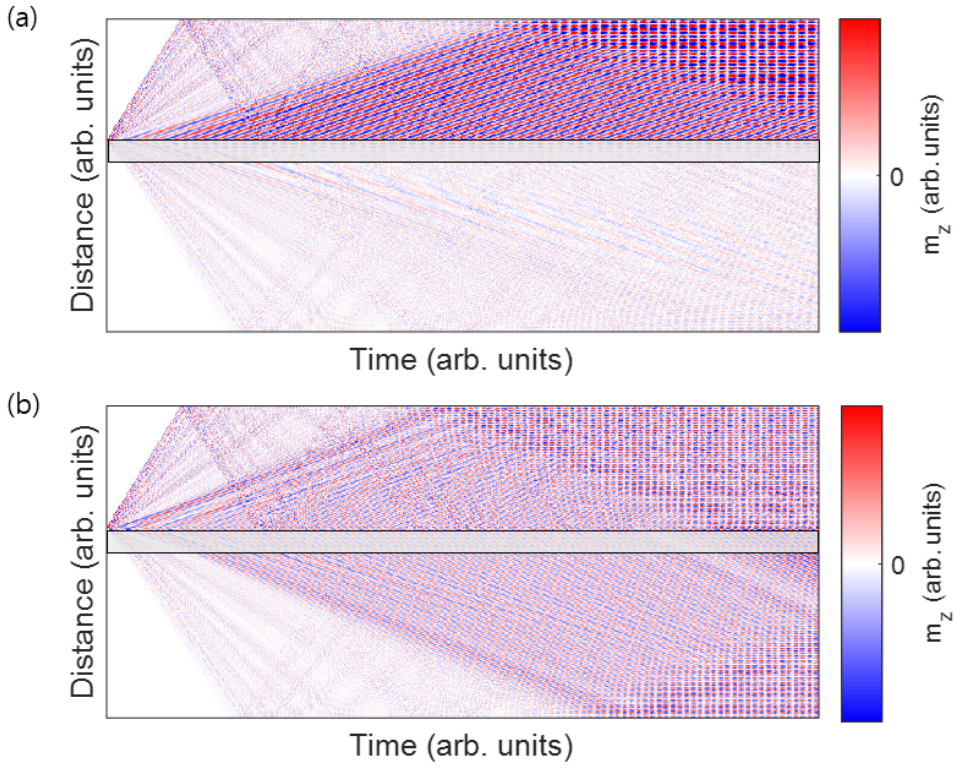

Figure 6.9: Comparison of pass band and stop band behavior in a spin wave DBR. The gray region marks the DBR. (a) At 4.5 GHz, the Bragg condition is satisfied and the wave is strongly reflected. (b) At 6.5 GHz, the Bragg condition is not satisfied and the wave propagates through the DBR.

where $\partial f/\partial k$ is evaluated at a representative wavenumber k_0 near the first stop band. Since spin waves generally exhibit a nonlinear dispersion relation, we approximate the local dispersion slope near $f \approx 4$ GHz as

$$\left.\frac{\partial f}{\partial k}\right|_{k_0} \approx \frac{2\ \text{GHz}}{0.003\ \text{nm}^{-1}}. \tag{6.17}$$

Using a cavity length of $d = 2500$ nm, the resulting FSR is

$$\Delta f = \left(\frac{2\ \text{GHz}}{0.003\ \text{nm}^{-1}}\right)\left(\frac{\pi}{2500\ \text{nm}}\right) \approx 0.13\ \text{GHz}. \tag{6.18}$$

As shown in Figure 6.10 (b), this estimated FSR is in good agreement with the spacing between the transmission peaks.

To visualize the spin wave dynamics, we examine the time evolution of the magnetization. The transmitted and reflected cases are clearly distinguishable. In Figrue 6.11 (a), multiple reflections inside the DBR cavity lead to constructive interference, resulting in the formation of a standing wave pattern within the cavity. In contrast, Figure 6.11 (b) shows a non-resonant case in which the resonance condition is not satisfied; as a result, constructive interference does not build up and the spin wave amplitude inside the cavity rapidly decays.

These results demonstrate that a spin wave DBR, analogous to an optical DBR, enables frequency selective transmission. Furthermore, by forming a DBR cavity, spin waves can be confined within the cavity region. In contrast to the transmission spectra of optical DBR cavities calculated using the TMM, the simulated spin wave DBR cavity exhibits transmission peaks with a finite linewidth. This linewidth broadening originates from intrinsic spin wave damping in the magnetic medium. Consequently, achieving a

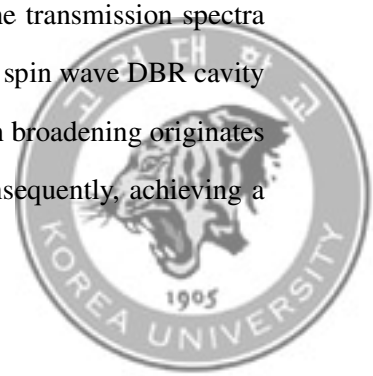

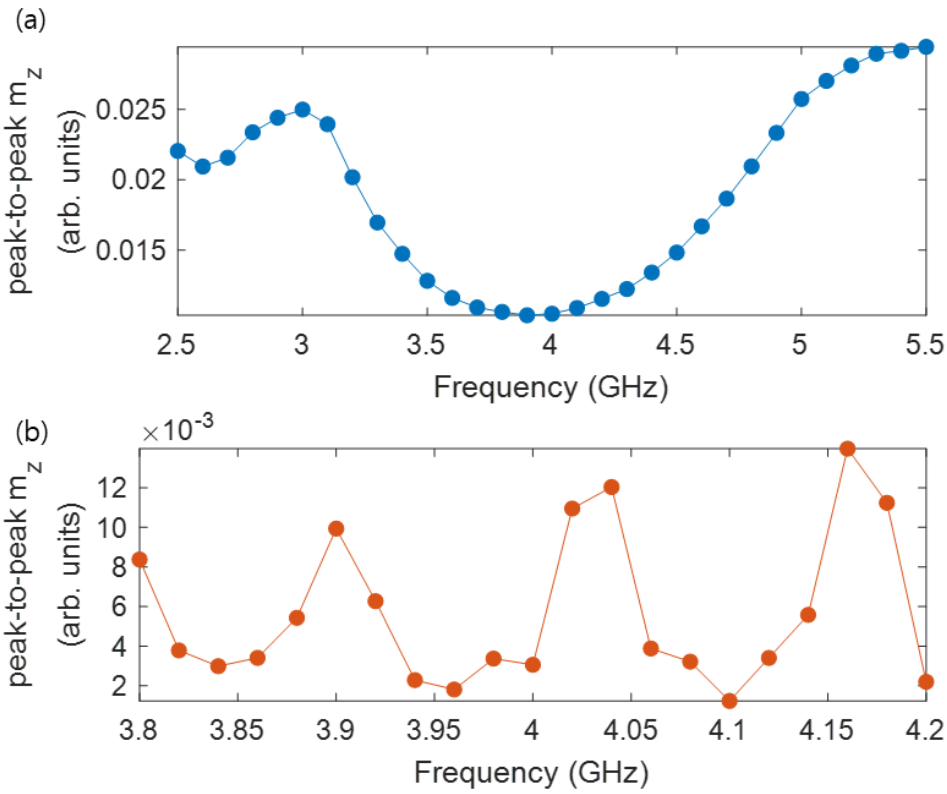

Figure 6.10: Spin wave amplitude after transmission through DBR structures. (a) Peak-to-peak amplitude of m_z after transmission through a DBR with $N = 3$ periods, showing the formation of a stop band near 4 GHz. (b) Peak-to-peak amplitude of m_z after transmission through a DBR cavity with cavity length d =2500 nm. Multiple transmission peaks are observed within the stop band, corresponding to cavity resonances.

high quality factor spin wave cavity will require magnetic materials with reduced damping, which should enable substantially higher cavity Q factors.

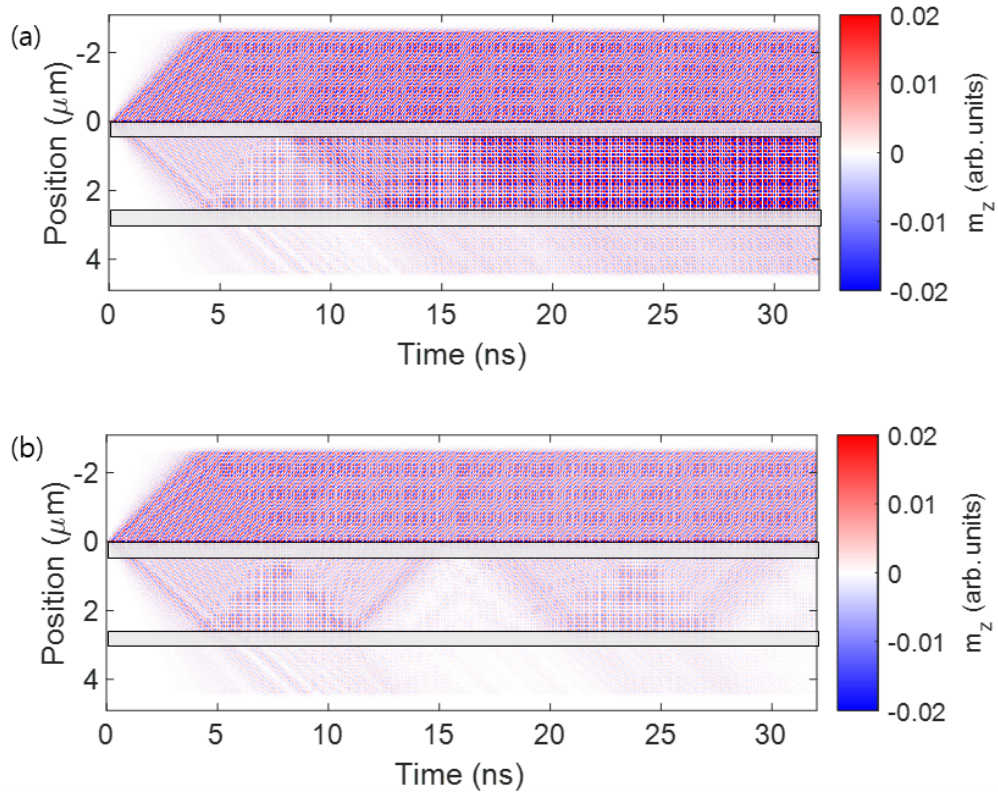

Figure 6.11: Spin wave dynamics in a DBR cavity. The gray regions indicate the locations of the DBR structures. (a) Resonant excitation ($f = 3.9$ GHz): repeated reflections inside the cavity lead to constructive interference, producing a standing wave within the cavity. (b) Off-resonant excitation ($f = 3.84$ GHz): in contrast to (a), the spin wave undergoes destructive interference during multiple reflections and transmissions, resulting in a strongly suppressed amplitude inside the cavity.

6.3 Spin wave reflector

In the previous section, micromagnetic simulations demonstrated that the DBR structure reflects only spin waves with wavelengths matching the structural periodicity. In this section, we aim to experimentally realize and verify this behavior. One key difference from the previous simulations lies in the wavelength of the spin waves. Due to computational limitations, the simulations were performed on nanometer-scale structures, whereas the DBR structure was fabricated at the micrometer-scale to ensure reliable device fabrication. Another important difference is the origin of the periodic modulation. While the simulations employed thickness modulation to form the DBR structure, the experimental implementation was achieved by depositing nickel (Ni) stripes on a YIG film, thereby introducing periodic modulation of the magnetic properties to realize the DBR structure. Figure 6.12 shows the fabricated spin wave DBR. Four Ni stripes with a thickness of 100 nm and a width of 2 μm were patterned on a 100 nm thick YIG film, with a periodic spacing of 30 μm. Spin wave antennas were placed on both sides of the DBR structure to excite and detect spin waves.

We measure the transmission parameter ($\mathbf{S}_{12}$) using a VNA while sweeping the external magnetic field. Figure 6.13 (a) shows the resulting transmission spectra. Several prominent dips appear that are absent in the plain YIG data of Figure 5.2. These dips are even clearer in the enlarged view on Figure 6.13 (b). The data confirm that the spin wave DBR acts as a frequency dependent reflector. We also find that the dip depth and bandwidth depend on the ratio of the Ni stripe width to the lattice constant. In our device, the Ni stripes are 2 μm wide with a lattice constant of 30 μm. By contrast, in another device with the same stripe width but a smaller lattice constant of 4 μm, the transmission was suppressed over the entire frequency range with little frequency selectivity. When

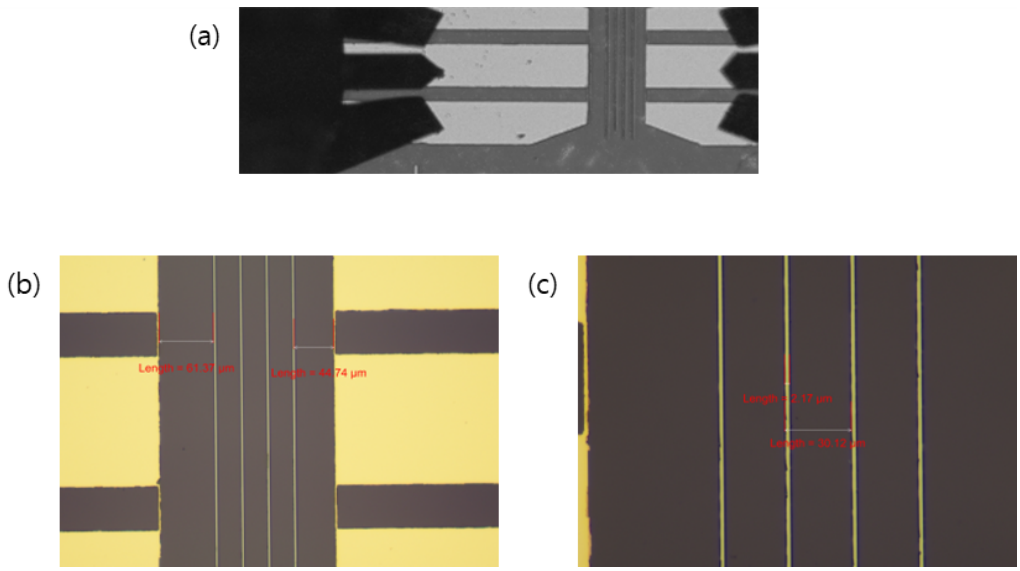

Figure 6.12: Spin wave reflector. An array of nickel stripes is patterned between two stripline antennas. (a) For the VNA measurements, the device was contacted using a CPW tip probe. The antennas connected to both ports generate spin waves, which then propagate through the region with the periodic structure. (b,c) Bragg structure formed by nickel stripes. The period of the periodic structure is 30 μm, and the width of each nickel stripe is 2 μm.

$a = 4\ \mu$m, the filling fraction of the Ni stripes becomes relatively large. We therefore expect a substantial increase in damping because Ni is significantly more lossy than YIG, which suppresses spin wave propagation over the entire frequency range, driving the system into a strongly overdamped regime. This provides a plausible explanation for the broadband reduction observed in the transmission. Achieving an ideal frequency selective filter with deep, narrow stop bands will therefore require further optimization of the stripe geometry. To verify the origin of the dips, we compare the transmission data with the spin wave dispersion relation. Figure 6.13 (d) shows an overall reduction in transmission, and more importantly, the dip frequencies coincide with the Bragg condition inferred from the dispersion.

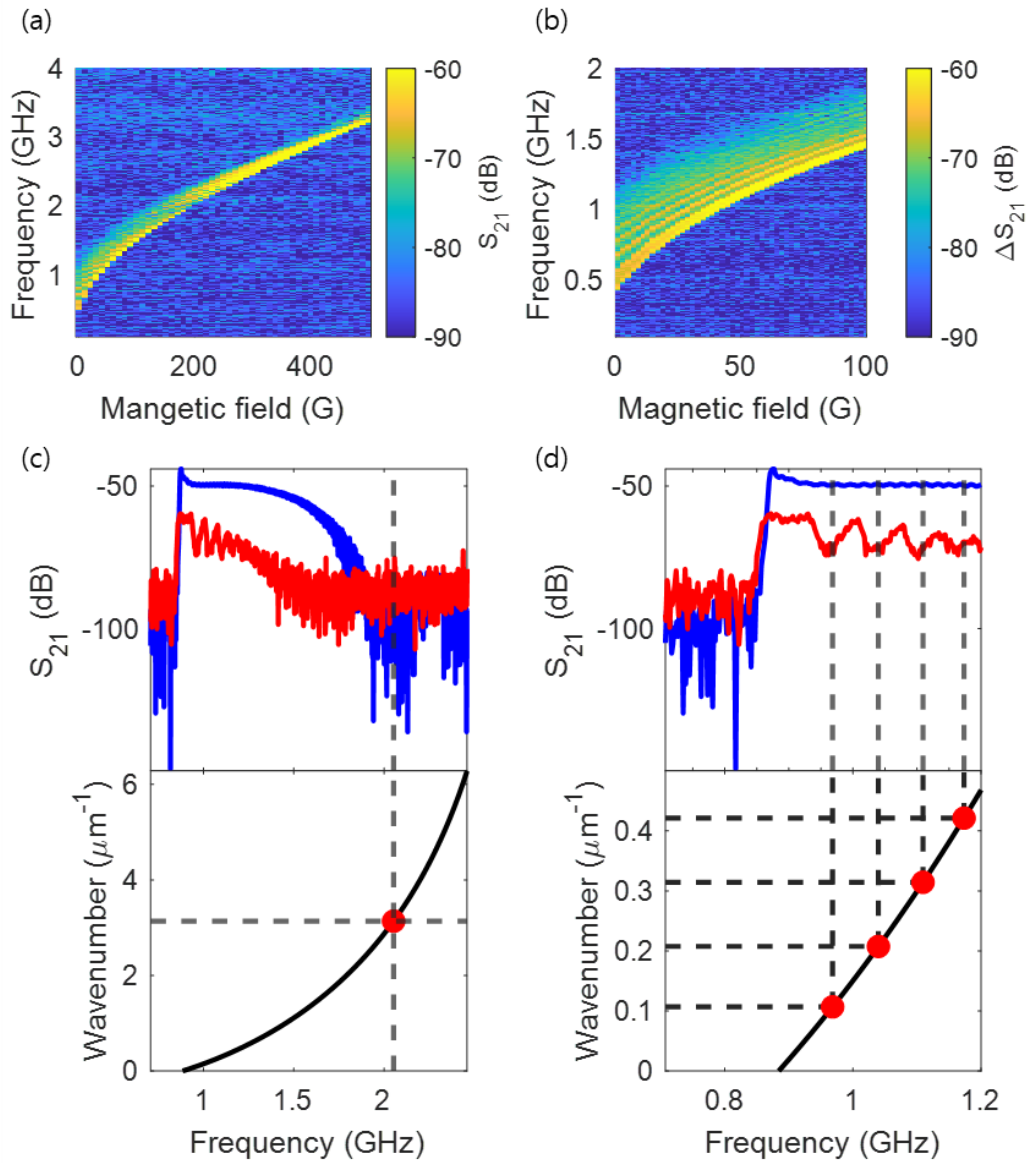

Figure 6.13: Transmission spectra of the spin wave reflector. (a) Coarse field sweep. (b) Fine sweep at low magnetic fields. (c) Full spectrum showing DBR induced dips in the low frequency range. (d) Enlarged view of the low frequency region. The dip frequencies correspond to wavevectors that satisfy the Bragg condition according to the spin wave dispersion relation.

6.4 Conclusions

In this chapter, we examined whether a DBR structure can reflect spin waves in a manner analogous to optical DBRs. To this end, we first reviewed optical DBR cavities and confirmed that the DBR formalism successfully describes their reflectance, transmittance, and FSR. We then employed micromagnetic simulations to verify that spin waves in a DBR structure exhibit Bragg condition dependent reflection and transmission, similar to the optical case. In addition, our simulations showed that a cavity formed by two such reflectors can confine spin waves within a defined region.

For an experimental realization, we fabricated a DBR on a YIG film by introducing a spatial modulation using Ni stripes, and demonstrated that this structure selectively transmits spin waves according to the Bragg condition. However, the presence of Ni substantially increased spin wave damping, limiting the efficiency of the spin wave DBR. If a method can be found to introduce spatial modulation without significantly increasing damping, together with a deeper theoretical understanding of spin wave propagation in periodically modulated media, it should be possible to build spin wave cavities. Such cavities would enable confined spin waves to serve as information carriers, providing a versatile platform for spin wave-based information transfer.

Chapter 7. Phonon-magnon coupling

Phonons [50] and magnons are promising candidates for flying quantum information carriers. Some qubit platforms couple more naturally to magnons, while others interact more efficiently with phonons. If we can build a hybrid quantum system that allows us to choose which type of flying excitation carries information, then different qubit platforms can be combined into a larger multi qubit cluster. Coupling between phonons and magnons is known as magnetoelastic coupling [88–91]. Magnetoelastic coupling arises from two reciprocal effects. The phenomenon in which a change in magnetization in-

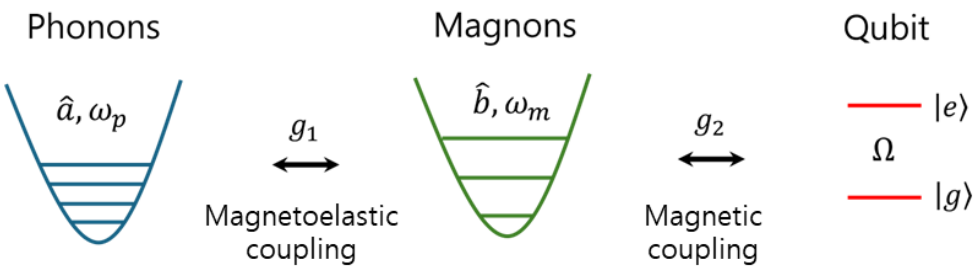

Figure 7.1: Illustration of a hybrid phonon-magnon-qubit system. Phonons with annihilation operator $\hat{a}$ and frequency ω_p are coupled to magnons with operator $\hat{b}$ and frequency ω_m via magnetoelastic interaction with coupling strength g_1. The magnons are further coupled to a two-level qubit system through magnetic coupling with strength g_2, where $|g\rangle$ and $|e\rangle$ denote the ground and excited states of the qubit, separated by energy Ω.

duces mechanical strain is called magnetostriction, whereas the phenomenon in which applied stress modifies the magnetization is known as the Villari effect [92]. This chapter first examines the transducers fabricated to generate surface acoustic waves (SAWs) and verifies SAW generation through transmission measurements. Next, we theoretically analyze phonon-magnon coupling and experimentally confirm its presence via transmission measurements. Finally, by integrating the system with an NV center scanning setup, we demonstrate that spin waves produced through NV-phonon-magnon coupling interact with NV centers.

7.1 Surface acoustic wave

We use a SAW for phonon driving. A SAW is an acoustic wave that propagates along the surface, and its amplitude decays into the substrate with depth. Many piezoelectric substrates can support SAWs, such as $LiNbO_3$, quartz, ZnO, AlN, and GaAs. Because each material has different acoustic velocities, operating frequencies, and wave modes, we must choose a piezoelectric substrate that is easy to fabricate and supports SAWs in the 2 - 3 GHz range to couple to NV centers. We use lithium niobate ($LiNbO_3$) as the SAW substrate, specifically a 128° YX-cut wafer with single side polishing. $LiNbO_3$ is commercially available in SAW grade and optical grade. Optical grade $LiNbO_3$ is transparent, whereas SAW grade $LiNbO_3$ is not. In our measurements, we do not observe a distinct difference in SAW performance between the two grades. Owing to the crystal symmetry of $LiNbO_3$, the material has three principal axes, X, Y, and Z [93]. The cut plane and SAW propagation direction affect the electromechanical coupling coefficient, wave velocity, and wave type. In the cut notation, the first letter indicates the surface normal and the second letter indicates the rotation axis used to tilt the cut by a specified

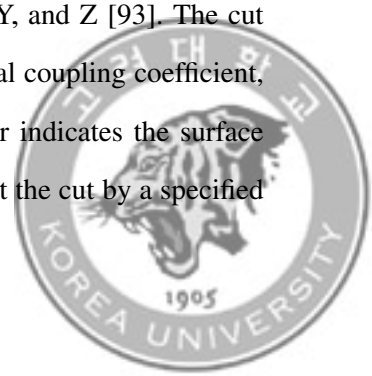

angle. For example, a 128° YX cut refers to a surface whose normal is along the Y axis and which is obtained by rotating the surface by 128° about the X axis. We tested two orientations, 128° YX cut and YZ cut, and found that the 128° YX cut produces much stronger SAWs than the YZ cut [1]. In double side polished $LiNbO_3$, not only surface waves but also bulk acoustic waves can be excited because both surfaces are polished. To excite SAWs on $LiNbO_3$, we fabricate an interdigital transducer (IDT). The IDT converts an applied AC electrical signal into a mechanical surface wave [94]. The SAW generation efficiency depends on the IDT properties, including the aperture, finger width, thickness, electrode configuration, and electrode material. Our IDT is made of aluminum, with a 120 μm aperture, 2 μm finger width, and 50 nm thickness. We tested both Au and Al as IDT metals and found that Al provides better performance. We speculate that this discrepancy arises from the differences in material properties between gold and aluminum. Although gold offers superior electrical performance compared to aluminum, its higher density increases the mass loading of the fabricated electrodes. We therefore believe that the additional weight on the surface enhanced the attenuation of the SAW, leading to reduced SAW transmission.

To evaluate the IDT performance, we place two identical IDTs facing each other with a separation of $\sim$ 1 mm. Figure 7.4 (a) shows the transmission (S_{12}) measured by a VNA. In this signal, no clear SAW feature is visible. Because an IDT launches not only acoustic waves but also electromagnetic waves, the direct transmission between IDT 1 and IDT 2 is dominated by the electromagnetic background, making the SAW contribution difficult to observe directly [95]. To isolate the SAW contribution from the transmission, we exploit the large difference in propagation velocities between acoustic and electromagnetic waves. In $LiNbO_3$, SAWs travel at about $\sim$ 3 km/s, whereas electromagnetic waves propagate at the speed of light, 3×10^8 m/s. Figure 7.4 (b) shows the transmission in the time

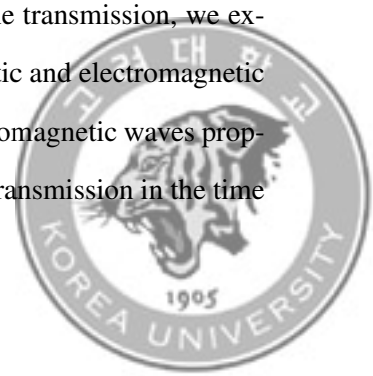

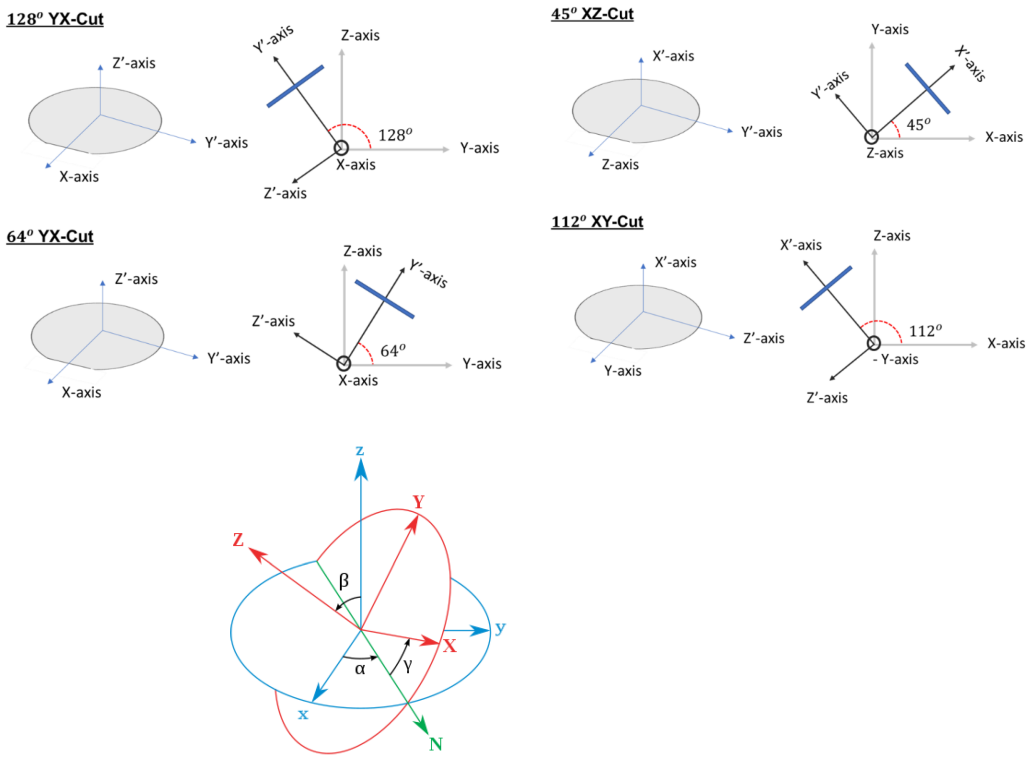

Figure 7.2: Different orientational cuts of the Lithium Niobate crystal (top) and the Eulerian angles (bottom). Adapted from [1]

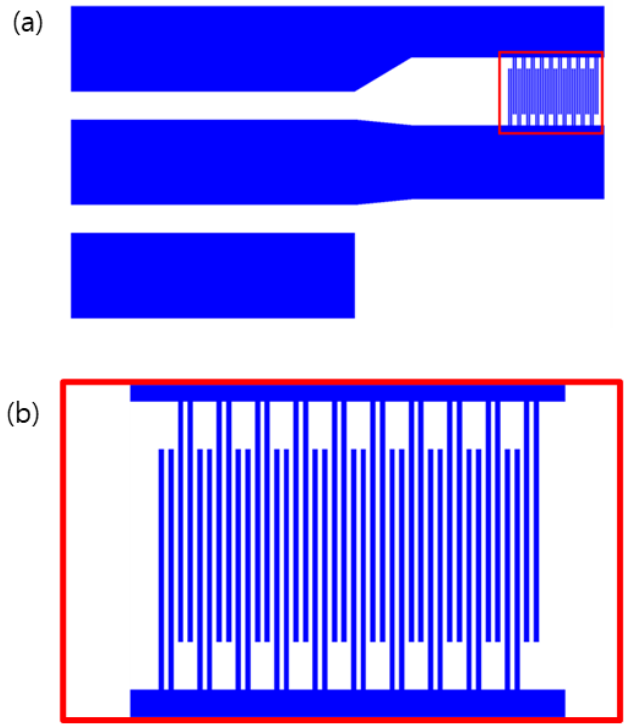

Figure 7.3: Design of the IDT. (a) The signal pad is flanked by ground pads on both sides. The upper ground pad and the signal pad are extended and connected to the region where the IDT structure is located. The lower ground pad is included because the probe tips used for VNA measurements are arranged symmetrically. (b) Enlarged view of the IDT region. Fingers are connected to both pads, and each pair of fingers is connected to the same pad.

domain. The rapidly decaying signal near 0 μs is attributed to the electromagnetic wave. A second envelope appears around 0.3 μs. This delay matches the expected acoustic time of flight, (distance between the IDTs)/(SAW velocity), and is therefore assigned to the SAW signal. In addition, another envelope is observed around 1.2 μs. We attribute this to a SAW that completes one round trip after being reflected by an IDT. From the time domain analysis, we identify why the SAW signal is not visible in the raw transmission spectrum. To isolate the SAW contribution, we apply a time gate to select only the time window (265 ns - 415 ns) in the time domain and then transform the gated signal back into the frequency domain. Figure 7.4 (c) shows the resulting transmission after time gating [96]. Multiple distinct peaks are observed. Because the peak frequencies agree with those expected from the IDT finger periodicity, we conclude that SAWs are successfully generated and propagate between the two IDTs.

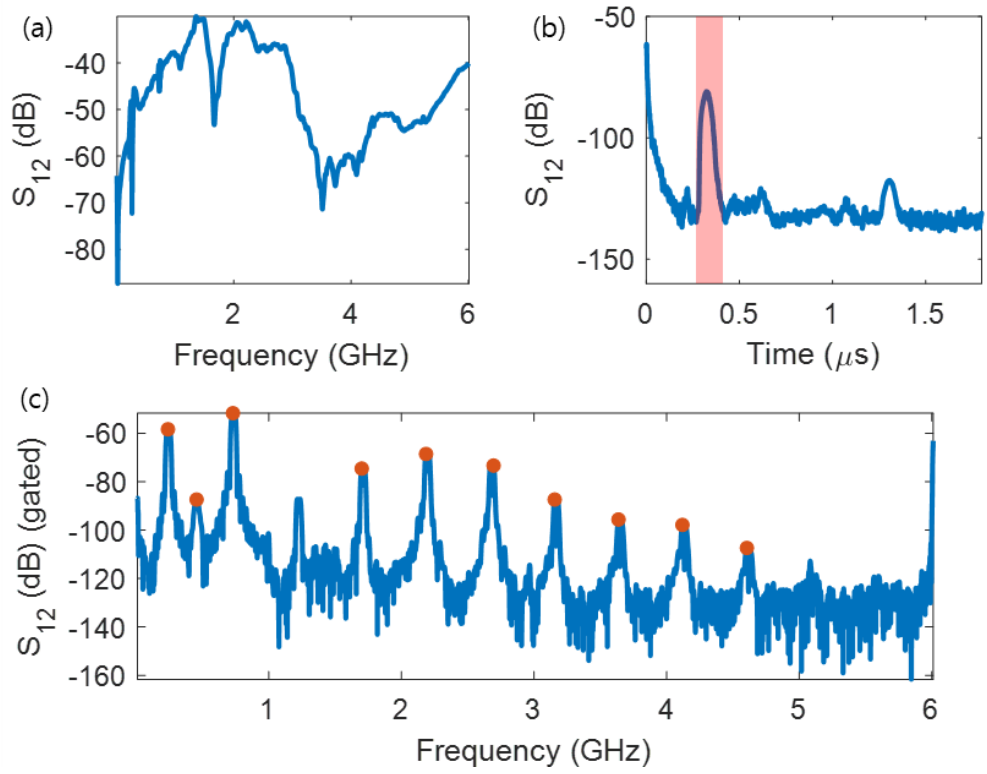

Figure 7.4: Transmission (S_{12}) of SAW. (a) S_{12} as a function of frequency. Input power was -10 dBm. In these measurements, the SAW modes cannot be clearly resolved. (b) Time domain transmission (S_{12}) acquired from the VNA. Because the acoustic velocity is slower than that of the electromagnetic wave, the SAW contribution can be resolved in the time domain. The red shaded area represents the estimated SAW power. (c) Transmission (S_{12}) signal after time gating. Unlike the previous measurements (a), the SAW mode is clearly visible in this signal. The fundamental mode frequency is 240 kHz, and higher harmonic modes at integer multiples of this frequency are also observed. The SAW mode frequencies are marked with red dots.

7.2 Theoretical description for magnetoelastic coupling

The mechanical and magnetic properties of ferromagnetic materials are intrinsically coupled. Magnetostriction denotes the elastic deformation generated by magnetization, whereas the Villari effect describes the reciprocal influence of elastic deformation on magnetization. Both phenomena can be formulated in terms of the magnetoelastic energy density

$$\begin{aligned} u_{\text{mag-ela}} =& b_1 \left[\varepsilon_{xx} \left(m_x^2 - \frac{1}{3} \right) + \varepsilon_{yy} \left(m_y^2 - \frac{1}{3} \right) + \varepsilon_{zz} \left(m_z^2 - \frac{1}{3} \right) \right] \\ &+ 2b_2 [\varepsilon_{xy} m_x m_y + \varepsilon_{xz} m_x m_z + \varepsilon_{yz} m_y m_z] \end{aligned} \tag{7.1}$$

Here ε_{ij} is the ij component of the strain tensor

$$\varepsilon_{ij} = \frac{1}{2} \left(\partial_i u_j + \partial_j u_i \right) \tag{7.2}$$

where $\mathbf{u}$ denotes the displacement field. The quantities m_i are the components of the unit magnetization $\mathbf{m} = \mathbf{M}/M_s$, and M_s is the saturation magnetization. The magnetoelastic constants b_1 and b_2 characterize the coupling of the magnetization to the diagonal and off-diagonal strain components, respectively. From $u_{\text{mag-ela}}$, the magnetoelastic contribution to the stress tensor is defined as

$$\sigma_{ij}^{\text{eff}} = \frac{\partial u_{\text{mag-ela}}}{\partial \varepsilon_{ij}} \tag{7.3}$$

and the associated body force $\mathbf{f}_{\text{eff}}$ follows as

$$f_i^{\text{eff}} = \partial_j \sigma_{ij}^{\text{eff}} \tag{7.4}$$

Carrying out the derivative gives

$$\mathbf{f}_{\text{eff}} = 2b_1 \begin{pmatrix} m_x\,\partial_x m_x \\ m_y\,\partial_y m_y \\ m_z\,\partial_z m_z \end{pmatrix} + 2b_2 \begin{pmatrix} m_x(\partial_y m_y + \partial_z m_z) + m_y\partial_y m_x + m_z\partial_z m_x \\ m_y(\partial_x m_x + \partial_z m_z) + m_x\partial_x m_y + m_z\partial_z m_y \\ m_z(\partial_x m_x + \partial_y m_y) + m_x\partial_x m_z + m_y\partial_y m_z \end{pmatrix} \tag{7.5}$$

Conversely, elastic deformation produces an effective magnetic field that enters the LLG equation. It is obtained by varying the energy density with respect to the magnetization

$$\mathbf{H}_{\text{eff}} = -\frac{1}{\mu_0}\frac{\partial u_{\text{mag-ela}}}{\partial \mathbf{M}} = -\frac{1}{\mu_0 M_s}\frac{\partial u_{\text{mag-ela}}}{\partial \mathbf{m}} \tag{7.6}$$

Evaluating the derivative yields

$$\mathbf{H}_{\text{eff}} = -\frac{1}{\mu_0 M_s}\left[2b_1 \begin{pmatrix} \varepsilon_{xx} m_x \\ \varepsilon_{yy} m_y \\ \varepsilon_{zz} m_z \end{pmatrix} + 2b_2 \begin{pmatrix} \varepsilon_{xy} m_y + \varepsilon_{xz} m_z \\ \varepsilon_{yz} m_z + \varepsilon_{xy} m_x \\ \varepsilon_{xz} m_x + \varepsilon_{yz} m_y \end{pmatrix} \right] \tag{7.7}$$

We take the external magnetic field along $\hat{z}$ and assume a saturated equilibrium state so that $m_z \simeq 1$ and $m_x, m_y \ll 1$. Retaining only terms linear in the small dynamical variables $\mathbf{u}$ and (m_x, m_y), the effective body force and field reduce to

$$\mathbf{f}_{\text{eff}} \simeq 2b_2 \begin{pmatrix} \partial_z m_x \\ \partial_z m_y \\ \partial_x m_x \end{pmatrix}, \qquad \mathbf{H}_{\text{eff}} \simeq -\frac{1}{\mu_0 M_s} \begin{pmatrix} 2b_2\varepsilon_{xz} \\ 2b_2\varepsilon_{yz} \\ 2b_1\varepsilon_{zz} \end{pmatrix} \tag{7.8}$$

To study waves in the xz plane (normal to y), we consider a wavevector with only x and z components, $\mathbf{k} = (k_x, 0, k_z)$. The elastic wave equations including $\mathbf{f}_{\text{eff}}$ become

$$-\rho\omega^2 u_x = -C_{11}k_x^2 u_x - C_{44}k_z^2 u_x - (C_{12}+C_{44})k_x k_z u_z + 2b_2\, ik_z m_x \tag{7.9}$$

$$-\rho\omega^2 u_y = -C_{44}(k_x^2 + k_z^2)u_y + 2b_2\, ik_z m_y \tag{7.10}$$

$$-\rho\omega^2 u_z = -C_{11}k_z^2 u_z - C_{44}k_x^2 u_z - (C_{12}+C_{44})k_x k_z u_x + 2b_2\, ik_x m_x \tag{7.11}$$

Here C_{11}, C_{12}, and C_{44} are stiffness tensor components governing the elastic wave. The terms proportional to b_2 represent magnetoelastic body forces. Including $\mathbf{H}_{\text{eff}}$ in the LLG equation and linearizing yields

$$i\omega m_x = -\omega_{fy} m_y - \frac{\gamma b_2}{M_s}\, ik_z u_y \tag{7.12}$$

$$i\omega m_y = \omega_{fx} m_x + \frac{\gamma b_2}{M_s}\, i(k_z u_x + k_x u_z) \tag{7.13}$$

,with

$$\omega_{fx} = \gamma\mu_0 H_{\text{ext}} + \gamma\mu_0 M_s \left[\alpha_{\text{ex}} k^2 + \sin^2\theta \left(1 - \frac{1-e^{-kd}}{kd}\right)\right] \tag{7.14}$$

$$\omega_{fy} = \gamma\mu_0 H_{\text{ext}} + \gamma\mu_0 M_s \left[\alpha_{\text{ex}} k^2 + \frac{1-e^{-kd}}{kd}\right] \tag{7.15}$$

where H_{ext} is the applied magnetic field, θ is the angle between $\mathbf{k}$ and the external field, α_{ex} is the exchange constant, and d is the film thickness. The terms proportional to b_2 represent magnetoelastic effective fields. Combining Equation (7.9) - (7.11) and (7.12) - (7.13) yields five coupled linear equations. To separate longitudinal and transverse acous-

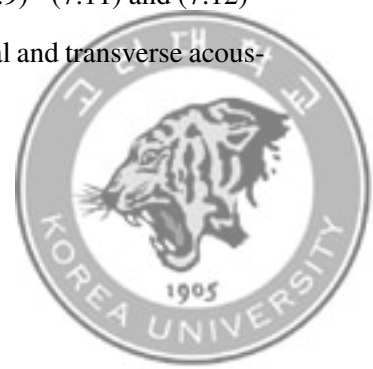

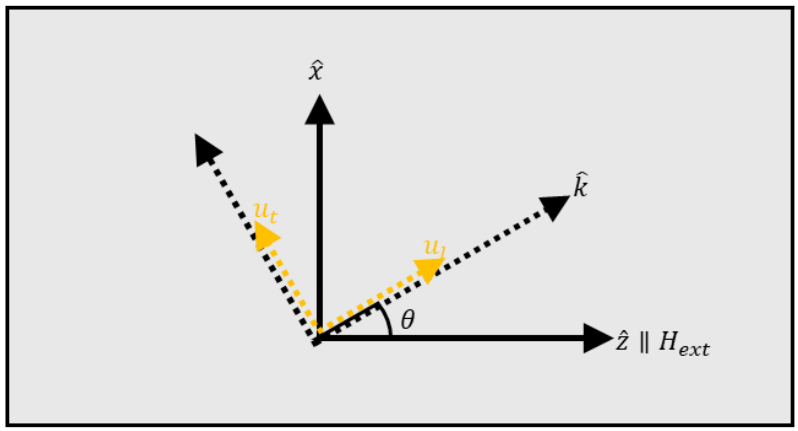

Figure 7.5: Axis orientation. The external magnetic field is applied along the $\hat{z}$ direction, and wave propagation occurs along $\hat{k}$. The angle between $\hat{z}$ and $\hat{k}$ is denoted by θ. The displacement field is decomposed into longitudinal (u_l) and transverse (u_t) components.

tic modes with respect to **k**, we introduce

$$u_x = u_l \sin\theta + u_t \cos\theta, \qquad u_z = u_l \cos\theta - u_t \sin\theta, \qquad k_x = k\sin\theta, \quad k_z = k\cos\theta$$

The coupled system becomes

$$\begin{aligned}
(\omega^2 - \omega_l^2)\sin\theta\, u_l + (\omega^2 - \omega_t^2)\cos\theta\, u_t + \frac{2ib_2 k\cos\theta}{\rho} m_x &= 0 \\
(\omega^2 - \omega_t^2) u_y + \frac{2ib_2 k\cos\theta}{\rho} m_y &= 0 \\
(\omega^2 - \omega_l^2)\cos\theta\, u_l - (\omega^2 - \omega_t^2)\sin\theta\, u_t + \frac{2ib_2 k\sin\theta}{\rho} m_x &= 0 \\
\frac{i\gamma b_2}{M_s} k\cos\theta\, u_y + i\omega m_x + \omega_{fy} m_y &= 0 \\
\frac{i\gamma b_2}{M_s} k\sin 2\theta\, u_l + \frac{i\gamma b_2}{M_s} k\cos 2\theta\, u_t + \omega_{fx} m_x - i\omega m_y &= 0
\end{aligned} \tag{7.16}$$

Here $\omega_l = \sqrt{\frac{C_{11}}{\rho}}\,k$ and $\omega_t = \sqrt{\frac{C_{44}}{\rho}}\,k$ denote the dispersions of the longitudinal and transverse acoustic modes, respectively.

Figure 7.6 shows the solutions of Equation (7.16). The three panels correspond to different propagation angles, $\theta =$ (a) 0, (b) $\pi/6$, and (c) $\pi/2$. The dashed lines indicate the uncoupled dispersions (black: longitudinal elastic wave; green: transverse elastic wave; blue: spin wave). The emergence of an anticrossing near the intersection of two dashed branches signifies hybridization of the modes, and the coupling strength is quantified by the size of the resulting gap. In particular, the anticrossing gap at the intersection between the longitudinal acoustic wave and the spin wave branch varies with the propagation angle. This angle dependent gap demonstrates that the strength of magnetoelastic coupling between elastic and spin wave modes depends on the wavevector orientation. This will be verified experimentally in next section.

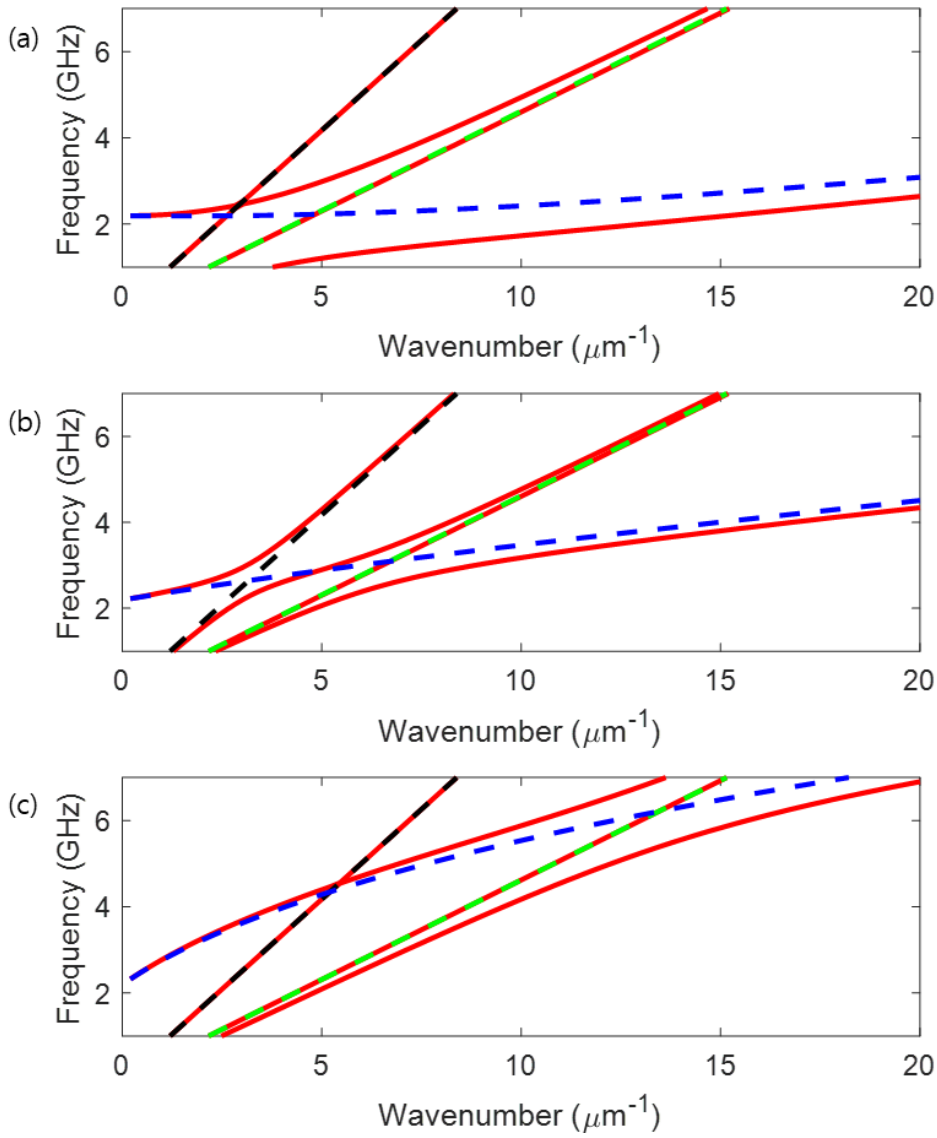

Figure 7.6: Dispersion of magnetoelastic wave. The red lines are solutions of Equations (7.16). The dashed lines are uncoupled waves (Black : longitudinal elastic wave, Green : transverse elastic wave, Blue : spin wave). The parameter are used $M_s = 480$ kA/m, $\mu_0 H_{ext} = 10$ mT, $\rho = 8900$ kg/m^3, $v_l = 5246$ m/s, $v_t = 2903$ m/s, $\alpha_{ex} = 5.53 \times 10^{-17}$ m^{-2}, $d = 20$ nm and $b_2 = 10$ MJ/m^3. θ = (a) 0, (b) $\pi/6$ and (c) $\pi/2$.

7.3 Transport of magnetoelastic wave

We place a Ni film between two IDTs. The Ni thickness is 20 nm, and it is capped with a 5 nm Au layer [97]. As shown in Figure 7.7, the two IDTs are connected to a VNA through contact probes. When coupling between spin waves and elastic waves occurs, part of the SAW power is transferred to spin waves, leading to a reduction in the transmitted SAW signal compared with Figure 7.4 (c) [98–100]. To maximize the coupling, we set the external bias magnetic field direction to $\theta = \pi/4$. Figure 7.8 shows the trans-

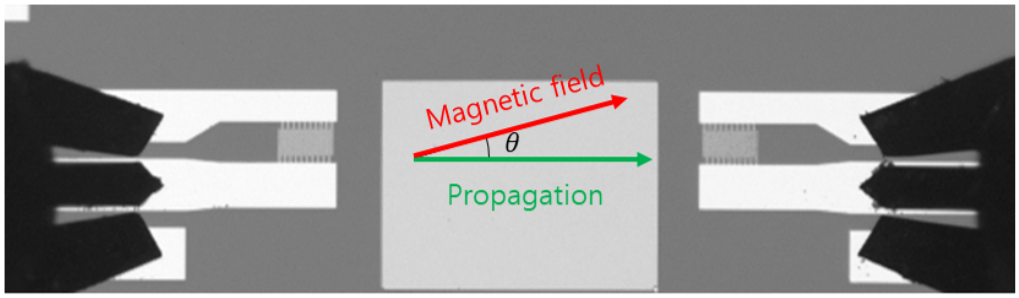

Figure 7.7: Image of total device. Two IDTs are used for SAW excitation and detection. The Ni film lies in the SAW propagation path, and a 5 nm Au layer encapsulates the Ni film.

mission as the bias field is swept. For some low frequency SAW modes, the transmission does not change noticeably with magnetic field. However, at higher SAW frequencies, the field dependent transmission change becomes clear. The frequency dependence of the coupling is summarized in Figure 7.8 (c). Higher frequency SAW modes generate stronger spin wave excitation, leading large transmission change. In Figure 7.8 (b), we plot the magnetic field values at which the SAW transmission reaches its minimum. At this magnetic field, the SAW transmission is reduced due to magnetoelastic coupling, and we observe that this reduction appears for both field polarities in the frequency range that

coincides with the Ni FMR frequency.

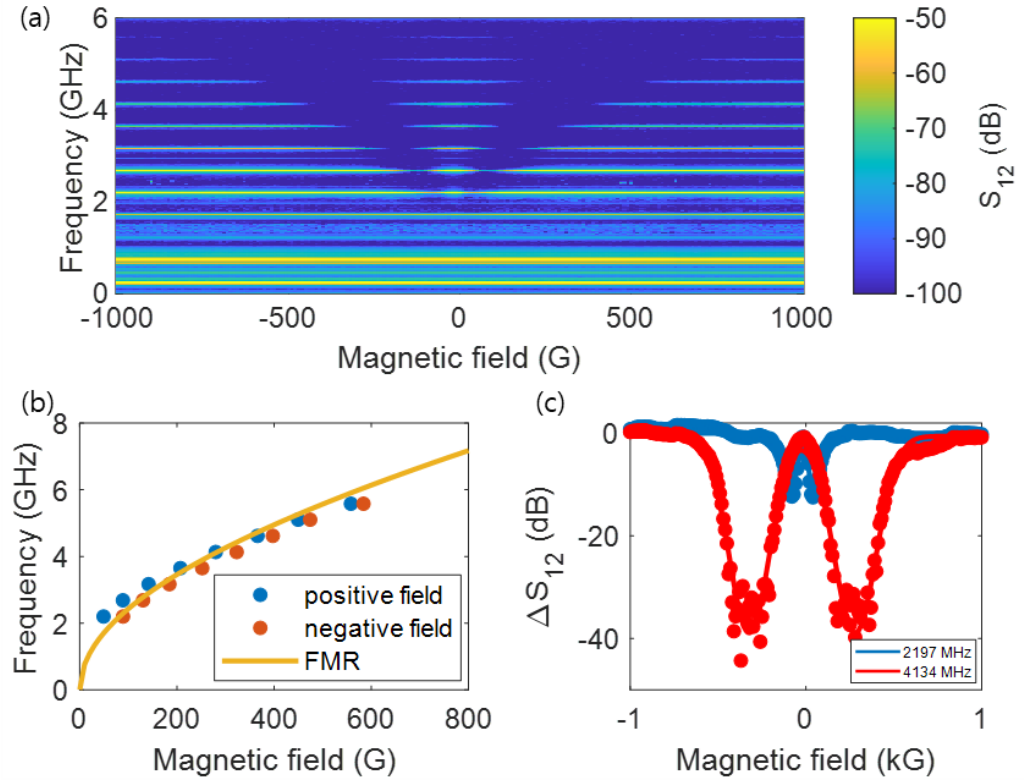

Figure 7.8: Results measured while varying the magnetic field. (a) Transmission measured as a function of magnetic field magnitude when the angle between the external field and the SAW propagation direction is 45°. (b) For each SAW mode, the dip frequencies induced by the magnetic field are plotted versus the external field magnitude. (c) SAW power variation of acoustic modes as function of magnetic field(blue: 2197 MHz, red: 4134 MHz).

Another key property of magnetoelastic coupling is that the coupling strength depends on the angle between the spin wave propagation direction and the bias magnetic field. As shown in Figure 7.6, the coupling between a longitudinal elastic wave and a magnetic wave varies with this angle. The SAW excited by the IDT on $LiNbO_3$ is a

Rayleigh type elastic wave, which contains a longitudinal component. The transmission change as a function of magnetic field direction is shown in Figure 7.9. We recorded the transmission while rotating the magnetic field angle, and from these data, Figure 7.9 (b) and (d) show that we reconstructed the field dependent transmission in angular space. The red dashed line indicates the maximum magnetic field used, 1 kG. As expected, the transmission change is largest for angles between 0 and $\pi/2$, but the maximum occurs at an angle slightly larger than $\pi/4$. We attribute this deviation from the theoretical expectation to the anisotropy field of the Ni film. We also find that a high frequency mode, such as the 5.101 GHz mode, is relatively insensitive to the magnetic field direction. We believe this is due to the broadening of the transmission dip.

At higher frequencies the intrinsic SAW transmission becomes weak, making it difficult to determine whether a feature corresponds to a genuine SAW mode. Nevertheless, the magnetoelastic coupling remains clearly visible at these high frequency modes, allowing us to distinguish SAW related features from non SAW background. In Figure 7.10, a clear distinction between SAW modes and non SAW modes is evident, even though the raw SAW transmission spectrum in Figure 7.4 (c) shows only weak signals above 5 GHz. From these observations, we confirm the presence of magnetoelastic coupling between SAWs and spin waves in the Ni film.

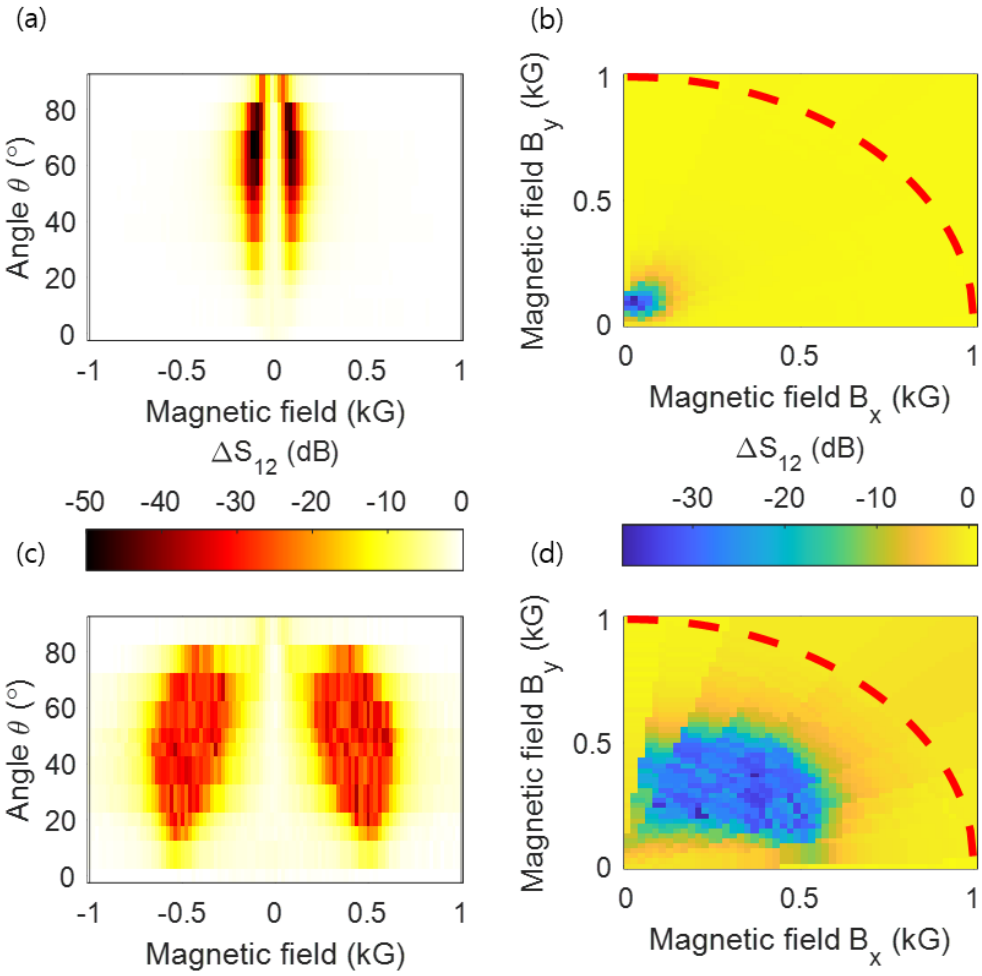

Figure 7.9: Magnetic field dependent changes in the transmission of SAW modes. The darker colored regions indicate where the SAW power is reduced due to spin wave coupling ((a) for the 2684 MHz mode and (b) for the 5101 MHz mode). The corresponding data were reprocessed into two dimensional maps with the magnetic field components on the horizontal and vertical axes. The blue regions represent the field range in which the SAW power is suppressed by spin waves ((c) for the 2684 MHz mode and (d) for the 5101 MHz mode). The maximum magnetic field magnitude used in the experiment was 1 kG, indicated by the red dashed line.

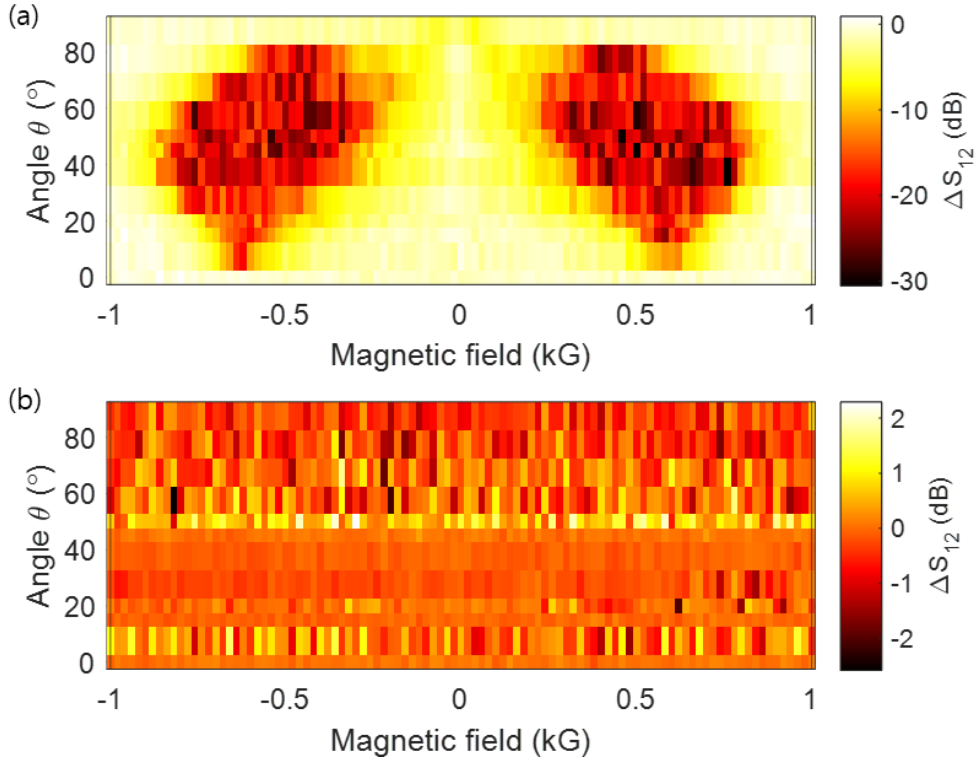

Figure 7.10: Magnetic field dependent changes in SAW transmission. In 7.4 (c), SAW modes above 5 GHz are not clearly visible because their transmission is too small. However, their response to the external magnetic field allows us to distinguish whether a peak corresponds to a SAW mode. (a) Magnetic field response of the highest frequency SAW mode that could be measured. (b) Magnetic field response of a peak that does not correspond to a SAW mode.

7.4 NV center manipulation by magnetoelastic wave

Like our experiments with YIG films, we detect magnetoelastic waves in the Ni film using a scanning probe with an attached NV center. Figure 7.11 (a) shows the NV center ground state frequency and the magnetoelastic frequency depend on the applied magnetic field. The ground state transition frequencies of the NV center are tuned by the external magnetic field, and the strength of the magnetoelastic coupling is also controlled by the field. To couple magnetoelastic waves to the NV center, the magnetoelastic wave frequency must be matched to an NV electronic transition by adjusting the external magnetic field. Among the available SAW modes, those near 3 GHz are resonant with the NV center ground state transitions. Figure 7.11 (b) and (c) show two different SAW modes, 1.712 GHz and 2.684 GHz. Each mode shows magnetoelastic coupling at a certain magnetic field. To be resonant for NV center frequency with SAW mode frequency, NV center frequency has to be tuned by magnetic field. The red dashed line indicates the magnetic field required for resonance. At SAW mode 1.712 GHz, magnetoelastic coupling is not efficient, far from magnetic field. But, at SAW mode 2.684 GHz, magnetoelastic coupling is resonant with magnetic field. We use SAW mode 2.684 GHz for magnetoelastic wave coupling with NV center.

Magnetoelastic wave in Ni film generate stray magnetic fields near the surface. We position NV probe few hundreds nm above Ni film. SAW is excited from IDT and magnetoelastic wave is excited inside Ni film and NV center near Ni film is affected by stray field made by magnetoelastic wave [101]. First of all, we measure CWESR by magnetoelastic wave. We observe CWESR driven by excitation of IDT. But from IDT, not only SAW, electromagnetic wave is also excited and propagated. To confirm origin of CWESR signal, we compare CWESR data from two different regions, inside of Ni re-

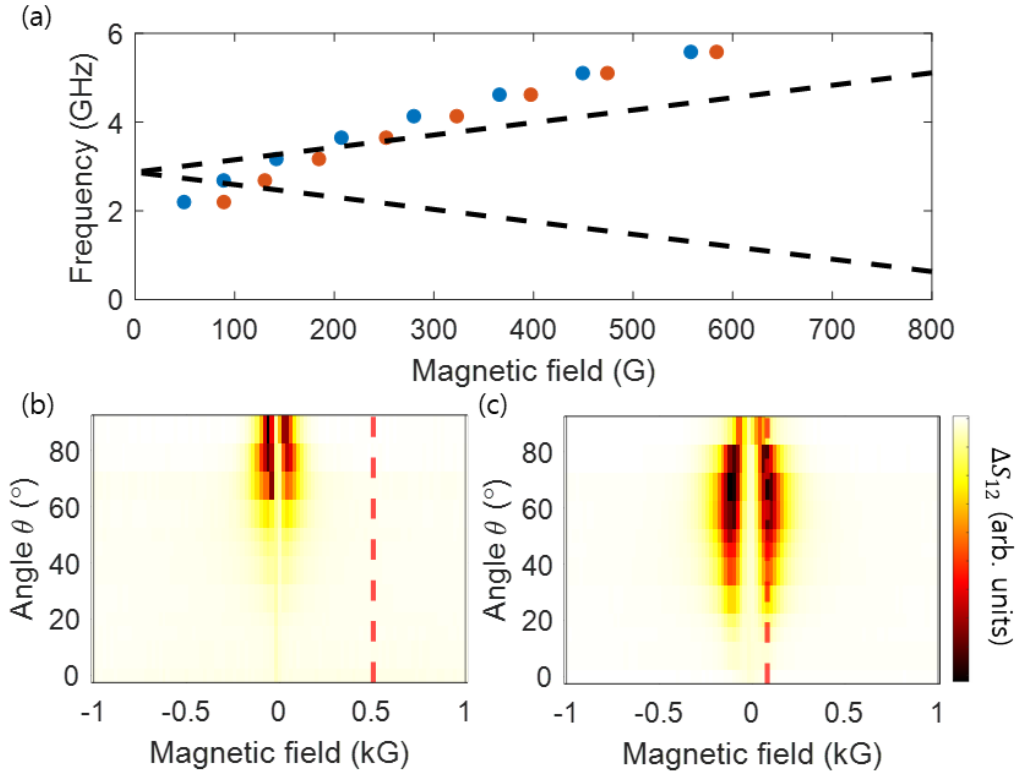

Figure 7.11: Magnetoelastic coupling and NV center matching based on magnetic field. (a) Frequency of NV ground state level (dashed line) and magnetoelastic wave in nickel acquired from VNA (blue dot). Magnetoelastic coupling maps at (b) 1712 MHz and (c) 2684 MHz. The red dashed line indicates the magnetic field magnitude at which the NV center ground state transition frequency matches the SAW mode frequency. The SAW mode at 1712 MHz does not intersect the NV center resonance, whereas the SAW mode at 2684 MHz matches the NV center frequency and can therefore coherently drive the NV center.

gion and outside of Ni region, but closer from IDT. If the observed CWESR were due to the electromagnetic wave from the IDT, the signal should be stronger closer to the IDT (outside the Ni region). Figure 7.12 (a) shows comparison of two CWESR data. CWESR get from outside of Ni region and closer to IDT is not noticeable. But CWESR get from inside of Ni region is clear dip at NV ground state level. From this, we convince CWESR signal driven by IDT is originated from magnetoelastic wave in Ni film. Furthermore, we drive Rabi oscillation by magnetoelastic wave. We record the NV center PL as a function of the pulse duration τ of magnetoelastic wave. Figure 7.12 (b) shows Rabi oscillation driven by magnetoelastic wave. We observe Rabi frequency driven by magnetoelastic wave is larger than driven by typical MW wire. We can manipulate NV center by magnetoelastic wave. CWESR and Rabi oscillation can be realized using magnetoelastic wave. In addition, manipulation by magnetoelastic wave is more power efficient than inductive MW wire. To manipulate NV center by MW wire, the wire must be placed close to NV center position. At certain situation, manipulation by magnetoelastic wave can be easier and more efficient than other ways.

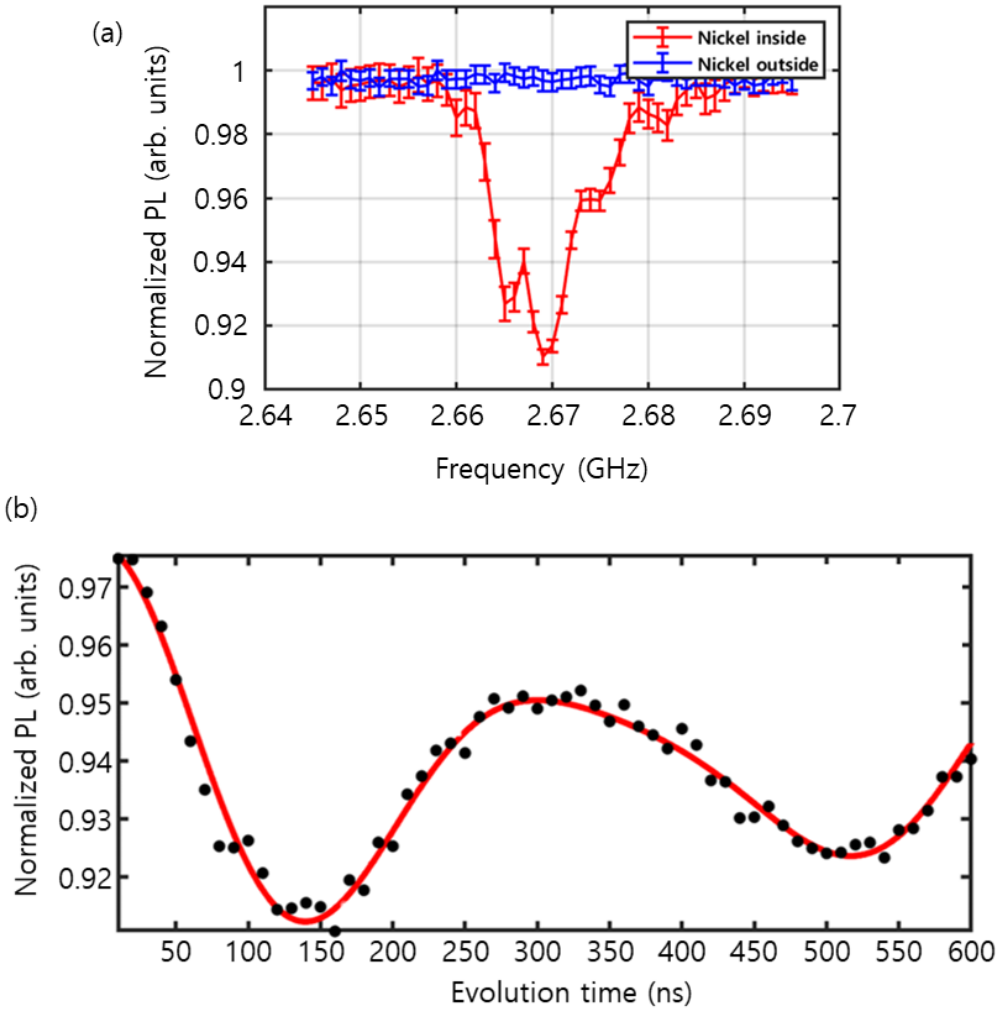

Figure 7.12: Measurement of magnetoelastic wave using an NV center. (a) Comparison of CWESR. The red data were measured on the nickel film, whereas the blue data were measured outside the nickel film. The SAW generates spin waves on the nickel film, and the resulting stray magnetic field enables us to detect the CWESR. (b) Rabi oscillation driven by magnetoelastic wave.

7.5 Imaging magnetoelastic wave

Waves can transmit information through physical quantities such as their wavelength and group velocity. These wave properties are crucial for understanding wave. Here, we focus on determining wavelength of magnetoelastic wave by coupling with NV center. One of the imaging techniques is to observe spin wave is X-ray magnetic circular dichroism (XMCD) [102, 103]. XMCD shows contrast for magnetization of the sample. But, in ferromagnetic material like Ni, magnetization wave is mixed with local magnetization pattern, like magnetic domain. To split between magnetization wave and local magnetization, two out-of-phase XMCD data are subtracted. Local magnetization variation which is not dependent on phase of waves are canceled and dynamic magnetization which is dependent on phase of waves get high contrast.

To acquire phase resolved Rabi oscillation, We drive Rabi oscillation by two independent function generators, one for excitation of SAW, the other for conventional wire to excite MW electromagnetic wave. Two different magnetic waves affect on NV center, so that Rabi oscillation frequency is defined from sum of the two different magnetic waves. As relative phase between two sources changes, resultant power of magnetic wave are changes. Figure 7.13 (a) shows Rabi frequency as a function of relative phase. When the two waves are in phase (300°), they interfere constructively, increasing the net driving field. When they are out of phase (120°), they interfere destructively, reducing the net field. This phase dependance of Rabi oscillation is determined by the path through that wave pass. Figure 7.13 (b) shows the phase sweep image. The image is taken along the x axis, which is tilted by about 18° relative to the wave propagation direction. The phase offset varies along x with a slope of $237^\circ/\mu$m. From this slope, the wavelength is estimated as $360^\circ/(237^\circ/\mu m) \times \cos(18^\circ) = 1.45\ \mu$m. This value is in good agree-

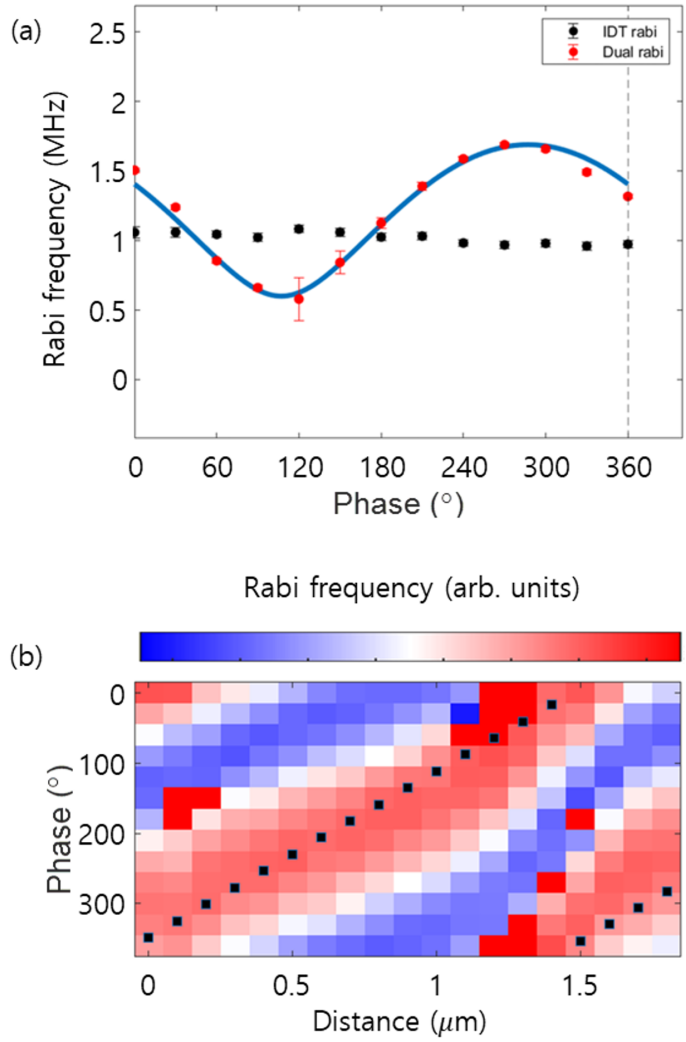

Figure 7.13: Interference pattern. (a) Rabi oscillations are driven by two waves that interfere with each other. The black data were acquired with the NV center driven by the SAW alone. The red data were acquired with the NV center driven by the combined field of two interfering waves. (b) Measurement of magnetoelastic wave wavefronts using NV centers. At each position, we perform the same measurement as shown in (a). The plotted data are normalized by the maximum Rabi frequency obtained at each measurement point. The black markers indicate, at each position, the phase at which the Rabi frequency is largest, allowing the wavelength to be determined.

ment with the wavelength expected for a SAW, given by (SAW velocity)/(frequency): 3992 m/s/2684 MHz = 1.49 μm.

7.6 Conclusions

In this chapter, we demonstrated magnetoelastic interactions between phonons and magnons. We first constructed a system to excite acoustic waves and observed, in the electrical transmission spectrum, a clear attenuation of the acoustic signal at acoustic modes. This reduction indicates energy transfer from the acoustic mode into magnons via magnetoelastic coupling. We further showed that this coupling can be detected through the Rabi oscillations of NV centers, which are driven by stray magnetic fields generated by the magnetoelastically excited magnons. Unlike purely electrical measurements, the NV scanning magnetometry setup allowed us to probe these magnetoelastically generated spin waves directly in real space and to extract their wavelength. Overall, the NV center state manipulation induced by phonon-magnon coupling presented here lays the groundwork for a hybrid platform interfacing two types of flying carriers (phonons and magnons) and offers a promising route toward expanding hybrid connections between NV centers and other qubits in future work.

Chapter 8. Conclusions

This dissertation experimentally demonstrates that waves mediated by magnons and phonons can interact with NV centers in diamond, highlighting their potential as building blocks for NV center-based hybrid quantum systems.

First, we show that strain waves generated by phonons can measurably affect NV centers. By simultaneously exciting two vibrational modes, we demonstrate partial tunability of the strain coupling strength. This multimode strain engineering introduces additional controllable degrees of freedom beyond conventional single mode strain coupling, providing a more versatile route for controlling NV centers via strain.

Second, we demonstrate that spin waves generated by magnons can manipulate the NV center spin state. Combined with an imaging configuration, this capability enables visualization of spin wave wavefronts using NV centers. In addition, compared with conventional antenna driven control, spin wave-based control can induce faster Rabi oscillations with substantially lower power [65], which is advantageous for applications requiring rapid state manipulation while minimizing dissipation and unwanted heating.

Third, we demonstrate phonon to magnon transduction and its interface to NV centers by launching SAWs to generate spin waves. The generation of spin waves by SAWs is electrically verified using a vector network analyzer, and the acoustically generated spin waves are shown to induce NV center spin state transitions. Together, these results indi-

cate that NV centers can serve as a node in hybrid connections involving both phonons and magnons, offering added flexibility for constructing NV center-based hybrid quantum architectures.

Overall, the experiments in this dissertation establish proof-of-principle interactions between NV centers and externally driven strain and spin waves in the classically driven regime. For coherent quantum information transduction, however, the central bottleneck is reaching the single quantum limit, where the vacuum (single quantum) coupling strength exceeds the relevant decoherence and dissipation rates and enables high cooperativity dynamics [104]. In this sense, the couplings demonstrated here do not yet constitute a single quantum coherent interface, because the observed transitions are induced by classically driven fields containing a very large number of quanta.

One possible strategy to mitigate weak single quantum coupling is to use an ensemble of NV centers, exploiting collective enhancement of the effective coupling strength. Indeed, hybrid circuit experiments have demonstrated coupling between NV center ensembles and superconducting resonators [105, 106]. Nevertheless, ensemble systems typically suffer from additional inhomogeneous broadening and experimentally challenging noise sources, which limit coherence and reduce the fidelity of quantum state transfer.

Therefore, realizing a scalable interface between NV centers and other qubit platforms ultimately requires a regime in which vacuum field coupling alone can drive NV center transitions with high cooperativity. Moreover, because the thermal occupation of propagating bosonic excitations (phonons or magnons) can overwhelm single quantum signals, operation in a cryogenic environment is necessary to suppress thermal populations. Establishing a platform with high cooperativity at cryogenic temperatures would open a realistic route to NV-based hybrid quantum networks mediated by phonons and magnons.

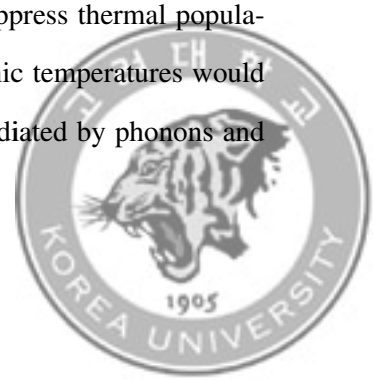

Bibliography

[1] Debdyuti Mandal and Sourav Banerjee. Surface acoustic wave (SAW) sensors: Physics, materials, and applications. *Sensors (Basel)*, 22(3):820, January 2022.

[2] Richard P Feynman. Simulating physics with computers. *Int. J. Theor. Phys.*, 21(6-7):467–488, June 1982.

[3] D L Moehring, P Maunz, S Olmschenk, K C Younge, D N Matsukevich, L-M Duan, and C Monroe. Entanglement of single-atom quantum bits at a distance. *Nature*, 449(7158):68–71, September 2007.

[4] Simon J Evered, Dolev Bluvstein, Marcin Kalinowski, Sepehr Ebadi, Tom Manovitz, Hengyun Zhou, Sophie H Li, Alexandra A Geim, Tout T Wang, Nishad Maskara, Harry Levine, Giulia Semeghini, Markus Greiner, Vladan Vuletić, and Mikhail D Lukin. High-fidelity parallel entangling gates on a neutral-atom quantum computer. *Nature*, 622(7982):268–272, October 2023.

[5] L M Vandersypen, M Steffen, G Breyta, C S Yannoni, M H Sherwood, and I L Chuang. Experimental realization of shor's quantum factoring algorithm using nuclear magnetic resonance. *Nature*, 414(6866):883–887, December 2001.

[6] Chenlu Wang, Xuegang Li, Huikai Xu, Zhiyuan Li, Junhua Wang, Zhen Yang, Zhenyu Mi, Xuehui Liang, Tang Su, Chuhong Yang, Guangyue Wang, Wenyan Wang, Yongchao Li, Mo Chen, Chengyao Li, Kehuan Linghu, Jiaxiu Han, Yingshan Zhang, Yulong Feng, Yu Song, Teng Ma, Jingning Zhang, Ruixia Wang, Peng Zhao, Weiyang Liu, Guangming Xue, Yirong Jin, and Haifeng Yu. Towards practical quantum computers: transmon qubit with a lifetime approaching 0.5 milliseconds. *Npj Quantum Inf.*, 8(1):3, January 2022.

[7] Stefania Castelletto and Alberto Boretti. Silicon carbide color centers for quantum applications. *JPhys Photonics*, 2(2):022001, April 2020.

[8] M Körber, O Morin, S Langenfeld, A Neuzner, S Ritter, and G Rempe. Decoherence-protected memory for a single-photon qubit. *Nat. Photonics*, 12(1):18–21, January 2018.

[9] Qianfan Chen, Ivar Martin, Liang Jiang, and Dafei Jin. Electron spin coherence on a solid neon surface. *Quantum Sci. Technol.*, 7(4):045016, October 2022.

[10] Frank Arute, Kunal Arya, Ryan Babbush, Dave Bacon, Joseph C Bardin, Rami Barends, Rupak Biswas, Sergio Boixo, Fernando G S L Brandao, David A Buell, Brian Burkett, Yu Chen, Zijun Chen, Ben Chiaro, Roberto Collins, William Courtney, Andrew Dunsworth, Edward Farhi, Brooks Foxen, Austin Fowler, Craig Gidney, Marissa Giustina, Rob Graff, Keith Guerin, Steve Habegger, Matthew P Harrigan, Michael J Hartmann, Alan Ho, Markus Hoffmann, Trent Huang, Travis S Humble, Sergei V Isakov, Evan Jeffrey, Zhang Jiang, Dvir Kafri, Kostyantyn Kechedzhi, Julian Kelly, Paul V Klimov, Sergey Knysh, Alexander Korotkov, Fedor Kostritsa, David Landhuis, Mike Lindmark, Erik Lucero, Dmitry Lyakh, Sal-

vatore Mandrà, Jarrod R McClean, Matthew McEwen, Anthony Megrant, Xiao Mi, Kristel Michielsen, Masoud Mohseni, Josh Mutus, Ofer Naaman, Matthew Neeley, Charles Neill, Murphy Yuezhen Niu, Eric Ostby, Andre Petukhov, John C Platt, Chris Quintana, Eleanor G Rieffel, Pedram Roushan, Nicholas C Rubin, Daniel Sank, Kevin J Satzinger, Vadim Smelyanskiy, Kevin J Sung, Matthew D Trevithick, Amit Vainsencher, Benjamin Villalonga, Theodore White, Z Jamie Yao, Ping Yeh, Adam Zalcman, Hartmut Neven, and John M Martinis. Quantum supremacy using a programmable superconducting processor. *Nature*, 574(7779):505–510, October 2019.

[11] J-P Tetienne, T Hingant, J-V Kim, L Herrera Diez, J-P Adam, K Garcia, J-F Roch, S Rohart, A Thiaville, D Ravelosona, and V Jacques. Nanoscale imaging and control of domain-wall hopping with a nitrogen-vacancy center microscope. *Science*, 344(6190):1366–1369, June 2014.

[12] L Thiel, Z Wang, M A Tschudin, D Rohner, I Gutiérrez-Lezama, N Ubrig, M Gibertini, E Giannini, A F Morpurgo, and P Maletinsky. Probing magnetism in 2D materials at the nanoscale with single-spin microscopy. *Science*, 364(6444):973–976, June 2019.

[13] James L Webb, Joshua D Clement, Luca Troise, Sepehr Ahmadi, Gustav Juhl Johansen, Alexander Huck, and Ulrik L Andersen. Nanotesla sensitivity magnetic field sensing using a compact diamond nitrogen-vacancy magnetometer. *Appl. Phys. Lett.*, 114(23):231103, June 2019.

[14] Qihui Liu, Shaoxiong Nie, Xiao Peng, Yaochen Zhu, Nan Wang, Yuqiang Hu, Xin Luo, Chun Li, Maoheng Jing, Chunji Zhang, Wei Liu, Hao Chen, Jiangong Cheng,

and Zhenyu Wu. Fiber-integrated diamond quantum sensor for high-voltage current measurements. *Adv. Sens. Res.*, 4(1):2400106, January 2025.

[15] Akihiro Kuwahata, Takahiro Kitaizumi, Kota Saichi, Takumi Sato, Ryuji Igarashi, Takeshi Ohshima, Yuta Masuyama, Takayuki Iwasaki, Mutsuko Hatano, Fedor Jelezko, Moriaki Kusakabe, Takashi Yatsui, and Masaki Sekino. Magnetometer with nitrogen-vacancy center in a bulk diamond for detecting magnetic nanoparticles in biomedical applications. *Sci. Rep.*, 10(1):2483, February 2020.

[16] Jonathan Kenny, Feifei Zhou, Ruihua He, Fedor Jelezko, Teck Seng Koh, and Weibo Gao. Quantum sensing enhancement through a nuclear spin register in nitrogen-vacancy centers in diamond. *Appl. Phys. Rev.*, 12(2):021323, June 2025.

[17] Nabeel Aslam, Matthias Pfender, Philipp Neumann, Rolf Reuter, Andrea Zappe, Felipe Fávaro de Oliveira, Andrej Denisenko, Hitoshi Sumiya, Shinobu Onoda, Junichi Isoya, and Jörg Wrachtrup. Nanoscale nuclear magnetic resonance with chemical resolution. *Science*, 357(6346):67–71, July 2017.

[18] H Bernien, B Hensen, W Pfaff, G Koolstra, M S Blok, L Robledo, T H Taminiau, M Markham, D J Twitchen, L Childress, and R Hanson. Heralded entanglement between solid-state qubits separated by three metres. *Nature*, 497(7447):86–90, May 2013.

[19] Xiao-Xiao Li, Peng-Bo Li, Sheng-Li Ma, and Fu-Li Li. Preparing entangled states between two NV centers via the damping of nanomechanical resonators. *Sci. Rep.*, 7(1):14116, October 2017.

[20] F Fung, E Rosenfeld, J D Schaefer, A Kabcenell, J Gieseler, T X Zhou, T Madhavan, N Aslam, A Yacoby, and M D Lukin. Toward programmable quantum proces-

sors based on spin qubits with mechanically mediated interactions and transport. *Phys. Rev. Lett.*, 132(26):263602, June 2024.

[21] Masaya Fukami, Denis R Candido, David D Awschalom, and Michael E Flatté. Opportunities for long-range magnon-mediated entanglement of spin qubits via on- and off-resonant coupling. *PRX quantum*, 2(4):040314, October 2021.

[22] David P DiVincenzo. Topics in quantum computers. *arXiv [cond-mat.mes-hall]*, December 1996.

[23] F Dolde, I Jakobi, B Naydenov, N Zhao, S Pezzagna, C Trautmann, J Meijer, P Neumann, F Jelezko, and J Wrachtrup. Room-temperature entanglement between single defect spins in diamond. *Nat. Phys.*, 9(3):139–143, March 2013.

[24] N Bar-Gill, L M Pham, A Jarmola, D Budker, and R L Walsworth. Solid-state electronic spin coherence time approaching one second. *Nat. Commun.*, 4(1):1743, April 2013.

[25] Marcus W Doherty, Neil B Manson, Paul Delaney, Fedor Jelezko, Jörg Wrachtrup, and Lloyd C L Hollenberg. The nitrogen-vacancy colour centre in diamond. *Phys. Rep.*, 528(1):1–45, July 2013.

[26] Clarice D Aiello, Masashi Hirose, and Paola Cappellaro. Composite-pulse magnetometry with a solid-state quantum sensor. *Nat. Commun.*, 4(1):1419, January 2013.

[27] I Cohen, N Aharon, and A Retzker. Continuous dynamical decoupling utilizing time-dependent detuning: Continuous dynamical decoupling utilizing time-dependent detuning. *Fortschr. Phys.*, 65(6-8):1600071, June 2017.

[28] N Aharon, I Cohen, F Jelezko, and A Retzker. Fully robust qubit in atomic and molecular three-level systems. *New J. Phys.*, 18(12):123012, December 2016.

[29] N Aharon, M Drewsen, and A Retzker. General scheme for the construction of a protected qubit subspace. *Phys. Rev. Lett.*, 111(23):230507, December 2013.

[30] Genko T Genov, Nati Aharon, Fedor Jelezko, and Alex Retzker. Mixed dynamical decoupling. *Quantum Sci. Technol.*, 4(3):035010, July 2019.

[31] Alexander Stark, Nati Aharon, Thomas Unden, Daniel Louzon, Alexander Huck, Alex Retzker, Ulrik L Andersen, and Fedor Jelezko. Narrow-bandwidth sensing of high-frequency fields with continuous dynamical decoupling. *Nat. Commun.*, 8(1):1105, October 2017.

[32] N Timoney, I Baumgart, M Johanning, A F Varón, M B Plenio, A Retzker, and Ch Wunderlich. Quantum gates and memory using microwave-dressed states. *Nature*, 476(7359):185–188, August 2011.

[33] J-M Cai, B Naydenov, R Pfeiffer, L P McGuinness, K D Jahnke, F Jelezko, M B Plenio, and A Retzker. Robust dynamical decoupling with concatenated continuous driving. *New J. Phys.*, 14(11):113023, November 2012.

[34] A Barfuss, J Teissier, E Neu, A Nunnenkamp, and P Maletinsky. Strong mechanical driving of a single electron spin. *Nat. Phys.*, 11(10):820–824, October 2015.

[35] J-P Tetienne, L Rondin, P Spinicelli, M Chipaux, T Debuisschert, J-F Roch, and V Jacques. Magnetic-field-dependent photodynamics of single NV defects in diamond: an application to qualitative all-optical magnetic imaging. *New J. Phys.*, 14(10):103033, October 2012.

[36] Michael Nielsen and Isaac Chuang. *Quantum Computation and Quantum Information*. Cambridge University Press, Cambridge, England, 2010.

[37] P Krantz, M Kjaergaard, F Yan, T P Orlando, S Gustavsson, and W D Oliver. A quantum engineer's guide to superconducting qubits. *Appl. Phys. Rev.*, 6(2):021318, June 2019.

[38] Wenlong Zhang, Jian Zhang, Junfeng Wang, Fupan Feng, Shengran Lin, Liren Lou, Wei Zhu, and Guanzhong Wang. Depth-dependent decoherence caused by surface and external spins for NV centers in diamond. *Phys. Rev. B*, 96(23):235443, December 2017.

[39] Wing Ki Lo, Yaowen Zhang, Ho Yin Chow, Jiahao Wu, Man Yin Leung, Kin On Ho, Xuliang Du, Yifan Chen, Yang Shen, Ding Pan, and Sen Yang. Enhancement of quantum coherence in solid-state qubits via interface engineering. *Nat. Commun.*, 16(1):5984, July 2025.

[40] Kihwan Kim, Yisoo Na, Jungbae Yoon, Dongkwon Lee, Hee Seong Kang, Chul-Ho Lee, Chulki Kim, and Donghun Lee. Suppression of spin-bath and low-frequency noise for submegahertz ac magnetometry based on a doubly dressed spin qubit in diamond. *Phys. Rev. Appl.*, 23(6):064004, June 2025.

[41] Scott T Alsid, Jennifer M Schloss, Matthew H Steinecker, John F Barry, Andrew C Maccabe, Guoqing Wang, Paola Cappellaro, and Danielle A Braje. Solid-state microwave magnetometer with picotesla-level sensitivity. *Phys. Rev. Appl.*, 19(5):054095, May 2023.

[42] Jner Tzern Oon, Jiashen Tang, Connor A Hart, Kevin S Olsson, Matthew J Turner, Jennifer M Schloss, and Ronald L Walsworth. Ramsey envelope modulation in NV diamond magnetometry. *Phys. Rev. B.*, 106(5):054110, August 2022.

[43] Brendan A McCullian, Ahmed M Thabt, Benjamin A Gray, Alex L Melendez, Michael S Wolf, Vladimir L Safonov, Denis V Pelekhov, Vidya P Bhallamudi, Michael R Page, and P Chris Hammel. Broadband multi-magnon relaxometry using a quantum spin sensor for high frequency ferromagnetic dynamics sensing. *Nat. Commun.*, 11(1):5229, October 2020.

[44] Jeffrey V Cady, Ohad Michel, Kenneth W Lee, Rishi N Patel, Christopher J Sarabalis, Amir H Safavi-Naeini, and Ania C Bleszynski Jayich. Diamond optomechanical crystals with embedded nitrogen-vacancy centers. *Quantum Sci. Technol.*, 4(2):024009, March 2019.

[45] Preeti Ovartchaiyapong, Kenneth W Lee, Bryan A Myers, and Ania C Bleszynski Jayich. Dynamic strain-mediated coupling of a single diamond spin to a mechanical resonator. *Nat. Commun.*, 5(1):4429, July 2014.

[46] Kenneth W Lee, Donghun Lee, Preeti Ovartchaiyapong, Joaquin Minguzzi, Jero R Maze, and Ania C Bleszynski Jayich. Strain coupling of a mechanical resonator to a single quantum emitter in diamond. *Phys. Rev. Appl.*, 6(3):034005, September 2016.

[47] A Barfuss, M Kasperczyk, J Kölbl, and P Maletinsky. Spin-stress and spin-strain coupling in diamond-based hybrid spin oscillator systems. *Phys. Rev. B*, 99(17):174102, May 2019.

[48] Shimon Kolkowitz, Ania C Bleszynski Jayich, Quirin P Unterreithmeier, Steven D Bennett, Peter Rabl, J G E Harris, and Mikhail D Lukin. Coherent sensing of a mechanical resonator with a single-spin qubit. *Science*, 335(6076):1603–1606, March 2012.

[49] Michael S J Barson, Phani Peddibhotla, Preeti Ovartchaiyapong, Kumaravelu Ganesan, Richard L Taylor, Matthew Gebert, Zoe Mielens, Berndt Koslowski, David A Simpson, Liam P McGuinness, Jeffrey McCallum, Steven Prawer, Shinobu Onoda, Takeshi Ohshima, Ania C Bleszynski Jayich, Fedor Jelezko, Neil B Manson, and Marcus W Doherty. Nanomechanical sensing using spins in diamond. *Nano Lett.*, 17(3):1496–1503, March 2017.

[50] Donghun Lee, Kenneth W Lee, Jeffrey V Cady, Preeti Ovartchaiyapong, and Ania C Bleszynski Jayich. Topical review: spins and mechanics in diamond. *J. Opt.*, 19(3):033001, March 2017.

[51] P Ovartchaiyapong, L M A Pascal, B A Myers, P Lauria, and A C Bleszynski Jayich. High quality factor single-crystal diamond mechanical resonators. *Appl. Phys. Lett.*, 101(16):163505, October 2012.

[52] Philipp Pirro, Vitaliy I Vasyuchka, Alexander A Serga, and Burkard Hillebrands. Advances in coherent magnonics. *Nat. Rev. Mater.*, 6(12):1114–1135, July 2021.

[53] Yutaka Tabuchi, Seiichiro Ishino, Atsushi Noguchi, Toyofumi Ishikawa, Rekishu Yamazaki, Koji Usami, and Yasunobu Nakamura. QUANTUM INFORMATION. coherent coupling between a ferromagnetic magnon and a superconducting qubit. *Science*, 349(6246):405–408, July 2015.

[54] Da Xu, Xu-Ke Gu, He-Kang Li, Yuan-Chao Weng, Yi-Pu Wang, Jie Li, H Wang, Shi-Yao Zhu, and J Q You. Quantum control of a single magnon in a macroscopic spin system. *Phys. Rev. Lett.*, 130(19):193603, May 2023.

[55] K An, M Xu, A Mucchietto, C Kim, K-W Moon, C Hwang, and D Grundler. Emergent coherent modes in nonlinear magnonic waveguides detected at ultrahigh frequency resolution. *Nat. Commun.*, 15(1):7302, August 2024.

[56] Bivas Rana, Yasuhiro Fukuma, Katsuya Miura, Hiromasa Takahashi, and Yoshichika Otani. Excitation of coherent propagating spin waves in ultrathin CoFeB film by voltage-controlled magnetic anisotropy. *Appl. Phys. Lett.*, 111(5):052404, July 2017.

[57] Jinho Lim, Wonbae Bang, Jonathan Trossman, Andreas Kreisel, Matthias Benjamin Jungfleisch, Axel Hoffmann, C C Tsai, and John B Ketterson. Direct detection of multiple backward volume modes in yttrium iron garnet at micron scale wavelengths. *Phys. Rev. B.*, 99(1):014435, January 2019.

[58] Clara Mühlherr, V O Shkolnikov, and Guido Burkard. Magnetic resonance in defect spins mediated by spin waves. *Phys. Rev. B*, 99(19):195413, May 2019.

[59] Yuhei Sekiguchi, Yuki Yasui, Kazuya Tsurumoto, Yuta Koga, Raustin Reyes, and Hideo Kosaka. Geometric entanglement of a photon and spin qubits in diamond. *Commun. Phys.*, 4(1):264, December 2021.

[60] W Pfaff, B J Hensen, H Bernien, S B van Dam, M S Blok, T H Taminiau, M J Tiggelman, R N Schouten, M Markham, D J Twitchen, and R Hanson. Quantum information. unconditional quantum teleportation between distant solid-state quantum bits. *Science*, 345(6196):532–535, August 2014.

[61] M H Abobeih, J Cramer, M A Bakker, N Kalb, M Markham, D J Twitchen, and T H Taminiau. One-second coherence for a single electron spin coupled to a multi-qubit nuclear-spin environment. *Nat. Commun.*, 9(1):2552, June 2018.

[62] Xiaoche Wang, Yuxuan Xiao, Chuanpu Liu, Eric Lee-Wong, Nathan J McLaughlin, Hanfeng Wang, Mingzhong Wu, Hailong Wang, Eric E Fullerton, and Chunhui Rita Du. Electrical control of coherent spin rotation of a single-spin qubit. *Npj Quantum Inf.*, 6(1):78, September 2020.

[63] Dany Lachance-Quirion, Yutaka Tabuchi, Arnaud Gloppe, Koji Usami, and Yasunobu Nakamura. Hybrid quantum systems based on magnonics. *Appl. Phys. Express*, 12(7):070101, July 2019.

[64] Abdulqader Mahmoud, Florin Ciubotaru, Frederic Vanderveken, Andrii V Chumak, Said Hamdioui, Christoph Adelmann, and Sorin Cotofana. Introduction to spin wave computing. *J. Appl. Phys.*, 128(16):161101, October 2020.

[65] Paolo Andrich, Charles F de las Casas, Xiaoying Liu, Hope L Bretscher, Jonson R Berman, F Joseph Heremans, Paul F Nealey, and David D Awschalom. Long-range spin wave mediated control of defect qubits in nanodiamonds. *Npj Quantum Inf.*, 3(1):28, July 2017.

[66] Masaya Fukami, Jonathan C Marcks, Denis R Candido, Leah R Weiss, Benjamin Soloway, Sean E Sullivan, Nazar Delegan, F Joseph Heremans, Michael E Flatté, and David D Awschalom. Magnon-mediated qubit coupling determined via dissipation measurements. *Proc. Natl. Acad. Sci. U. S. A.*, 121(2):e2313754120, January 2024.

[67] Toeno van der Sar, Francesco Casola, Ronald Walsworth, and Amir Yacoby. Nanometre-scale probing of spin waves using single-electron spins. *Nat. Commun.*, 6(1):7886, August 2015.

[68] Tony X Zhou, Joris J Carmiggelt, Lisa M Gächter, Ilya Esterlis, Dries Sels, Rainer J Stöhr, Chunhui Du, Daniel Fernandez, Joaquin F Rodriguez-Nieva, Felix Büttner, Eugene Demler, and Amir Yacoby. A magnon scattering platform. *Proc. Natl. Acad. Sci. U. S. A.*, 118(25):e2019473118, June 2021.

[69] Joris J Carmiggelt, Iacopo Bertelli, Roland W Mulder, Annick Teepe, Mehrdad Elyasi, Brecht G Simon, Gerrit E W Bauer, Yaroslav M Blanter, and Toeno van der Sar. Broadband microwave detection using electron spins in a hybrid diamond-magnet sensor chip. *Nat. Commun.*, 14(1):490, January 2023.

[70] Eric Lee-Wong, Ruolan Xue, Feiyang Ye, Andreas Kreisel, Toeno van der Sar, Amir Yacoby, and Chunhui Rita Du. Nanoscale detection of magnon excitations with variable wavevectors through a quantum spin sensor. *Nano Lett.*, 20(5):3284–3290, May 2020.

[71] C S Wolfe, V P Bhallamudi, H L Wang, C H Du, S Manuilov, R M Teeling-Smith, A J Berger, R Adur, F Y Yang, and P C Hammel. Off-resonant manipulation of spins in diamond via precessing magnetization of a proximal ferromagnet. *Phys. Rev. B*, 89(18):180406, May 2014.

[72] Iacopo Bertelli, Joris J Carmiggelt, Tao Yu, Brecht G Simon, Coosje C Pothoven, Gerrit E W Bauer, Yaroslav M Blanter, Jan Aarts, and Toeno van der Sar. Magnetic resonance imaging of spin-wave transport and interference in a magnetic insulator. *Sci. Adv.*, 6(46):eabd3556, November 2020.

[73] Brecht G Simon, Samer Kurdi, Helena La, Iacopo Bertelli, Joris J Carmiggelt, Maximilian Ruf, Nick de Jong, Hans van den Berg, Allard J Katan, and Toeno van der Sar. Directional excitation of a high-density magnon gas using coherently driven spin waves. *Nano Lett.*, 21(19):8213–8219, October 2021.

[74] Chunhui Du, Toeno van der Sar, Tony X Zhou, Pramey Upadhyaya, Francesco Casola, Huiliang Zhang, Mehmet C Onbasli, Caroline A Ross, Ronald L Walsworth, Yaroslav Tserkovnyak, and Amir Yacoby. Control and local measurement of the spin chemical potential in a magnetic insulator. *Science*, 357(6347):195–198, July 2017.

[75] Brecht G Simon, Samer Kurdi, Joris J Carmiggelt, Michael Borst, Allard J Katan, and Toeno van der Sar. Filtering and imaging of frequency-degenerate spin waves using nanopositioning of a single-spin sensor. *Nano Lett.*, 22(22):9198–9204, November 2022.

[76] Michal Gryga, Dalibor Ciprian, and Petr Hlubina. Distributed bragg reflectors employed in sensors and filters based on cavity-mode spectral-domain resonances. *Sensors (Basel)*, 22(10):3627, May 2022.

[77] Weichao Yu (余超, Jin Lan (金, Ruqian Wu, and Jiang Xiao (江. Magnetic snell's law and spin-wave fiber with dzyaloshinskii-moriya interaction. *Phys. Rev. B*, 94(14):140410, October 2016.

[78] Roman Verba, Vasil Tiberkevich, and Andrei Slavin. Spin-wave transmission through an internal boundary: Beyond the scalar approximation. *Phys. Rev. B.*, 101(14):144430, April 2020.

[79] Huajun Qin, Rasmus B Holländer, Lukáš Flajšman, Felix Hermann, Rouven Dreyer, Georg Woltersdorf, and Sebastiaan van Dijken. Nanoscale magnonic fabry-pérot resonator for low-loss spin-wave manipulation. *Nat. Commun.*, 12(1):2293, April 2021.

[80] Tao Yu, Yaroslav M Blanter, and Gerrit E W Bauer. Chiral pumping of spin waves. *Phys. Rev. Lett.*, 123(24):247202, December 2019.

[81] A V Chumak, P Pirro, A A Serga, M P Kostylev, R L Stamps, H Schultheiss, K Vogt, S J Hermsdoerfer, B Laegel, P A Beck, and B Hillebrands. Spin-wave propagation in a microstructured magnonic crystal. *Appl. Phys. Lett.*, 95(26):262508, December 2009.

[82] Tao Yu, Chuanpu Liu, Haiming Yu, Yaroslav M Blanter, and Gerrit E W Bauer. Chiral excitation of spin waves in ferromagnetic films by magnetic nanowire gratings. *Phys. Rev. B.*, 99(13):134424, April 2019.

[83] M P Kostylev, A A Stashkevich, and N A Sergeeva. Collective magnetostatic modes on a one-dimensional array of ferromagnetic stripes. *Phys. Rev. B*, 69(6):064408, February 2004.

[84] Alexey B Ustinov, Andrei V Drozdovskii, Andrey A Nikitin, Alexander A Semenov, Dmytro A Bozhko, Alexander A Serga, Burkard Hillebrands, Erkki Lähderanta, and Boris A Kalinikos. Dynamic electromagnonic crystal based on artificial multiferroic heterostructure. *Commun. Phys.*, 2(1):137, December 2019.

[85] V D Bessonov, M Mruczkiewicz, R Gieniusz, U Guzowska, A Maziewski, A I Stognij, and M Krawczyk. Magnonic band gaps in YIG-based one-dimensional

magnonic crystals: An array of grooves versus an array of metallic stripes. *Phys. Rev. B*, 91(10):104421, March 2015.

[86] César L Ordóñez-Romero, Zorayda Lazcano-Ortiz, Andrey Drozdovskii, Boris Kalinikos, Melisa Aguilar-Huerta, J L Domínguez-Juárez, Guillermo Lopez-Maldonado, Naser Qureshi, Oleg Kolokoltsev, and Guillermo Monsivais. Mapping of spin wave propagation in a one-dimensional magnonic crystal. *J. Appl. Phys.*, 120(4):043901, July 2016.

[87] Marc Vogel, Andrii V Chumak, Erik H Waller, Thomas Langner, Vitaliy I Vasyuchka, Burkard Hillebrands, and Georg von Freymann. Optically reconfigurable magnetic materials. *Nat. Phys.*, 11(6):487–491, June 2015.

[88] Haruka Komiyama, Ryusuke Hisatomi, Kotaro Taga, Hiroki Matsumoto, Takahiro Moriyama, Hideki Narita, Shutaro Karube, Yoichi Shiota, and Teruo Ono. Quantitative evaluation method for magnetoelastic coupling between surface acoustic waves and spin waves using electrical and optical measurements. *arXiv [cond-mat.mes-hall]*, July 2024.

[89] Yi Li, Chenbo Zhao, Wei Zhang, Axel Hoffmann, and Valentyn Novosad. Advances in coherent coupling between magnons and acoustic phonons. *APL Mater.*, 9(6):060902, June 2021.

[90] Yunyoung Hwang, Jorge Puebla, Kouta Kondou, Carlos Gonzalez-Ballestero, Hironari Isshiki, Carlos Sánchez Muñoz, Liyang Liao, Fa Chen, Wei Luo, Sadamichi Maekawa, and Yoshichika Otani. Strongly coupled spin waves and surface acoustic waves at room temperature. *Phys. Rev. Lett.*, 132(5):056704, February 2024.

[91] Andreas Rückriegel, Peter Kopietz, Dmytro A Bozhko, Alexander A Serga, and Burkard Hillebrands. Magnetoelastic modes and lifetime of magnons in thin yttrium iron garnet films. *Phys. Rev. B*, 89(18):184413, May 2014.

[92] Andrey A Grachev, Alexandr V Sadovnikov, and Sergey A Nikitov. Strain-tuned spin-wave interference in micro- and nanoscale magnonic interferometers. *Nanomaterials (Basel)*, 12(9):1520, April 2022.

[93] R S Weis and T K Gaylord. Lithium niobate: Summary of physical properties and crystal structure. *Appl. Phys. A*, 37(4):191–203, August 1985.

[94] H Engan. Excitation of elastic surface waves by spatial harmonics of interdigital transducers. *IEEE Trans. Electron Devices*, 16(12):1014–1017, December 1969.

[95] Xiao Chen, Mohammad Ali Mohammad, James Conway, Bo Liu, Yi Yang, and Tian-Ling Ren. High performance lithium niobate surface acoustic wave transducers in the 4–12 GHz super high frequency range. *J. Vac. Sci. Technol. B Nanotechnol. Microelectron.*, 33(6):06F401, November 2015.

[96] Christian Heeg. *Spin mechanics at radio frequencies*. PhD thesis, TECHNISCHE UNIVERSITAT¨ MUNCHEN, Munich, 2010.

[97] Dominic Labanowski. *Acoustically Driven Ferromagnetic Resonance for Device Applications*. PhD thesis, UC Berkeley, 2017.

[98] M Weiler. *Magnon-phonon interactions in ferromagnetic thin films*. PhD thesis, TECHNISCHE UNIVERSITAT¨ MUNCHEN, 2012.

[99] M Weiler, L Dreher, C Heeg, H Huebl, R Gross, M S Brandt, and S T B Goennenwein. Elastically driven ferromagnetic resonance in nickel thin films. *Phys. Rev. Lett.*, 106(11):117601, March 2011.

[100] D Hatanaka, M Asano, H Okamoto, Y Kunihashi, H Sanada, and H Yamaguchi. On-chip coherent transduction between magnons and acoustic phonons in cavity magnomechanics. *Phys. Rev. Appl.*, 17(3):034024, March 2022.

[101] Dominic Labanowski, Vidya Praveen Bhallamudi, Qiaochu Guo, Carola M Purser, Brendan A McCullian, P Chris Hammel, and Sayeef Salahuddin. Voltage-driven, local, and efficient excitation of nitrogen-vacancy centers in diamond. *Sci. Adv.*, 4(9):eaat6574, September 2018.

[102] Blai Casals, Nahuel Statuto, Michael Foerster, Alberto Hernández-Mínguez, Rafael Cichelero, Peter Manshausen, Ania Mandziak, Lucía Aballe, Joan Manel Hernàndez, and Ferran Macià. Generation and imaging of magnetoacoustic waves over millimeter distances. *Phys. Rev. Lett.*, 124(13):137202, April 2020.

[103] Marc Rovirola, M Waqas Khaliq, Travis Gustafson, Fiona Sosa-Barth, Blai Casals, Joan Manel Hernàndez, Sandra Ruiz-Gómez, Miguel Angel Niño, Lucía Aballe, Alberto Hernández-Mínguez, Michael Foerster, and Ferran Macià. Study of the magnetoelastic effect in nickel and cobalt thin films at GHz range using x-ray microscopy. *Phys. Rev. Res.*, 6(2):023285, June 2024.

[104] Cleaven Chia, Ding Huang, Victor Leong, Jian Feng Kong, and Kuan Eng Johnson Goh. Hybrid quantum systems with artificial atoms in solid state. *Adv. Quantum Technol.*, 7(5):2300461, May 2024.

[105] Xiaobo Zhu, Shiro Saito, Alexander Kemp, Kosuke Kakuyanagi, Shin-Ichi Karimoto, Hayato Nakano, William J Munro, Yasuhiro Tokura, Mark S Everitt, Kae Nemoto, Makoto Kasu, Norikazu Mizuochi, and Kouichi Semba. Coherent coupling of a superconducting flux qubit to an electron spin ensemble in diamond. *Nature*, 478(7368):221–224, October 2011.

[106] Y Kubo, C Grezes, A Dewes, T Umeda, J Isoya, H Sumiya, N Morishita, H Abe, S Onoda, T Ohshima, V Jacques, A Dréau, J-F Roch, I Diniz, A Auffeves, D Vion, D Esteve, and P Bertet. Hybrid quantum circuit with a superconducting qubit coupled to a spin ensemble. *Phys. Rev. Lett.*, 107(22):220501, November 2011.

Appendix A. Fabrication recipe

This chapter illustrates the fabrication procedures. We fabricate diamond resonators, YIG devices, and lithium-niobate/nickel devices. Most processes are carried out at KIST micro-nano fab center. Sometimes, SEM equipment and ICP-RIE in KU engineering department, clean room in KUKIST, or ICP-RIE etching in KANC are used.

- Diamond resonator

This work is composed of physical etching, patterning and wet etching. The etching process has two different recipes, Ar/Cl_2 and O_2. Since chlorine gas is dangerous to handle, we request KANC for etching, rather than being performed in-house. Other etching process is self operated in KU engineering fab center. We start from 2mm X 2mm diamond plate. And substrate is silicon oxide wafer. During process, cleaning is done at intervals.

Slicing	Commercial service. Laser slicing and polish into 3 20 μm thick pieces. (Applied Diamond, Inc.)
Bonding	Spin coating FOX-16 3000 rpm, 10 sec. Put diamond on coated substrate on weight in 2 minutes room temperature. If necessary using cotton swab press the diamond or cleaning FOX-16 To prevent bonding upper substrate and substrate. Put on hot plate 160°C, 2 minutes. If necessary remove contamination using cotton swab with acetone and IPA. Put in wafer bonder machine 420°C, 3 hours, rising time 1 hour and pressing force 3 kg/cm^2 (KIST micronano fab)
Etching(Thinning)	Etch diamond plate to 1 μm. Ar 25 sccm, Cl_2 40 sccm ICP 500W (bias 200W) Pressure : 0.7 Pa Estimated etch rate : 1.7 μm/hrs cycle : 15 minutes process 15 minutes cooling (KANC ICP - RIE)
Patterning	Spin coating AZ 5214E 3000 rpm, 30 sec. Bake 110 °C 1 minute Exposure 15 sec (UV lamp power 350W) Develop MIF 300, 1 minute (KUKIST cleanroom) Aluminum 100 nm e-beam evaporation (KIST micro-nano fab)
Etching(Patterning)	Etch diamond to shape resonator. O_2 30 sccm, ICP 700W (bias 200W) Pressure : 20 mTorr Estimated etch rate : 3 µm/hrs (KU engineering fab ICP - RIE)
Releasing	Wet etching oxide layer in BOE (KUKIST cleanroom)

Table A.1: Recipe for diamond resonator.

- Antenna or DBR on YIG film

We start from 1 cm X 1 cm, YIG 100 nm film on GGG substrate that is commercially available. (Matesy) We make stripline antenna on YIG film to excite spin wave and array of stripes to study reflector of spin wave. When linewidth of the pattern is narrow under 2 μm, We request e-beam lithography by commercial service. (SEMCRON) Only photolithography is introduce under the table. This work is composed of lithography, evaporation and lift-off. All process is done in KIST micro-nano fab center. Depending on whether the linewidth is wider than 2 μm, the lithography tool is changed. The finer structure, the more precise detailed parameter adjustment is needed.

- SAW device on lithium niobate

The IDT, launcher of SAW, is a periodic, narrow pattern. Slightly changed condition may change the IDT width, which affects the performance of the IDT. We tried Aluminum and gold as IDT material, as a consequence, Aluminum is a better choice for higher SAW mode excitation. We start from lithium niobate chip, 1 cm X 1cm X 0.5 mm, commerically available. (MTI corp.) YZ-cut and 128 XY-cut are used in our research and to be sure of crystal direction, corner of chip is sliced.

Lithography (2 μm linewidth)	Spin coat HMDS 3000 rpm 30 sec Spin coat GXR-601 (14cp) 3000 rpm 30 sec Bake 95°C, 1 minute 30 sec. Exposure 28 mJ (EVG aligner) Post bake 110 °C 1 minute Develop MIF 300, 22 sec.
Lithography (over 2 μm linewidth)	Spin coat HMDS 3000 rpm 30 sec Spin coat AZ5214E 3000 rpm 30 sec Bake 110°C, 1 minute. Exposure 15 sec (MA-6) Develop MIF 300, 40 sec.
Evaporation	Ti/Au (10 nm / 100 nm) is for spin wave antenna. Ni/Au (100 nm / 5 nm) is for reflector array.
Lift-off	Put Acetone for long time until perfect lift-off

Table A.2: Recipe for YIG structure and SAW device.

- Cleaning

Cleaning is essential during fabrication. In every step, small contamination can be introduced regardless of cause. This maybe due to photo resist residues or small metal pieces after lift off. These defects can degrade subsequent steps in fabrication. To clean contamination without damage in device is important. We used acetone and IPA as remover of organic material like photo resist. Rather than simply soaking the sample, sonication is more effective to remove contamination. But, sometimes fragile sample is vulnerable in sonication. Mechanical resonator and metal layer with weak adhesion can be damaged or delaminated during sonication. Care should be taken when using sonication. Another way to clean organic material is microwave plasma asher. Ashing removes resist using plasma. It can be controlled by power and time. It helps to remove contamination, but because it involves etching, it is important to determine whether it causes damage to the sample. We use asher 200W, 2 minutes maximum for YIG and lithium niobate and it helps remove contamination.